UNIVERSITY OF SOUTHAMPTON

FACULTY OF PHYSICAL SCIENCES AND ENGINEERING

School of Physics and Astronomy

X-ray and microwave studies of strongly exchange coupled magnetic multilayers.

By

Gavin Brian George Stenning

Thesis for the degree of Doctor of Philosophy

August 2013

University of Southampton

Abstract

FACULTY OF PHYSICAL SCIENCES AND ENGINEERING

School of Physics and Astronomy

Doctor of Philosophy

X-ray and microwave studies of strongly exchange coupled multilayers

By Gavin Brian George Stenning

Magnetic exchange spring systems which consist of alternating thin hard and soft magnetic layers provide a great potential in applications such as (*i*) permanent magnets and (*ii*) magnetic data storage. The molecular beam epitaxy-grown samples provide an excellent model system with which to study the magnetic switchings and reversals. X-ray magnetic circular dichroism (XMCD) allows element-selective hysteresis loops with the results presented alongside bulk magnetometry and micromagnetic modelling. This gives a complete picture of $RE\text{Fe}_2$ magnetic exchange springs. This work unveiled the spin-flop and transverse exchange springs in the $\text{ErFe}_2/\text{YFe}_2$ and $\text{DyFe}_2/\text{Fe}_2$ thin film multilayers respectively.

This work has also focused upon studying the magnetisation dynamics of exchange-coupled bilayers. Ferromagnetic resonance spectroscopy gives multiple resonant modes of the NiFe/CoFe exchange-coupled bilayer. X-ray detected ferromagnetic resonance was used to investigate the relationship between the magnetic layers by using XMCD for the magnetic contrast. How the anisotropy of one layer can influence the second, as well as determination of the origin of the two resonant modes are discussed.

A new microwave device is the final aspect of this work. The new topic of metamaterials was studied and opened up new research directions. This work demonstrates that tunability of the metamaterial resonance by applied magnetic field is possible by coupling the resonant split ring resonator structure to magnetic thin films, providing large modulations in transmitted microwave power previously unattained.

Declaration of Authorship

I, Gavin Brian George Stenning declare that this thesis titled ‘X-ray and microwave studies of strongly exchange coupled multilayers’ and the work presented in it are my own and has been generated by me as the result of my own original research, unless otherwise stated.

- The work done was wholly or mainly in candidature for a research degree at this university.
- That any part of this thesis which has previously been submitted for a degree or any other qualification at this university or any other institution, this has been clearly stated.
- When I have consulted the published work of others, it is always clearly attributed.
- When I have quoted from the work of others, the source is always given. With the exception of such quotations this thesis is entirely my own work.
- I have acknowledged all main sources of help.
- Where the thesis is based on work done by myself jointly with others, I have made clear exactly what was done by others and what I have contributed myself.

Signed:

Date:

Acknowledgements

I would like to thank everyone who has helped me for the duration of, and contributing to this PhD thesis. I want to thank specifically the following people:

- My supervisor Prof. Peter de Groot for giving me the opportunity to carry out this research and for many a discussion and ideas.
- Prof. Graham Bowden who although retired has given me a wealth of knowledge both experimentally and theoretically in aspects of magnetism as well as many discussions.
- I wish to thank Gerrit van der Laan, Stuart Cavill, Leigh Shelford, Adriana Figueroa-Garcia and many others at the Diamond Light Source Ltd for their insightful discussions and many experimental measurements and support.
- Greg Ashton for helpful discussions and his work on simulating magnetic bilayers using Nmag as part of his undergraduate degree.
- I would like to express my gratitude to Dr. Thorsten Hesjedal, Dr. Roger Ward and Alberto Sposito who provided the samples studied in this thesis.
- My thanks to Prof. Nikolay Zheludev and all of his metamaterials research group at the Optoelectronics Research Centre for giving me the opportunity to work alongside them.
- I would also like to thank all of my family for their support for the duration of my research and for proof reading this thesis.

Contents

List of symbols

a	Lattice constant
B_a	Applied field
B_B	Bending field
B_c	Coercive field
B_{Cr}	Critical field
B_{co}	Cross over field
B_{rf}	Microwave field
B_{SW}	Stoner-Wohlfarth field
C	Capacitance of the metamolecule
$Ch.$	Chapter
D	Spin-wave stiffness factor
d	Thickness of the magnetic soft layer
E_{dem}	Demagnetising energy
E_{MC}	Magneto-crystalline anisotropy energy
E_{Zee}	Zeeman energy
E''_{Total}	Double differential energy matrix
F', F''	First and second order free energy crystal field terms
G	VSM sensitivity
g	Landé g factor
$\overline{H}$	External magnetic field
$\overline{H}_{dem}$	Demagnetising field
$\overline{H}_{eff}$	Effective field
$\overline{H}_{ex}$	Exchange field
$\overline{H}_k$	Anisotropy field
$\overline{H}_w$	Write field
h	Planks constant
h_{rf}	Microwave excitation field
$\hbar$	Planks constant/2π
$\mathcal{H}_{ex}$	Hamiltonian for exchange
J_{ij}	Exchange integral
$K_{1,2,3}$	Anisotropy parameters
$\tilde{K}_{4,5,6}$	Spherical anisotropy parameters
k_B	Boltzmann constant
k_s	Wavenumber
K_u	Anisotropy per unit volume
L	Inductance of the metamolecule
$\overline{M}$	Magnetisation
m	Magnetic moment
m_J	Magnetic quantum number
M_s	Saturation magnetisation
N	Demagnetising tensor
P	Microwave power
S_{21}	Transmitted microwave scattering parameter

$\left\|S_{21}^{N}\right\|$	Normalised S_{21} to zero applied field
$\bar{S}_i$	Spin at lattice site *i*
$\bar{S}_j$	Spin at lattice site *j*
T	Temperature
t	Time
T_c	Curie temperature
$\bar{T}$	Torque
V_0	Volume of a grain
W	Coplanar waveguide signal line width
$\mathbf{Y}_n^C$	Spherical harmonics (n=4, 6, 8, 10 and 12)
Z_0	Characteristic impedance
α	Gilbert damping constant
$\alpha_{x,y,z}$	Direction of cosines
γ	Gyromagnetic ratio
δ	Mutual interaction between the SRR and a YIG thin film.
ε	Electromotive voltage
$\varepsilon_{i,j,k}$	Energy at site *i,j,k*
ε_r	Dielectric constant
$\langle\theta\rangle_{Er}$	Average inclination angle for Er
μ_0	Permeability of free space
μ_B	Bohr magnetron
μ_r	Relative permeability
ν	Applied frequency
v_g	Group velocity
v_{SRR}	Resonant frequency of the split ring resonator
v_{YIG}	Ferromagnetic resonance of YIG film
ρ	Resistivity
φ	Magnetic flux
$\langle\phi\rangle_{Er}$	Average in-plane angle for Er
ω_0	Ferromagnetic resonance frequency
$\Omega_{i,j,k}$	Cartesian angles ($\theta_{i,j,k}$, $\varphi_{i,j,k}$)
ω	Angular frequency
ω_L	Lamor frequency
ω_{mm}	Resonant frequency of the metamolecule

Publications

G. B. G. Stenning, G. J. Bowden, L. C. Maple, S. A. Gregory, A. Sposito, R. W. Eason, N. I. Zheludev, and P. A. J. de Groot, *Opt. Express.* **21,** 1456 (2013).

A. Sposito, T. C. May-Smith, G. B. G. Stenning, P. A. J. de Groot, R. W. Eason, *Opt. Mater. Express.* **3,** 624. (2013).

A. R. Buckingham, D. Wang, G. B. G. Stenning, G. J. Bowden, I. Nandhakumar, R. C. C. Ward, and P. A. J. de Groot, *J. Phys.: Condens. Matter.* **25,** 086002. (2013).

G. B. G. Stenning, G. J. Bowden, S. A. Gregory, A. N. Dobrynin, L. R. Shelford, P. Bencok, P. Steadman, T. Hesjedal, G. van der Laan, P. A. J. de Groot, *Phys. Rev. B.* **86,** 174420 (2012).

G. B. G. Stenning, G. J. Bowden, S. A. Gregory, J. –M. L. Beaujour, A. N. Dobrynin, L. R. Shelford, P. Bencok, P. Steadman, T. Hesjedal, G. van der Laan, P. A. J. de Groot, *Appl. Phys. Lett.* **101,** 072412 (2012).

G. B. G. Stenning, A. R. Buckingham, G. J. Bowden, R. C. C. Ward, G. van der Laan, L. R. Shelford, F. Maccherozzi, S. S. Dhesi, and P. A. J. de Groot, *Phys Rev. B.* **84,** 104428 (2011).

G. J. Bowden, A. R. Buckingham, G. B. G. Stenning, and P. A. J. de Groot, *J. Condens. Matt. Phys.* **22,** 291001 (2010).

In Preparation

G. B. G. Stenning, L. R. Shelford, S. A. Gregory, F. Hoffmann, M. Haertinger, T. Hesjedal, R. C. C. Ward, G. Woltersdorf, S. A. Cavill, G. J. Bowden, G. Ashton, L. C. Maple, C. H. Back, H. Fangohr, G. van der Laan, and P. A. J. de Groot, In preparation. (2013).

S. A. Gregory, G. B. G. Stenning, G. J. Bowden, N. I. Zheludev, and P. A. J. de Groot, In Preparation. (2013).

1. Introduction

The company known as IBM was the first company in the world to market magnetic data storage [1]. Initially, the device consisted of a rotating disc coated with a thin magnetic film. ‘Bits’ of information were subsequently stored on the disc by magnetising small grains of the film horizontally either to the left or the right. The disc was then scanned by a write/read head which sensed the direction of magnetisation of the individual ‘bits’. The first commercial hard magnetic disk drive (HDD) had a capacity of just 5 megabytes (MB). By contrast today’s storage devices exceed over 1 terabyte (TB) of data.

The rapid rise in the capacity of magnetic data storage has been made possible by a decrease in the physical size of the so-called ‘bits’. Currently, the storage density is typically measured in bits in^{-2}. Figure 1.1 shows the almost logarithmic increase in storage density from 1980 to the present day.

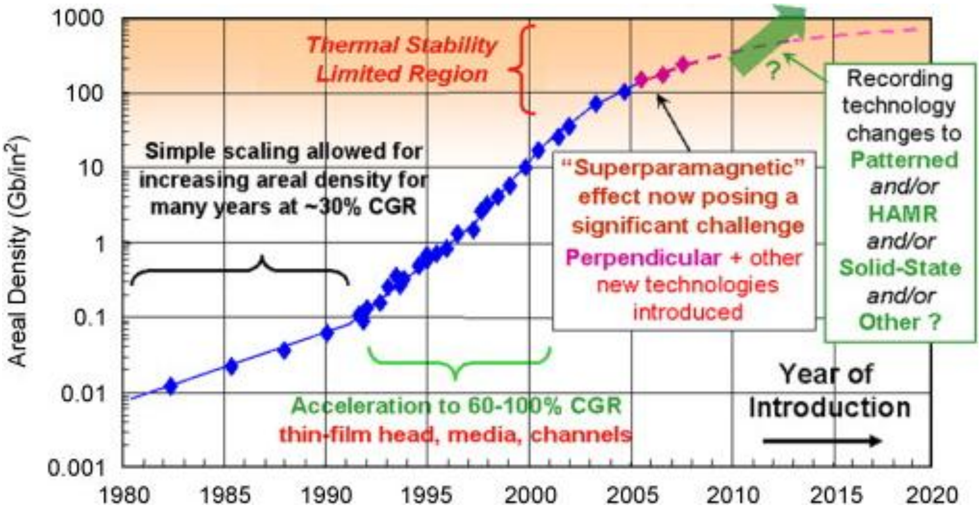

Figure 1.1: Diagram displaying areal density of hard disc drives (HDD) *vs.* year of introduction [2]. In early 2012 Seagate became the first HDD maker to achieve a storage density of 1 TB/in^2 using heat assisted magnetic recording (HAMR).

From an examination of Figure 1.1 it is clear that the trend to smaller and smaller bits will be difficult because of the so-called superparamagnetic limit. For storage densities exceeding 100 GB/in^2, the ‘bit’ size is such that thermal stability of the magnetisation becomes a problem. Individual magnetic elements cannot retain their direction of magnetisation, being thermally reversed at room-temperature. The trade-off between the writability of the ‘bit’ and the thermal effects is what is known as the superparamagnetic limit. Figure 1.1 also lists some alternative methods devoted to overcoming this upcoming problem (see green arrow). Current methods of defeating the superparamagnetic limit include patterned magnetic data storage [3], heat assisted magnetic recording (HAMR) [4] and perpendicular magnetic recording where the magnetisation of the ‘bits’ point out of plane. These future technologies involve the use of harder magnetic materials with larger anisotropies and new approaches to the switching the magnetisation. A few of these possibilities are outlined below.

Longitudinal media

Longitudinal magnetic recording media have long been used as the standard for magnetic data storage. The magnetisation of the data ‘bit’ lies in the plane of the disc (see Figure 1.2 (a)). The ‘bit’ in longitudinal storage media is in reality composed of many magnetic grains, with each grain acting effectively as a single domain [5]. Such systems provide a good signal to noise ratio (SNR), however, if the size of the ‘bit’ is decreased it leads not only to a decrease in the SNR, but also to ‘thermal instability’ (see for example Zhou, Bertram and Moser *et al.* [6, 7]). This can be offset by using harder magnetic materials such as FePt, CoFe or the rare earths, with an increased anisotropy (K) this problem can be avoided to some extent. In practice, it is necessary to satisfy the inequality for thermal stability:

$$(K_u V_0) >> k_B T \qquad (1.1)$$

where K_u is the magnetic anisotropy density (Jm^{-3}), V_0 is the volume of the grain, and $k_B T$ is the available thermal energy which can induce magnetic reversal.

Reading of magnetic media nowadays is usually achieved using a magneto resistance sensor. It is found in the actuator arm in the HDD and is known as the write/read head. To write to the magnetic media (*i.e.* to change the direction of the data ‘bits’ by switching their magnetisation) the write head employs an electromagnet known as the inductive write-head.

Increasing the areal density by decreasing the size of the ‘bit’ and increasing the anisotropy cannot be done limitlessly. In practice, there is an approximate relationship between magnetic write field required to switch the magnetisation of the elements and the anisotropy [7],

$$H_W = \frac{K_u V_0}{\mu_0 M_S} \qquad (1.2)$$

Here, H_W is the required field, with M_s the saturation magnetisation of the element (or bit). Therefore if the anisotropy (K_u) is increased while the bit size (M_s) is decreased, the required write field H_W must increase, however increasing H_W cannot be done limitlessly due to the available field supplied by the write head. Increasing M_s would help with the problem and highlights the potential for composite hard and soft magnetic hard-disc multilayers, where non-coherent switching occurs by magnetic exchange springs being set-up in the thicker magnetically soft layers. This significantly reduces the switching field necessary [8].

Perpendicular media

Recording with perpendicular media, where the magnetisation of the individual ‘bits’ point out of the plane of the disc, was first demonstrated by Takano *et al.* [9] and has been employed in the industry since 2005. The primary advantage of perpendicular media recording is the use of thicker magnetic films [10] which offsets any decrease in areal bit size. Further, the dipole interactions between adjacent magnetic ‘bits’ are reduced.

Nevertheless, various factors still apply in perpendicular media as they do in longitudinal media. The main difference occurs in the write head. Because the areal size of the bits are smaller, the stray-field from the write field can inadvertently switch other grains. To overcome this problem a soft magnetic layer is placed under the perpendicular media which acts as a flux return mechanism. This situation is illustrated in Figure 1.2 (b) which illustrates the return loop through the magnetic write head and the underlying soft-layer.

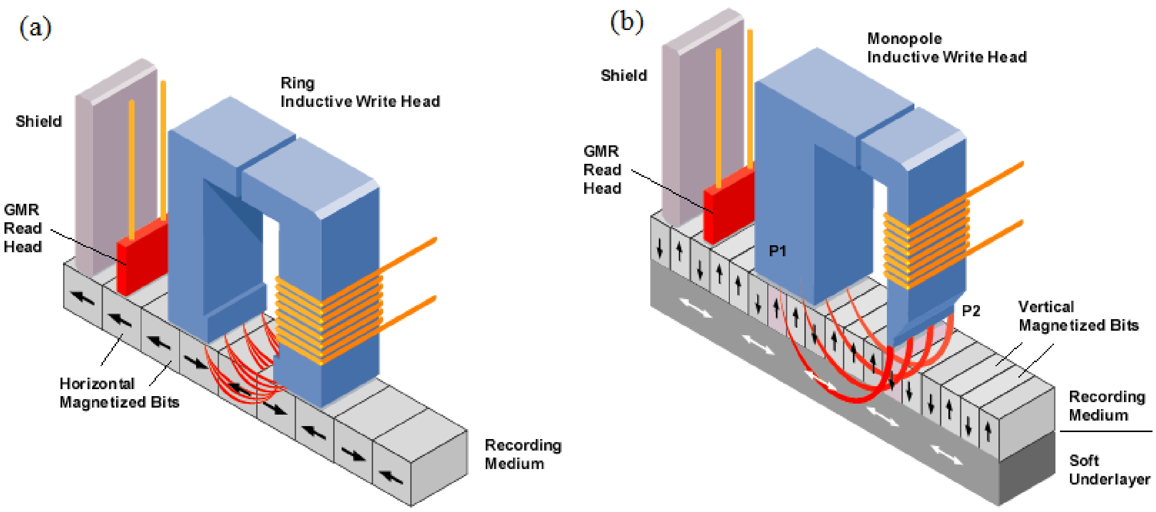

Figure 1.2: Schematic showing (a) longitudinal and (b) perpendicular magnetic recording, with magnetic flux return loop [11].

An example of the early perpendicular magnetic data storage media used is CoCrPt [9]. The disadvantage of perpendicular media is that of write-ability to high anisotropic media. It requires a large magnetic write-field, that causes problems on the data storage device due to the stray fields emitted from the write head [12], secondly increasing the write-field cannot be done limitlessly. The solution to the problem will involve the use of composite magnetic media.

Composite magnetic media

A composite ferromagnetic exchange spring media consisting of a soft magnetic layer coupled to a magnetically harder magnetic layer offers an alternative solution. This type of recording system can alleviate the problem of (*i*) the superparamagnetic limit by using a hard anisotropic magnetic material and (*ii*) switch-ability, the latter being achieved by using exchange springs set up in the thicker soft layer to help switch the hard magnetic layer by non-coherent reversal. The thicker soft layer magnetisation is easily rotated in small applied fields which then exerts a strong effective field on the hard-layer via strong magnetic exchange coupling across the soft-hard layer interface. This reduces the coercive field at which the magnetisation of the hard layer switches [13], allowing for smaller data 'bits' with increased M_S, and higher anisotropy values K_u. In this thesis, such ideas are explored via the use of antiferromagnetically coupled compound rare earth (high anisotropy *RE*Fe$_2$ layers) and magnetically soft YFe$_2$ layers. The samples were grown by molecular beam epitaxy (MBE) at Oxford University [14]. They possess very sharp interfaces (~7 Å) and strong Fe-Fe (~600 K) exchange coupling between the individual layers. These antiferromagnetically coupled exchange spring superlattice systems are excellent model systems in which to study exchange-spring assisted magnetic reversal. In particular chapter 4 details magnetic reversal mechanisms studied by bulk magnetometry and x-ray magnetic circular dichroism (XMCD). The work is also complemented by micromagnetic modelling.

Microwave devices

The second main aspect of this thesis involves microwave devices which have great relevance for applications. These devices such as non-reciprocal oscillators/filters and planar microwave circuits are crucial components within WiFi, radar technology and data storage media.

Switching speeds for magnetic bilayers in data storage media is of particular importance. The magnetisation dynamics associated with a transition metal exchange-coupled bilayer (NiFe)/(CoFe) is presented and discussed in Chapter 5. This data is important in determining writing and switching speeds. Typical resonant frequencies for soft magnetic layers occur in the low GHz range but introducing anisotropic materials such as CoFe greatly increases the resonant frequency.

In the NiFe/CoFe bilayer, phase and amplitudes of the individual layers precessing in the presence of applied fields were determined using the new technique of x-ray detected ferromagnetic resonance (XFMR) at the Diamond Light Source.

Finally, some FMR and XFMR studies on microwave devices loaded with metamaterials [15-17] are described in Chapter 6. This is a new and exciting field of physics which will see many future applications. In particular, the problem of tune-ability of composite metamaterials in the GHz range is addressed by coupling the resonance of the metamaterial to that of a magnetic material such as yttrium iron garnet (YIG).

References

1. http://www-03.ibm.com/ibm/history/exhibits/storage/storage_350.html
2. R. Wood, J. *Magn. Mag. Mater.* **321,** 555. (2009).
3. C. A. Ross, *Annu. Rev. Mater. Res.* **31,** 203. (2001).
4. R. R. Rottmayer, S. Batra, D. Buechel, W. A. Challener, J. hohlfeld, Y. Kubota, L. Li, B. Lu, C. Milhalcea, K. Mountfield, K. Pelhos, C. Peng, T. Rausch, M. A. Seigler, D. Weller, and X. Yang, *IEEE Trans. Mag.* **42,** 2417. (2006).
5. R. C. O'Handley, *"Modern Magnetic Materials; Principles and Applications,"* Wiley Interscience (Wiley and Sons, Inc. 2000).
6. H. Zhou, and H. N. Bertram, *IEEE Trans. Mag.* **35,** 2712. (1999).
7. A. Moser, K. Takano, D. T. Margulies, M. Albrecht, Y Sonobe, Y. Ikeda, S. Sun, and E. E. Fullerton, *J. Phys. D: Appl. Phys.* **35,** R157. (2002).
8. D. Suess, T. Schrefl, R. Dittrich, M. Kirschner, F. Dorfbauer, G. Hrkac, and J. Fidler, *J. Mag. Mag. Mater.* **290,** 551. (2005).
9. H. Takano, Y. Nishida, A. Kuroda, H. Sawaguchi, Y. Hosoe, T. Kawabe, H. Aoi, H. Muraoka, Y. Nakamura, and K. Ouchi, *J. Magn. Mag. Mater.* **235,** 241. (2000).
10. X. Shen, M. Kapoor, R. Field, and R. H. Victora, *IEEE Trans. Mag.* **43,** 676. (2007).
11. http://www.computerlanguage.com/
12. D. Suess, T. Schrefl, S. Fahler, M. Kirschner, G. Hrkac, D. Dorfbauer, and J. Fidler, *Appl. Phys. Lett.* **87,** 012504. (2005).
13. J-. P. Wang, W. K. Shen, J. M. Bai, R. H. Victora, J. H. Judy, and J-. P. Wang, *J. Appl. Phys.* **97,** 10N513. (2005).
14. C. Wang, A. Kohn, S. G. Wang, and R. C. C. Ward, *J. Phys.: Condens. Matter.* **23,** 116001. (2011).
15. R. A. Shelby, D. R. Smith, S. Schultz, *Science.* **292,** 77. (2001).
16. D. Schurig, J. J. Mock, B. J. Justice, S. A. Cumer, J. B. Pendry, A. F. Starr, and D. R. Smith, *Science.* **314,** 977. (2006).
17. J. B. Pendry, A. J. Holden, D. J. Robbins, and W. J. Stewart, *IEEE Trans. Microw. Theory Tech.* **47,** 2075. (1999).

2. Theory

This chapter contains a brief review of the physics of magnetic films and multilayers covered in this thesis. In addition, the physical terms used in this thesis are defined.

2.1 Exchange interactions

The exchange energy arises from the Coulomb interaction between the electrons in accordance with the Pauli exclusion principle and is generally minimized when the spins of neighbouring electrons possess a parallel or antiparallel spin arrangement. The exchange Hamiltonian $\mathcal{H}_{ex}$ [1] takes the form,

$$\mathcal{H}_{ex} = \sum_{i<j} J_{ij} \bar{S}_i \cdot \bar{S}_j \qquad (2.1)$$

Here, J_{ij} is the exchange integral while $\bar{S}_i$ and $\bar{S}_j$ are two spins at lattice sites, i and j respectively. Frequently, the summation can be limited to 6 nearest neighbour interactions. Thus for $J_{ij}>0$ (<0) a parallel (antiparallel) alignment of spins is achieved respectively. The former gives rise to ferromagnetism while the latter gives rise to anti-ferromagnetism. This is not the case in pure rare-earth metals where complex spiral arrangements are frequently encountered [2].

Rare earth (*RE*) metals from the lanthanide group of the periodic table can be combined with transition metals such as iron (Fe) to form intermetallic cubic Laves phase compounds. Our research has concentrated on the *RE*Fe$_2$ compounds which possess the largest known magnetostriction [3], large magnetic moments per *RE* ion [4], and large crystalline magnetic anisotropies [5]. Considerable early work on bulk *RE*Fe$_2$ compounds has been reported by Buschow [6], Bowden [5], and Cohen [7].

In the *RE*Fe$_2$ compounds there are a number of magnetic exchange interactions which must be considered. They are, in order of decreasing strength the Fe-Fe strong ferromagnetic, the *RE*-Fe which is antiferromagnetic for the heavy *RE* (*e.g.* Gd, Dy, Ho, Er) and the *RE-RE* exchange interactions. Generally the *RE-RE* interaction is small, and is usually neglected. The two main exchange interactions occurring in the *RE* materials are outlined below:

Fe-Fe exchange

The Fe-Fe ferromagnetic exchange interaction (≈600 K) in *RE*Fe$_2$ intermetallic compounds arises from the exchange interactions between the 3*d* (4*s*) electrons of the transition metal ions [8]. This interaction is primarily responsible for the high Curie temperatures $T_C \approx 600$ K.

RE-Fe exchange

The *RE*-Fe exchange is an antiferromagnetic exchange (≈100 K) between the *RE* 4*f* magnetic moments and the Fe 3*d* moments. In *RE* metals the long range ordering is usually ascribed to the Ruderman-Kittel-Kasuya-Yosida model (RKKY) [9-11] where the 4*f* electrons polarize the 6*s* electrons. These weakly polarised conduction electrons then convey the spin information to other sites due to the extended wavefunctions. In the case of the *RE*Fe_2 intermetallics Campbell *et al*. [12] have proposed a model in which the exchange is primarily local, acting between 5*d* electrons on the *RE* ions and the 3*d* electrons on the Fe sites.

2.2 Magnetic order

In the absence of an external magnetic field, moments in paramagnetic materials are orientated randomly (except for short range order) with no spontaneous magnetisation. In contrast, ferromagnetic materials are characterised by a non-vanishing magnetisation arising from the spontaneous alignment of magnetic moments which in turn from the exchange interaction as described above. Ferrimagnetism can also occur as a result of the anti-parallel alignment of dissimilar magnetic moments [4]. Ferrimagnetism occurs in the rare-earth-iron compounds (*RE*Fe_2) and yttrium iron garnet (YIG) as discussed in Chapters 4 and 6. The long range magnetic ordering of the atomic moments for these materials occurs below their Curie or Neel temperature for ferromagnetic and antiferromagnetic/ferrimagnets respectively. The spontaneous long range magnetisation is observed to vanish causing the change from ordered magnetic states to paramagnetism.

2.3 Magnetic anisotropy

The anisotropy of a magnetic film is important. It determines: (*i*) the direction of preferred magnetisation, (*ii*) the precessional damping rate and (*iii*) the applied field required to switch the magnetic film. In general, there are three different anisotropies to be considered: (*i*) shape anisotropy, (*ii*) magneto-crystalline anisotropy and (*iii*) and exchange anisotropy [4]. The shape anisotropy depends upon the macroscopic shape of the sample and is closely related to the demagnetising field. The magneto-crystalline anisotropy arises from the interaction of the Fe 3*d* electrons and/or *RE* 4*f* electrons with the electric field gradients within the crystal structure. It is therefore dependent on the symmetry of the latter and gives rise to preferred directions of the magnetisation, often referred to as the ‘easy’ and ‘hard’ axes. If the magnetisation is aligned along an easy axis, such a state can be said to possess a high resistance to a change in applied field leading to a corresponding increase in the magnetic precession frequency. In contrast when the magnetisation is aligned along a hard axis the magnetisation is easily deflected away from the hard-axis leading to lower precessional frequencies. In general, the magneto-crystalline anisotropy energy can be measured by determining the strength of magnetic field required to magnetise the sample along its hard axis.

The *RE* Laves phase systems possess a large and complex anisotropy over that of transition metal films presented in this thesis. The *RE*Fe_2 series belong to the cubic $MgCu_2$ structure $O_h^7 - Fd3m$, with 8(16) *RE*(Fe) ions per unit cell *i.e.* 8 formula units (f.u) per unit cell. The structure per se can be seen in Figure 4.1 of Ch. 4.

In addition to large magnetic moments the *RE* ions in the *RE*Fe_2 Laves structure also possess very large magneto-crystalline anisotropies, this is due to the 4*f* electrons on the *RE* moment interacting with the principle axes of the crystal lattice. It is primarily the spin-orbit interaction which is responsible for magneto-crystalline anisotropy, this is much greater in the *RE*s than the transition metals due to a large *l*. An example of the magneto-crystalline anisotropies can be seen in Figure 2.1. The single crystal *RE* magnetic films used in this research were grown by MBE, (*vide infra* Ch. 3) meaning that the well understood single ion anisotropy is present across the entire sample. This makes the *RE* multilayer films an excellent model system to study the static and dynamic behaviour of multilayers.

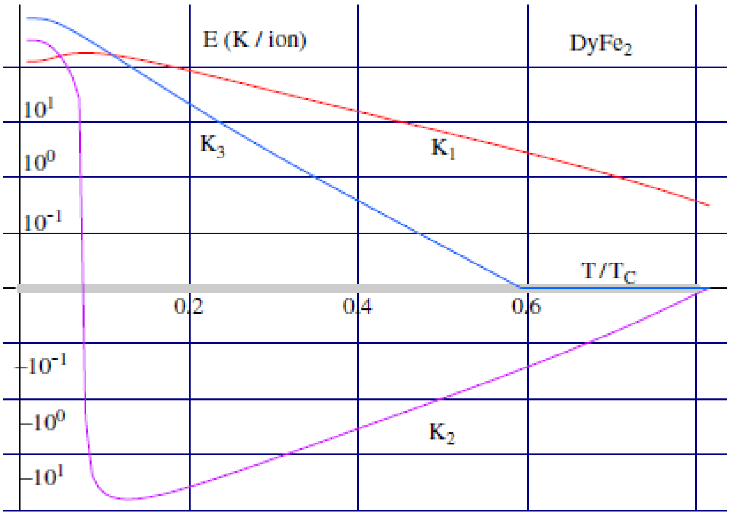

Figure 2.1: Calculated *RE*Fe_2 anisotropy parameters K_1, K_2 *etc.*, as a function of temperature for $DyFe_2$ [13].

In Figure 2.1 the temperature dependence of the first (K_1), second (K_2) and third (K_3) order temperature dependent (cubic) anisotropy constants can be seen for $DyFe_2$. Here we have used the phenomological form of the cubic crystal field anisotropy proposed by Atzmony and Dariel [14]:

$$E_{MC}(\overline{M},T) = K_1(\alpha_x^2\alpha_y^2 + \alpha_x^2\alpha_z^2 + \alpha_y^2\alpha_z^2) + K_2(\alpha_x^2\alpha_y^2\alpha_z^2) + K_3(\alpha_x^4\alpha_y^4 + \alpha_x^4\alpha_z^4 + \alpha_y^4\alpha_y^4) \tag{2.2}$$

where $\alpha_{x,y,z}$ are the direction cosines with respect to the magnetisation vector. The astonishing change of sign of the K_2 parameter is due to use of non-orthogonal components for K_1, K_2 and K_3, *i.e.* $K_1 = \alpha_x^2\alpha_y^2 + \alpha_x^2\alpha_z^2 + \alpha_y^2\alpha_z^2$ has a basis vector set which is different to that of K_2, $= \alpha_x^2\alpha_y^2\alpha_z^2$ and hence K_3. In general, the magneto-crystalline anisotropy energy in the *RE* materials is well described by the Callen-Callen model [15, 16] which reveals that the temperature dependence of the anisotropy parameters decrease monotonically with temperature.

The sign change of K_2 in Figure 2.1 is resolved if the anisotropy energy is expressed in terms of an orthogonal set of spherical harmonics as shown below,

$$E_A = F' + F'' = \tilde{K}_0(T)[Y_0^0(\theta,\phi)] + \tilde{K}_4(T)\mathbf{Y}_4^C + \tilde{K}_6(T)\mathbf{Y}_6^C + \tilde{K}_8(T)\mathbf{Y}_8^C + \tilde{K}_{10}(T)\mathbf{Y}_{10}^C + \tilde{K}_{12}(T)\mathbf{Y}_{12}^C \tag{2.3}$$

Here, the $\mathbf{Y}_4^C$ *etc.* are combinations of spherical harmonics with cubic symmetry. With this set of orthogonal harmonics the anisotropy parameters fall monotically with temperature as shown in Figure 2.2.

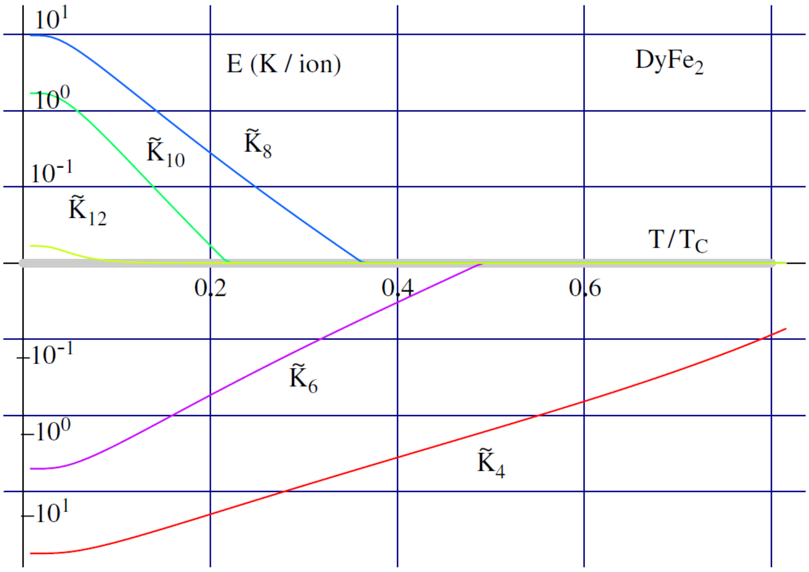

Figure 2.2: Calculated anisotropy constants $(\tilde{K}_4 - \tilde{K}_{12})$ for $DyFe_2$ plotted as a function of reduced temperature T/T_C. The thick line corresponds to the region $-10^{-2} \leq |\tilde{K}_i| \leq +10^{-2}$ [13].

In practice either set of the anisotropy parameters can be used. Finally, it should also be noted that if only the phenomonlogical terms K_1 and K_2 are considered the easy axes of magnetisation are either the [001], [101] or [111] directions. It has been shown by Atzmony and Dariel [14] and Bowden *et al.*, [17] that in the *RE*Fe_2 compounds the Callen and Callen model must be modified to include a K_3 term. The presence of this term gives rise to directions of magnetisation which do not lie along the principal cubic axes.

The dependence of the anisotropy parameters are given in Figure 2.2 show the anisotropy decreases with an increase in temperature as the magnetisation M(T) undergoes increasing thermal motion around its equilibrium and hence ‘samples’ more of the anisotropy surface thereby reducing the anisotropy strength [4]. The higher order anisotropy terms fall off faster with increasing temperature according to Akulovs law [18],

$$\frac{K_n(T)}{K_n(0)} = \left(\frac{M(T)}{M(0)}\right)^{n(n+1)/2} \qquad (2.4)$$

Equation 2.4 shows the dependence of anisotropy in ferromagnets, over a temperature range such that $\Delta M/M(0) \ll 1$. Here, M(T) is the magnetisation at temperature T and M(0) is the magnetisation at 0°K; K_n is the anisotropy constant for the nth order surface harmonic [19]. The REFe$_2$ systems studied in this thesis also possess a strain term in the anisotropy. This is a two-fold problem, firstly a lattice mismatch in the parameters of the substrate and the film. The lattice mismatch is $a_{RE\mathrm{Fe2}}$=0.733 nm for the REs and 0.4758 nm for Al_2O_3 and prevents the growth of the cubic Laves phase structure. However this can be alleviated by the seed and buffer layer as well as the growth temperature. Secondly the epitaxial growth of the Laves phase REFe$_2$ systems require that a growth temperature of 600 °C such that 2D growth is ensured (not 3D island growth). However the raised temperature during growth will then cause there to be an in-plane strain to form once cooled as the REFe$_2$ film and Al_2O_3 substrate have different thermal expansion coefficients.

2.4 *RE*Fe$_2$ magnetic moments

The magnetic moments which are used throughout this thesis, particularly in regards to the micromagnetic model, are values which are derived primarily from the ^{57}Fe Mössbauer data [5]. For the REFe$_2$ system covered in Ch. 4 the moments are as follows: μ_{Dy} = 10 μ_{B}, μ_{Er} = 9μ_{B} and 1.5 μ_{B} for Fe yielding a total magnetic moment of 7 μ_{B} at T = 0 K for $DyFe_2$ and 6μ_{B} for $ErFe_2$. Calculations by Brooks *et al* [21] deem it more appropriate to write μ_d (=$\mu_{3d} + \mu_{5d}$) = 1.5 μ_{B} in place of the discrete Fe moment of μ_{Fe} = 1.5 μ_{B}.

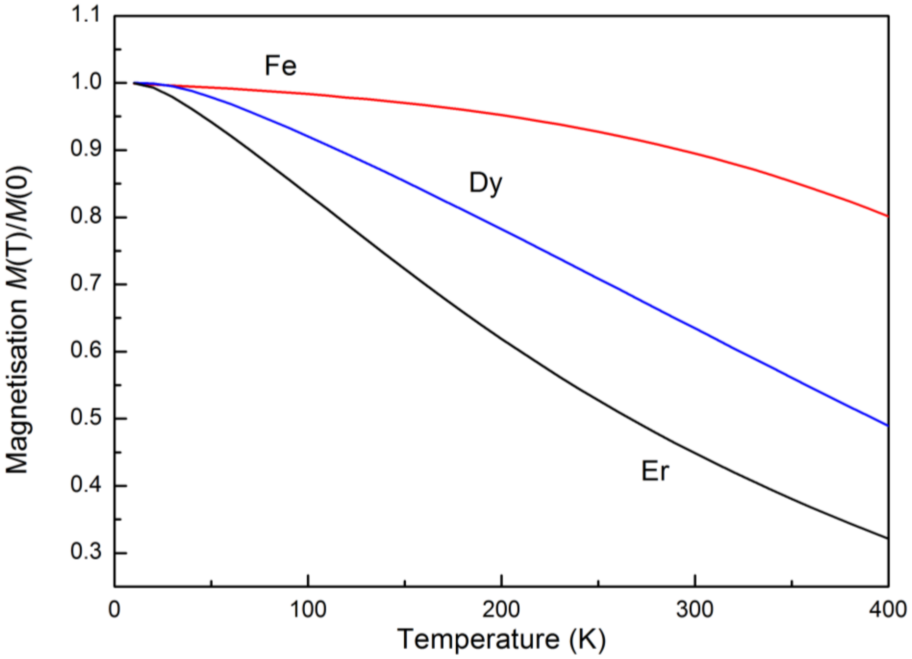

Figure 2.3: Magnetisation as a function of temperature

In Figure 2.3 the normalised magnetic moment of Dy, Er and Fe can be seen as a function of temperature in the range which was investigated by both XMCD and bulk magnetometry.

In the heavy rare earth systems the coupling mechanism is where the 5*d* electrons of the *RE* are antiferromagnetically coupled to the 3*d* moments of the Fe. The 5*d* electrons on the *RE* become polarised by the large moment on the 4*f* *RE* ions. The magnetic properties of the *RE*Fe_2 can be explained in terms of a 3*d*-5*d* interaction as a positive inter-ionic interaction between the Fe and the *RE* ions and the 5*d*-4*f* interaction between the *RE* 5*d* and 4*s* electrons as a negative intra-ionic [22].

2.5 Zeeman energy

In the description of magnetisation statics and dynamics the Zeeman energy of the system which describes the interaction of the magnetisation $\overline{M}$ with an external magnetic field $\overline{H}$ is of paramount importance [23, 24].

In general, we write:

$$E_{Zee} = -\mu_0 \int_V \overline{M} \cdot \overline{H} dV \qquad (2.5)$$

For a single spin with the applied magnetic field along the *z*-axis we can write:

$$E_{Zee} = -g\mu_B m_S H \qquad (2.6)$$

Where g is the gyromagnetic ratio and m_S is the magnetic quantum number which can take the values of ±1/2. The most energetically favourable state is reached when the magnetisation is aligned parallel to the magnetic field.

2.6 Demagnetising energy

The shape of the magnetic sample can also play a vital role. This is illustrated in Figure 2.4. When the magnetisation is aligned perpendicular to the film plane (Figure 2.4(a)) magnetic poles are created at the upper and lower surface of the film (emergence of flux lines from the surface). It costs energy to place the magnetic dipoles adjacent to each other such that they have the same orientation (Figure 2.4 (a)). This energy is stored in the fields about the dipole configuration. Dependent upon the shape of the sample, part of the dipolar field is through the sample, which acts to oppose the applied field which initially set up the 'free poles'. The energy becomes less when the dipoles are assembled head to tail with the field applied along the long axis (Figure 2.4 (b)) *i.e.* the magnetostatic energy [4]. From $\nabla \cdot \overline{B} = 0$ we find $\nabla \cdot \overline{H} = -\nabla \overline{M}$ which shows that the demagnetisation field is opposite to the direction of magnetisation inside the film. This field acts to demagnetise the sample. Hence, the origin of the term 'demagnetising field' $\overline{H}_{dem}$ [4, 23].

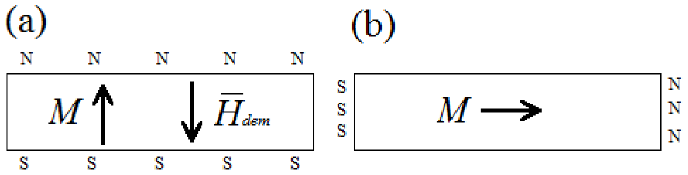

Figure 2.4: Cross section of a thin film showing (a) perpendicular alignment of magnetisation showing magnetic poles leading to demagnetising field. (b) Parallel alignment with negligible demagnetising effects.

By contrast when the magnetisation is in the film plane (Figure 2.4(b)) the demagnetisation field is negligible due to the large separation between the magnetic poles (large aspect ratio) at the small side surfaces. In both cases this is described in terms of surface charge as each magnetic pole within the film cancels with the pole adjacent to it.

In general, the energy associated with the demagnetising field takes the form:

$$E_{dem} = \frac{\mu_0}{2} \int_V \overline{M} \cdot \overline{H}_{dem} dV \qquad (2.7)$$

The integration is performed over the sample volume *V*. For ellipsoidal shaped samples, the demagnetising field is given by $\overline{H}_{dem} = N \cdot \overline{M}$ where *N* is a dimensionless demagnetising tensor, with the property Tr[N] = 1. Thus for an ellipsoid $N_x + N_y + N_z = -1$. For a thin film with large aspect ratio (see Figure 2.4(b)) the in-plane components of the demagnetising tensor are given by $N_x = N_y = 0$. Consequently the perpendicular component is $N_z = 1$.

2.7 Effective magnetic field

The total energy of a given magnetic system is obtained by adding various components, such as exchange energy, anisotropy energy and Zeeman energy. All these can be described in terms of an effective field acting on the magnetic system, as used, for instance in micromagnetic modelling. As shown in Eq. 2.8,

$$\overline{H}_{eff} = \overline{H}_a - \overline{H}_{dmag} + \overline{H}_{ex} + \overline{H}_{ani} + \overline{H}_{Zee} + \ldots \qquad (2.8)$$

Eq. 2.8 shows the effective field $\overline{H}_{eff}$ which is used instead of the magnetic energy and will be considered throughout this thesis. Many terms can be added to this summation dependent upon the individual magnetic sample and system, such as an additional field from exchanged bias systems or breaking down of more complex multilayer systems.

2.8 The equation of motion for magnets in a magnetic field

Magnetic resonance occurs when the magnetic selection rule $\Delta m_s = 0$ or ±1 is obeyed in conjunction with the Zeeman splitting, this then gives the allowed transitions arising from the splitting of the energy levels due to the applied field, below is the energy from Zeeman splitting taking $m_s = 0$,

$$h\omega_L = g\mu_B \overline{H}_{eff} \qquad (2.9)$$

Therefore, the atomic magnet will precess about the z-axis at the Larmor frequency ω_L this is the frequency of precession for the moment of an electron when subjected to a magnetic field.

From classical mechanics we find that when the magnetic moment m is deflected from its position of equilibrium (parallel to the effective magnetic field $\overline{H}_{eff}$) that the magnet will be subject to a torque [3, 25],

$$\overline{T} = \mu_0 \overline{M} \times \overline{H}_{eff} \qquad (2.10)$$

This torque, $\overline{T}$ will cause the magnetisation to precess around $\overline{H}_{eff}$ (z-axis) at the Larmor frequency ω_L. In practice the torque will give rise to a change in angular momentum of the magnet according to,

$$\frac{d\overline{M}}{dt} = -\gamma\overline{T} = -\gamma\mu_0 \cdot \overline{M} \times \overline{H}_{eff} \qquad (2.11)$$

Here γ is the gyromagnetic ratio defined by: $\gamma = \frac{g\mu_B}{\hbar}$, for a single spin. The situation is summarised in Figure 2.5 (a) [26].

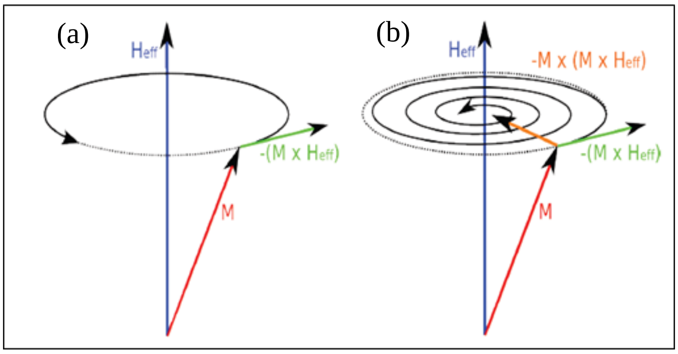

Figure 2.5: (a) Magnetisation $\overline{M}$ precessing about the effective field $\overline{H}_{eff}$. (b) The orange arrow shows the effect of the damping term (see Eq. 2.12) that is responsible for relaxing the magnetisation back into the direction of $\overline{H}_{eff}$.

Figure 2.5 (a) depicts the above-described dynamics, where once the magnetisation has started precessing it will continue indefinitely [27]. This is not the situation experimentally. In practice it is known that $\overline{M}$ returns to its equilibrium position along $\overline{H}_{eff}$ after a period, usually amounting to nanoseconds as shown in Figure 2.5 (b). Relaxation occurs as energy is transferred from the precessing magnet to the lattice via either the spin-lattice relaxation, mediated by the spin-orbit interaction, and/or spin wave excitations. In addition spins located in different parts of the magnet will interact via their mutual dipolar fields. All these features are taken into account in a phenomological way by the Landau-Lifshitz-Gilbert (LLG) equation of motion.

2.9 Landau-Lifshitz-Gilbert equation

The equation of motion which takes into account precessional damping of the magnetisation is the Landau-Lifshitz-Gilbert equation [28, 23],

$$\frac{d\overline{M}}{dt} = -\gamma\mu_0(\overline{M} \times \overline{H}_{eff}) + \frac{\alpha}{M_s}(\overline{M} \times \frac{d\overline{M}}{dt}) \qquad (2.12)$$

Here α is an intrinsic damping factor, which in most cases is smaller than 1 for ferromagnetic materials. The principle effect of damping on ferromagnetic resonance (FMR) is to increase the FMR FWHM (full-width-half-maximum) line-width. The first term in Eq. 2.12 represents the processional motion of the magnetisation vector about the applied field, while the second term describes the damping. The latter is highlighted in Figure 2.5 (b), where the orange arrow shows the return to the equilibrium state as a function of time.

In FMR the initial tipping of the magnetisation away from its equilibrium position is achieved by continuous excitation of a microwave rf field h_{rf}. The field $\overline{H}_{eff}$ determines the Zeeman energy level separation $\Delta E = g\mu_B\mu_0 H_{eff}$. The oscillating h_{rf} field excites transitions between the two Zeeman levels when the frequency of the microwave rf field obeys the condition $\hbar\omega = g\mu_B\mu_0 H_{eff}$. Typically FMR resonances are in the MHz and GHz range. Unlike nuclear spin systems it is not possible to drive the ferromagnetic spin system hard enough to produce 90° type rotations of the net magnetisation. Ferromagnetic resonance prevents this by breaking down into spin wave modes well before the magnetisation vector can be appreciably moved away from its equilibrium position [3]. This occurs due to FMR excitation frequency being a very narrow frequency range when in fact the FMR is much broader (due to inhomogeneous field *ect.*), to achieve 90° rotations a broader excitation frequency must be used. This is known as inhomogeneous broadening.

In practice, it is also necessary to take demagnetisation factors into account. These factors modify the internal field seen by the magnetic spins. Consequently, $B_x^i = B_x^0 - N_x M_x$ where B_x^i is the modified internal field. This applies also to both y and z axes. On substituting into equation 2.10 with (*i*) $N_x = N_z = 0$, $N_y = 1$ and (*ii*) B_0 is parallel to the plane of the sample we find [3],

$$\omega_0 = \gamma[B_0(B_0 + \mu_0 M_S)]^{1/2} \qquad (2.13)$$

Here ω_0 is the FMR frequency of the uniform mode where all the moments process together in phase and with the same amplitude. Other resonant modes will be considered in chapters 5 and 6. In contrast for B_0 applied perpendicular to the plane: $N_x = N_y = 0$, $N_z = 1$ which gives the ferromagnetic resonance condition as:

$$\omega_0 = \gamma(B_0 - \mu_0 M_S) \qquad (2.14)$$

Fundamentally in this thesis, we shall be primarily concerned with the in-plane FMR on thin film samples. This is when the magnetic field will be applied in-plane of the thin films due to the majority of magnetic films under investigation having an in-plane anisotropy.

References

1. P. A. M. Dirac, *Proc. R. Soc. Lond. A.* **123,** 714. (1929).
2. W. C. Koehler, *J. Appl. Phys.* **36,** 1078. (1965).
3. C. Kittel, "*Introduction To Solid State Physics, Eighth Edition,"* (Wiley and Sons, Inc. 2005).
4. R. C. O'Handley, *"Modern Magnetic Materials; Principles and Applications,"* Wiley Interscience (Wiley and Sons, Inc. 2000).
5. G. J. Bowden, D. St. P. Bunbury, A. P. Guimaraes, and R. E. Snyder, *J Phys. C.* **1,** 1376. (1968).
6. K. H. J. Buschow, *Rep. Prog. Phys.* **40,** 1179. (1977).
7. R. L. Cohen, *Phys. Rev.* **134,** A94. (1964).
8. M. B. Stearns, *Phys. Rev. B.* **8,** 4383. (1973).
9. M. A. Ruderman, and C. Kittel, *Phys. Rev.* **96,** 99. (1954).
10. T. Kasuya, *Prog. Theor. Phys. Rev.* **16,** 45. (1956).
11. K. Yosida, *Phys Rev.* **106,** 893. (1957).
12. I. A. Campbell, *J. Phys. F: Metal Phys.* **2,** L47. (1972).
13. K. N. Martin, P. A. J. de Groot, B. D. Rainford, K. Wang, G. J. Bowden, J. P. Zimmermann, and H. Fangohr, *J. Phys: Condens Matt.* **18,** 459. (2005).
14. U. Atzmony, and M. P. Dariel, *Phys. Rev. B.* **13,** 4006. (1976).
15. H. B. Callen, and E. Callen, *Phys. Rev.* **139,** A455. (1965).
16. H. B. Callen, and E. Callen, *J. Phys. Chem. Solids.* **27,** 1271. (1966).
17. G. J. Bowden, P. A. J. de Groot, B. D. Rainford, K. Wang, K. N. Martin, J. P. Zimmermann, and H. Fangohr, *J. Phys.: Condens. Matter.* **18,** 5861. (2006).
18. N. Akulov, *Z. Physik.* **100,** 197. (1936).
19. P.Pincus, *Phys. Rev.* **113,** 769. (1959).
18. A. Mougin, C. Dufour, K. Dumesnil, N. Maloufi, Ph. Mangin, and G. Patrat, *Phys. Rev. B.* **59,** 5950. (1999).
21. M. S. S. Brooks, L. Nordstrom, and B. Johansson, *J. Phys.:Condens. Matter.* **3,** 2357 (1991).
22. G. J. Bowden, A. R. Buckingham, G. B. G. Stenning, and P. A. J. de Groot, *J. Phys.:Condens. Matter.* **22,** 291001. (2010)
23. J. Stohr, and H. C. Siegmann, "Magnetism; From Fundamentals to Nanoscale Dynamics," (Springer, 2006).
24. P. Zeeman, *Phil. Mag.* **43,** 226. (1897).
25. C. Kittel, *Phys. Rev.* **73,** 155161. (1948).
26. C. Bilzer, *Ph. D. Thesis,* Universite of Paris, (2007).
27. L. Landau, and E. Lifshitz, *Phys. Z. Sowjetunion.* **8,** 153. (1935).

28. T. L. Gilbert. *Phys. Rev*. **100,** 1243. (1955).

3. Experimental techniques

The focus of this chapter is on the manufacture and experimental techniques needed to investigate thin magnetic films. In general, the growth and characterisation of thin films is much easier than that of their bulk counterparts, due to their extended 2D-nature. For magnetic films, the demagnetisation values are already well known (*ziede supra* Ch. 2, section 2.6). All the samples discussed in this thesis were grown by one of two methods: (*i*) molecular beam epitaxy for metallic films, and (*ii*) pulsed laser deposition for insulators.

Sample deposition

3.1 Molecular beam epitaxy

Molecular beam epitaxy (MBE) [1] is a well-established growth technique used to accurately deposit ultra-thin layers by elemental co-deposition at relatively low temperatures (≈500 ˚C). The technique was first used by Arthur *et al* [2] for semiconductor films. In general, MBE methods give rise to atomically sharp interfaces between adjacent layers in a multilayer system, essential for strongly exchange-coupled magnetic multilayer films [3]. In addition well defined stoichiometry leads to well-defined magnetic anisotropy. The metal films discussed in this thesis were all produced by MBE at the Clarendon Laboratory, Oxford. They were grown using a Balzers UMS 630 UHV MBE system [4] at elevated temperatures in ultra-high vacuum (UHV). The magnetic multilayer samples were grown with a substrate temperature of 500 to 600 °C at a base pressure of $\approx 10^{-11}$ mbar the low pressure was protected by passing samples through a load lock. Two different sources were used for co-deposition of material: effusion cells [5] and electron beam guns [6]. For the $RE\mathrm{Fe}_2/\mathrm{YFe}_2$ films, stoichiometric co-deposition of the elemental fluxes gives rise to very clear interfaces between the $RE\mathrm{Fe}_2$ and YFe_2 layers. (Ch. 4). Shutters for both the effusion and electron-beam guns can open/close in a few micro-seconds.

Co-deposition produces good quality samples as the stoichiometry can be controlled to ~1%, this is difficult to achieve in a sputtering rig. For example, if an alloy target is used with the composition $\mathrm{Ni}_{0.81}\mathrm{Fe}_{0.19}$, the resultant film may possess a different stoichiometry due to differing elemental sputtering rates which are dependent upon the growth conditions. However with MBE, co-deposition of the elemental fluxes can be adjusted simultaneously to always yield the desired composition (*e.g.* $\mathrm{Ni}_{0.81}\mathrm{Fe}_{0.19}$) [5] as well as epitaxial growth. To ensure that the stoichiometry is indeed correct, in-situ measurement was performed using reflection high energy electron diffraction (RHEED) [6]. This also provides a real-time view of the surface crystallography as the film is being grown.

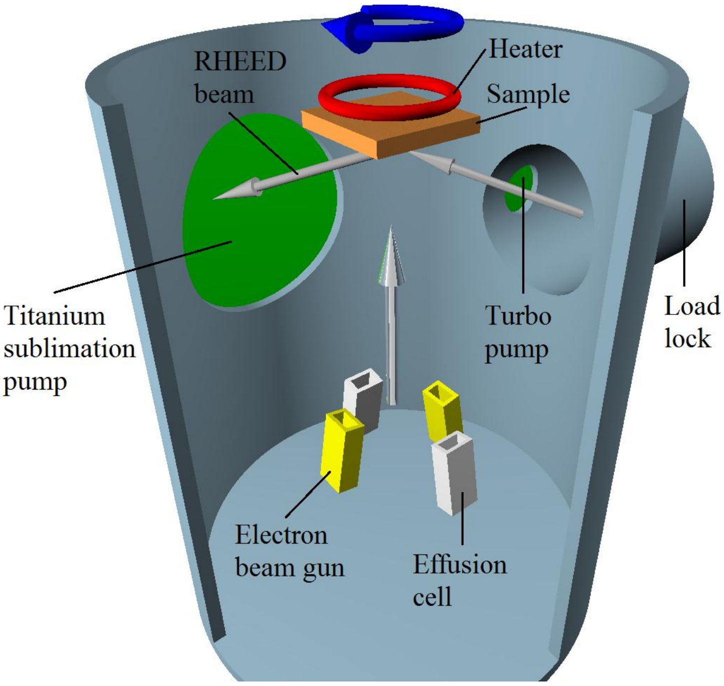

Figure 3.1: Schematic of a chamber of the Balzers 630 UHV MBE experimental chamber.

Figure 3.1 shows the arrangement within the MBE main chamber. Rotation of the sample (blue arrow) is used to achieve an even deposition of the material. The magnetic multilayer samples were grown either on epi-prepared $(11\bar{2}0)$ sapphire (Al_2O_3) or a single crystal magnesium oxide (MgO) substrate. In all of the films, seed layers were deposited before the magnetic films were grown to promote high quality epitaxial growth.

The MBE samples discussed in this thesis [9-11] can be separated into two groups: (*i*) the Laves-phase *RE*Fe_2 and (*ii*) transition metal films. More details are given in Ch. 2 and 3, respectively. The *RE*Fe_2 superlattice samples discussed in this thesis possess the following compositions:

(*i*) Al_2O_3/Nb (100 Å)/Fe (20 Å)/[$ErFe_2$ (70 Å)/YFe_2 (150 Å)]×25/Y (100 Å)

for spin-flop transitions (Ch. 4 section 4.2) [11] and:

(*ii*) Al_2O_3/Nb (100 Å)/Fe (20 Å)/[$DyFe_2$ (60 Å)/YFe_2 (240 Å)]×15/Nb(100 Å)

for transverse exchange springs (Ch. 4 section 4.4) [10, 11]. Here the Nb and Fe act as buffer and seed layers respectively, grown on top of the Al_2O_3 substrate. The capping layer of either Y or Nb was chosen to prevent the rapid oxidation of the magnetic films.

3.2 Transition metal films

The transition metal films investigated during the course of this work are (*i*) NiFe, (*ii*) CoFe and (*iii*) a bilayer combining NiFe/CoFe. Taken separately the crystal-structures of NiFe and CoFe are FCC and BCC respectively [12, 13]. Both the Ni and Fe moments, and Co and Fe moments are coupled ferromagnetically. The magnetic bilayer, which is the main focus of the transition metal samples discussed in this thesis (see Ch. 5) were grown epitaxially on a (001)-MgO substrate, using a buffer and seed layer Fe (30 Å)/Pt (300 Å). The latter acts to offset the lattice mismatch between the MgO and the magnetic layers. This was followed by the actual bilayer [NiFe (400 Å)/CoFe (400 Å)]. Finally, to prevent oxidation the samples were capped with 50 Å of Pt. The bilayer was grown with an in plane magnetic field 0.02 T applied along a [110] in-plane axis. A schematic diagram of the sample structure can be seen in Figure 3.2.

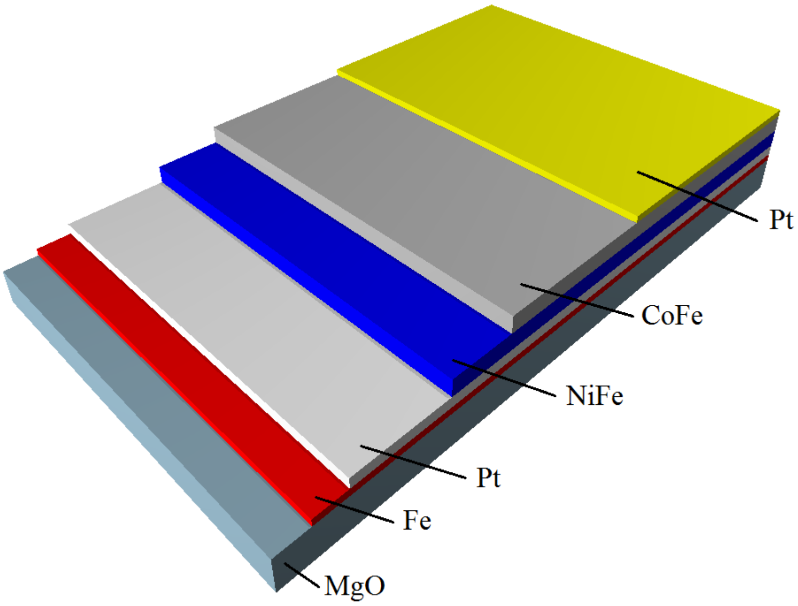

Figure 3.2: Schematic showing the various layers of a transition metal bilayer NiFe/CoFe structure. The Fe and Pt act as the seed and buffer layer respectively with the topmost Pt as the protective cap.

Samples were also produced with an additional IrMn (100 Å) layer placed just before the NiFe/CoFe bilayer. The effect of the IrMn layer is to subject the bilayer to an exchange bias, thereby shifting the magnetic hysteresis loop (and the ferromagnetic resonance) either to the right or left along the field axis however, this was observed to be a small effect.

3.3 Pulsed laser deposition

Pulsed laser deposition (PLD) is a thin film deposition technique which can be used to manufacture a wide range of materials [14]. Cubic materials such as garnets have been successfully grown by PLD [15]. The garnet grown by PLD for this investigation was yttrium iron garnet (YIG – $Y_3Fe_5O_{12}$) [16]. PLD uses a high power laser beam focused onto a target material. The focused laser vaporises the target material into a plasma plume which then expands away from the target surface, interacting with the chamber atmosphere until it is finally deposited as a thin film onto a substrate (some 6 cm away). The laser used to ablate the single crystal YIG target was a KrF excimer operating at 248 nm [17] with a 20 ns pulse duration at a repetition rate at 20 Hz and energy-fluence of 3 Jcm^{-2}. The experimental chamber base pressure is $\approx 10^{-3}$ mbar but subsequently backfilled with 10^{-2} mbar of oxygen. The chamber has multiple sources allowing for doped films and multilayers. The YIG film is deposited on a single crystal yttrium aluminium garnet (YAG) (100 orientated) substrate at a temperature of ≈750 °C. Since this value depends upon the power of the CO_2 laser aimed at the substrate for heating purposes it is only an approximate value. The YAG substrate was chosen to achieve a reasonably good lattice match to the YIG [17]. The benefit of this technique is rapid sample-growth enabling films several μm thick to be produced in a very short time.

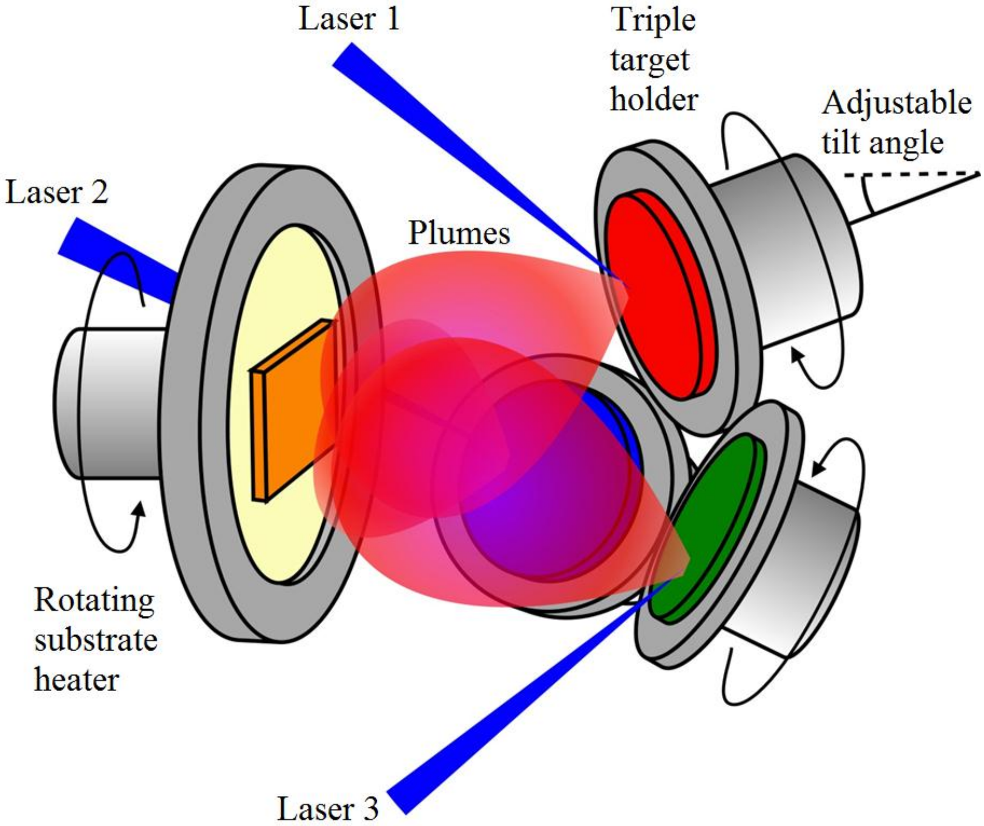

Figure 3.3 Schematic showing the PLD of a YIG-film with rotation of the sample to ensure even growth.

Additional plumes of material are shown in Figure 3.3 to highlight the possibility of either multilayer growth or, say, YIG doped with either Bi or increased Fe-content. The YIG films were grown in the Opto-electronics Research Centre at Southampton University by Alberto Sposito. They were subsequently investigated and optimised using ferromagnetic resonance (FMR) spectroscopy (see section 3.6). In general, the narrower the resonance the better the film. The results are summarised in Figure 3.4.

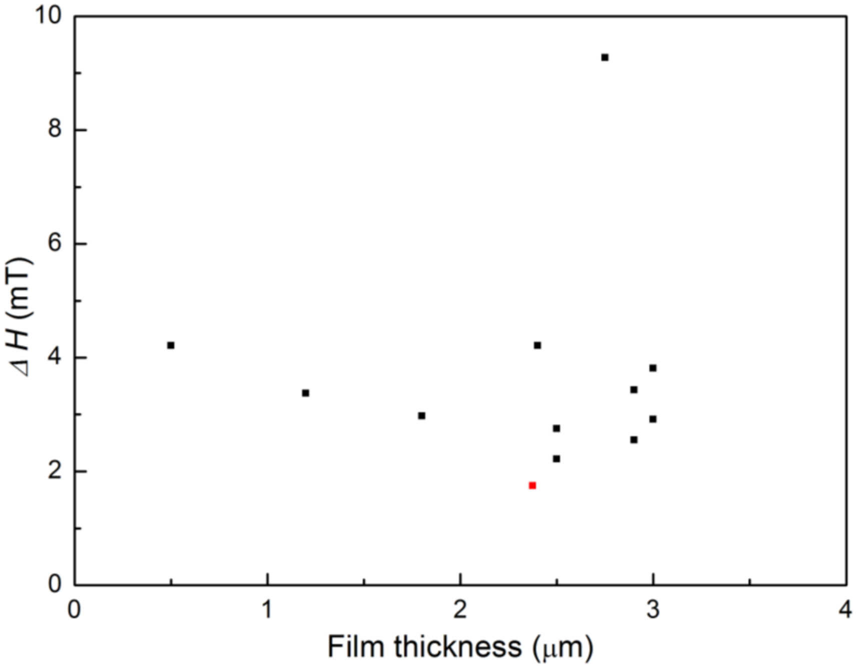

Figure 3.4: The full-width half-maximum (ΔH) of the ferromagnetic resonance of several YIG films as a function of film thickness. The red data point is the YIG film with the narrowest linewidth.

FMR measurements have been used in the past as the basis for optimisation/comparison of YIG films. In particular a narrow linewidth of 0.02 mT has been achieved in bulk YIG [18]. In general narrow linewidths and small damping are important in applications. It should also be noted that in addition to optimising the thickness of YIG films further experiments involving differing oxygen pressures, substrates and Fe content were also performed.

Experimental methods

3.4 Vibrating sample magnetometer (VSM)

The vibrating sample magnetometer (VSM) is one of many standard tools for characterising magnetic films and bulk materials.

The sample under investigation is placed in the centre of a homogenous applied magnetic field close to a pair of pick up coils. A vibrator is used to drive the sample sinusoidally in a vertical direction typically at a frequency of 10-100 Hz. The vertical movement of the magnetised sample gives rise to a change of the flux (φ) within the pick-up coils. This in turn induces an electromotive voltage,

$$\varepsilon = \frac{\partial \varphi}{\partial t} \qquad (3.1)$$

A more complete derivation can be found by Beaujour [19], which reveals that the induced electromotive voltage is given by,

$$\varepsilon = z_a \omega m \sin(\omega t) G(z_0) \qquad (3.2)$$

Here m is the magnetic moment, ω is the angular frequency of vibration, t is time and G defines the sensitivity, which depends in part on the position of the sample with respect to the pick-up coils. Generally, G is obtained experimentally using a calibrated sample of known magnetic moment.

Two different VSMs were used in the course of this work. The first was an in-house superconducting-magnet VSM Oxford Instruments Aerosonic 3001 magnetometer capable of fields of up to ±12 T. The second was a Quantum Design MPMS SQUID [20] VSM with a maximum field strength of ±7 T. Both of these systems possess a temperature range of 2-300 K. The sensitivity of the two systems was

1×10^{-6} emu (5×10^{-8} emu) for the Aerosonic and SQUID VSMs respectively. In general, VSM measurements were used as a means of characterising the magnetic films, prior to synchrotron measurements such as XMCD (Ch. 4) or XFMR (Ch. 5).

3.5 VNA-FMR

Vector network analyser-ferromagnetic resonance (VNA-FMR) is a continuous wave (CW) technique which probes magnetisation dynamics in thin magnetic films via FMR. The method employs the use of a coplanar waveguide (CPW) and vector network analyser (VNA) to both drive and monitor the properties of a loaded CPW as a function of frequency and applied magnetic field. The applied magnetic field was supplied by an electromagnet driven by a computer controlled DC bipolar power supply. The magnetic field strength was recorded using a Lakeshore 425 Hall probe situated close to the sample. The microwave rf field, applied to the CPW was delivered by a 20 GHz vector network analyzer (VNA) (HP E5071C) through low loss broadband cables. The microwave circuit can be described as a two port transmission measurement system. The cables were inserted through the centre of the electromagnet pole pieces and connected to the coplanar waveguide (CPW) using end launch connectors. The CPW signal line width and gap size were set at 1.1 mm and 200 μm respectively, as shown in Figures 3.5 and 3.6.

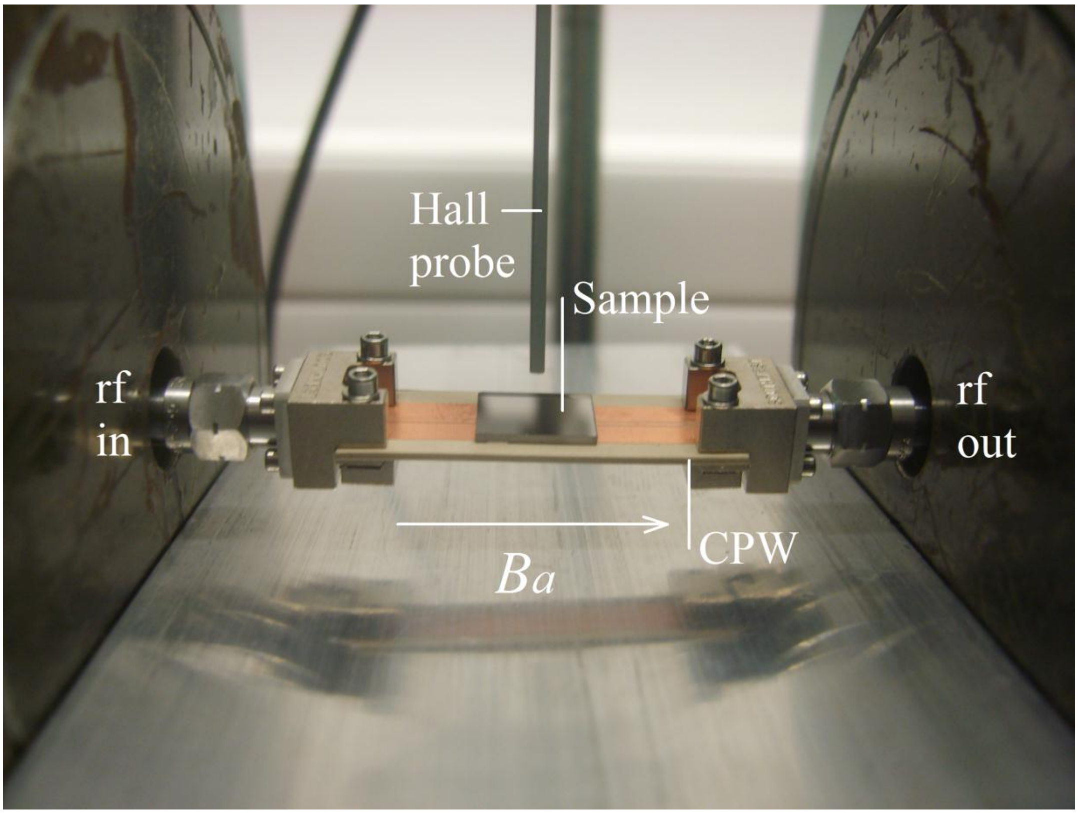

Figure 3.5: Photograph of VNA-FMR experimental arrangement.

The dimensions of the CPW permit a broadband frequency device in the 1-20 GHz range with 50 Ω impedance. Matching the 50 Ω impedance required the use of specialist software [21], inclusion of vias [22], and tapering of the signal line. The final arrangement can be seen in Figure 3.6 below. The CPW yielded a clear microwave response up to frequencies of 25 GHz.

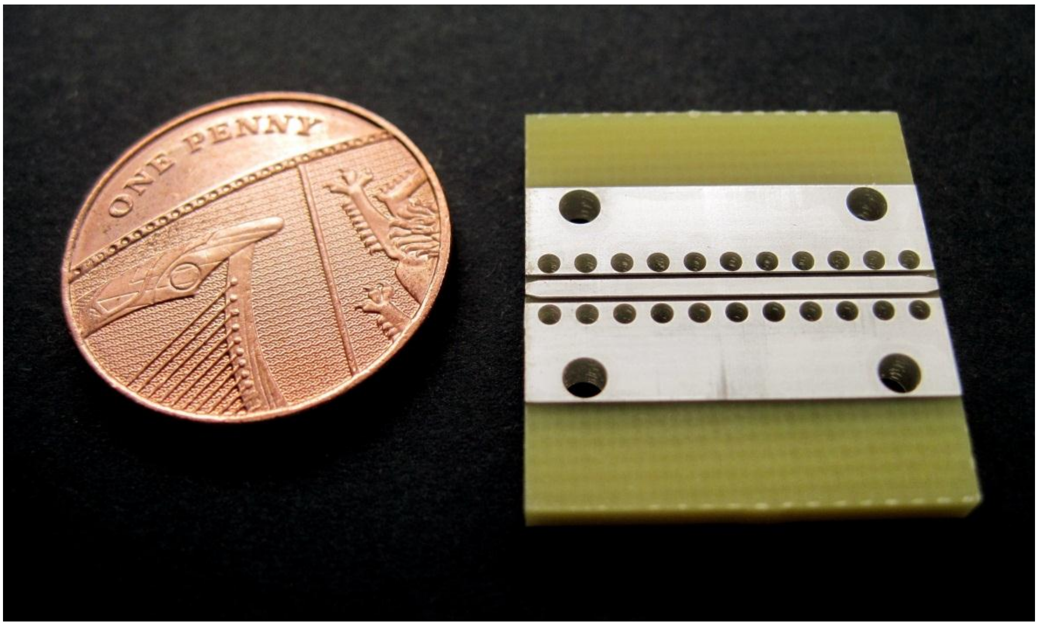

Figure 3.6: Photograph of optimised CPW shown next to a penny for scaling.
Signal line width 1.1 mm, gap size 200 μm.

The VNA provides a frequency sweep from 300 kHz to 20 GHz while simultaneously monitoring microwave transmission properties over this range. The CPW permits a transverse electromagnetic (TEM) geometry. The magnetic film is placed ‘flip chip’ [23] on top of the waveguide enabling strong coupling to the CPW and good microwave excitation. The CPW was fabricated using a simple mask/photo-etching technique. A 70 µm copper layer on both sides of a 0.7 mm thick dielectric sheet was used as the substrate (FR4, $\varepsilon_r = 4.5$). The VNA allows for collection of the S-matrix (Scattering-Matrix) parameters including the transmission coefficient S_{21}. In particular the latter details the transmission properties of the CPW loaded with a magnetic film and/or a split ring resonator (see Ch. 6).

The results from VNA-FMR experiments are usually presented in a 2D map of frequency *vs.* field map (ν-B_a). This measurement is a frequency sweep taken at multiple applied fields which are then collated together into a 2D plot. The colour at a given point in the 2D-map represents the magnitude of S_{21}. It should be noted that the S_{21} map plots presented in this work were normalized by subtracting the S_{21} transmission obtained in very small magnetic fields ($B_a = 0.001$ T) from every subsequent frequency sweep. This gives $\left|S_{21}^{N}\right|$, leaving only the field dependent features in the resultant 2D-plot. Examples of these can be seen in Ch. 5. Measurements were also obtained by fixing the excitation frequency of the VNA and sweeping the magnetic field (fieldsweeps), such measurements allow the FMR linewidth to be examined in more detail and alleviate any problems arising from resonant modes from the experiment as the CPW is an effective microwave cavity (field independent features).

3.6 Metamaterial VNA-FMR

The experimental technique for investigating metamaterials can be described as a variation on the VNA-FMR method. On this occasion, the CPW is loaded with a split ring resonator (SRR) fabricated on the underside of the CPW. A single SRR can be thought of as a single metamolecule (see Ch. 6). The CPW/SRR technique was pioneered by Martin *et al.* [24] and Falcone *et al.* [25] who showed that SRR systems can be studied and exploited in a coplanar arrangement. Figure 3.7 illustrates the experimental arrangement showing the SRR on the underside of the CPW substrate directly underneath one of the gaps of the CPW. This arrangement maximises rf coupling between the CPW and SRR. The dimensions of the SRR used in this work are also shown in Figure 3.7. It is similar to a design given by Shelby *et al.* [26].

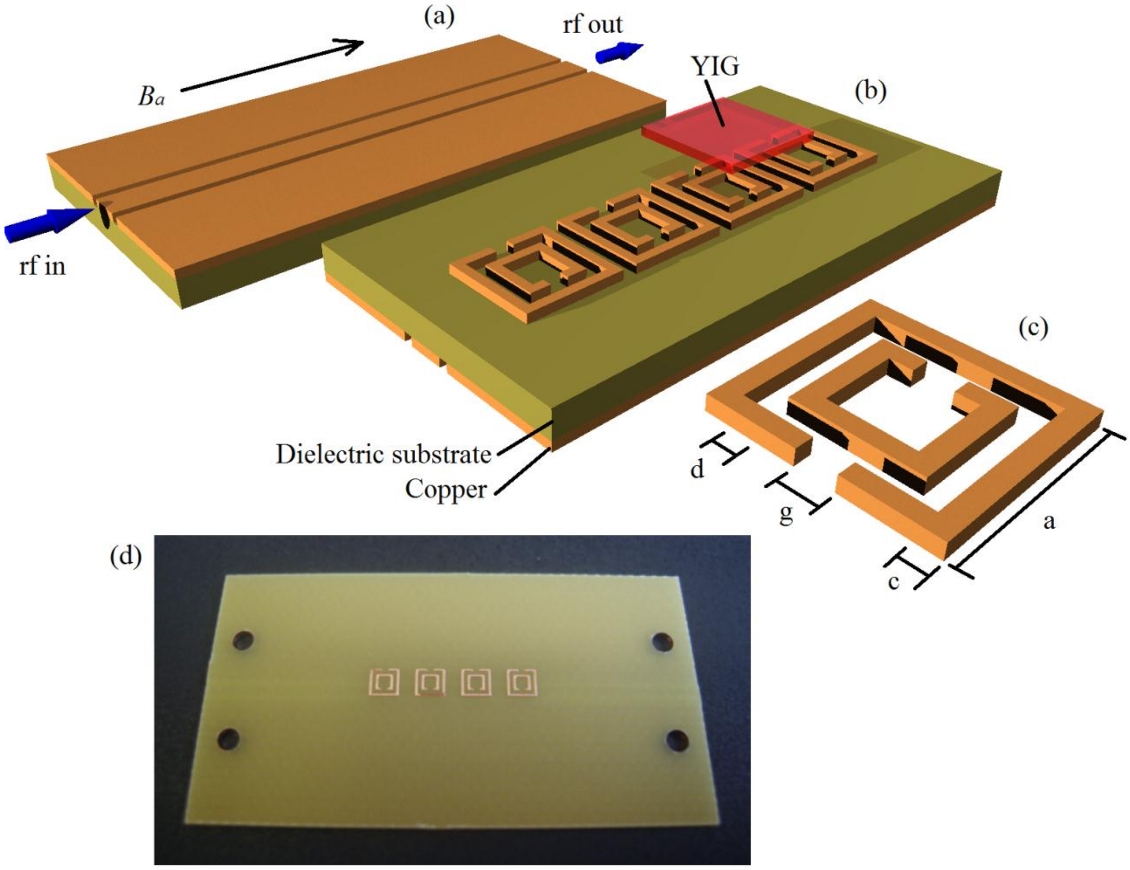

Figure 3.7: Schematic/photograph of (a) top view of the CPW, (b) SRRs (metamaterial) located on the underside of the CPW substrate. The YIG film is placed directly on top of one SRR. (c) Single SRR. Dimensions: a = 3.93 mm, c = 0.375 mm, d = 0.45 mm, g = 0.69 mm. (d) photograph of metamaterial. Field direction as shown by B_a.

The CPW can just be seen through the FR4 substrate in Figure 3.7(d). The FMR film is placed ‘flip chip’ on one of the SRRs. The TEM from the CPW excites both the SRR and the magnetic material. Measurements of $\left|S_{21}^{N}\right|$ are then conducted in the same way as for standard VNA-FMR 2D-maps. Examples of these can be seen in Ch. 6.

3.7 Cleanroom sample fabrication

With all the magnetic films some pre-processing is necessary before characterisation. This includes simply cutting the sample to the required shape either to allow for mounting into the VSM or VNA-FMR or for more complex ‘patterning’. Cutting the films was performed using a diamond tipped cutting blade, ensuring a clean cut across the film and hard substrate.

Patterning of the sample into a CPW is an essential prerequisite for x-ray ferromagnetic resonance studies (XFMR). For such experiments, low energy x-rays must be able to penetrate the magnetic film. This means the sample must be patterned into a CPW rather than using a 'flip chip' method to allow for x-ray transmission. Patterning into a CPW also has the advantage of increasing the rf coupling into say the NiFe/CoFe magnetic bilayer.

The above work was carried out in the University of Southampton nanofabrication centre. In the first instance, roughly a 100 nm thick layer of Cu was deposited on top of the magnetic bilayer. This is to favour the *in-phase* excitation of the magnetic bilayer via the Cu layer rather than the microwave excitation propagating through the magnetic material. The Cu deposition was performed using an Edwards Auto 500 electron beam evaporator. The base pressure reached was ≈10^{-6} mbar.

The patterning used in this work can be described as an etching back photolithography process as opposed to a lift-off technique [27]. A photoresist is patterned into the desired shape which is then used as a mask to etch back through the whole sample. The process is as follows. Photoresist (S1813) [28] is spun on top of the newly deposited Cu layer, spinning at 5000 rpm for 60 s. This produces an even coating of the resist across the sample with a uniform thickness of 1.3 μm. S1813 is a 'positive' resist, so the resist which is exposed to UV light will be removed. (A negative resist would do the opposite). The sample is then baked for 30 min at an elevated temperature of 90°C to ensure the majority of solvents are successfully removed from the film. The sample at this stage is shown in Figure 3.8(b).

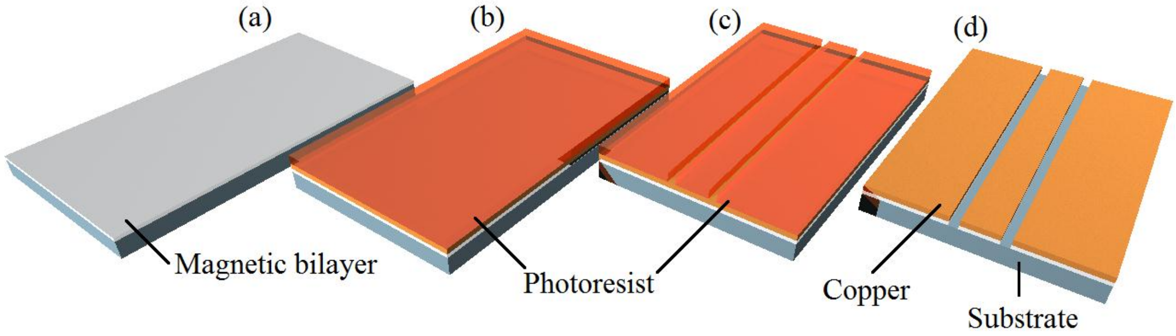

Figure 3.8: Shows the four main steps in the patterning of a metallic film. (a) as grown magnetic film. (b) Photoresist atop the magnetic film. (c) Photoresist patterned into CPW. (d) CPW etched through to the magnetic film.

Before patterning can take place a photolithography mask must first be designed (this is covered in more detail in Ch. 5). Given such a mask, UV exposure through the mask into the photoresist is accomplished with the aid of a Karl-Suss MA6 double sided mask aligner. Carefully controlling the exposure time and type (12 s exposure and hard contact respectively [29]) the exact patterns/dimensions, can be achieved. Optimisation is required to avoid under- or over-exposure of the resist [27].

The next stage is to remove the resist which has been exposed to UV thereby leaving only the required patterned structure. The exposed resist is removed by submerging the resist/sample in a MF319 (a developing agent [30]) which removes only the polymerised resist. At this stage the sample looks like the schematic drawing shown in Figure 3.8 (c).

Next, it is necessary to embed the pattern into the magnetic film itself. This is achieved by placing the sample with the patterned resist into an ion etcher (Ionfab 300 Plus reactive ion beam etcher). Energetic Ar ions bombard the sample removing all material. However as the resist is 1.3 μm thick and the magnetic bilayer sample is 40 nm thick, even with the etch rates being very different the ratio of the thicknesses is sufficient to etch all the way through the bilayer through to the MgO substrate leaving only the pattern and resist.

The resist is completely removed by placing the sample in a solvent leaving the patterned film as shown in Figure 3.8(d). However, for XFMR experiments, an additional step is required. The sample must be mounted into a regular plastic circuit board (PCB) CPW (Figure 5.8) to allow for CPW microwave excitation. This enables the microwaves to be supplied to the CPW patterned on the sample with a high power, while still maintaining the x-rays on the signal line of the CPW for detection. A sonic wire bonder, 40 μm Al wires are bonded from the CPW patterned sample to the PCB signal and ground planes respectively on the PCB CPW, thereby enabling microwave excitation across the sample.

3.8 Synchrotron radiation

The experimental technique which envelopes the use of synchrotron facilities, such as x-ray magnetic circular dichroism (XMCD) and x-ray detected ferromagnetic resonance (XFMR), will be covered in much greater detail in chapters 4 and 5.

References

1. A. Y. Cho, and J. R. Arthur, *Phys. Rev. Lett.* **22,** 1180. (1969).
2. J. R. Arthur. *J. Appl. Phys.* **39,** 4302. (1968).
3. K. Dumesnil, M. Dutheil, C. Dufour, and Ph. Mangin, *Phys. Rev. B.* **62,** 1136. (2000).
4. http://www2.physics.ox.ac.uk/research/thin-film-quantum-materials/growth-facilities
5. A. Schuhl, P. Galtier, O. Durand, J. R. Childress, and R. Kergoat, *Appl. Phys. Lett.* **65,** 913. (1994)
6. Y. Horio, Y. Hashimoto, A. Ichimiya, *Appl. Surf. Sci.* **100,** 292. (1996).
7. M. J. Bentall, R. C. C. Ward, E. J. Grier, and M. R. Wells, *J. Phys.: Condens. Matt. Phys.* **15,** 6493. (2003).
8. C. Wang, A. Kohn, S. G. Wang, and R. C. C. Ward, *J. Phys.: Condens. Matter.* **23,** 116001. (2011).
9. G. B. G. Stenning, A. R. Buckingham, G. J. Bowden, R. C. C. Ward, G. van der Laan, L. R. Shelford, F. Maccherozzi, S. S. Dhesi, and P. A. J. de Groot, *Phys Rev. B.* **84,** 104428. (2011).
10. G. B. G. Stenning, G. J. Bowden, S. A. Gregory, J. –M. L. Beaujour, A. N. Dobrynin, L. R. Shelford, P. Bencok, P. Steadman, T. Hesjedal, G. van der Laan, P. A. J. de Groot, *Appl. Phys. Lett.* **101,** 072412. (2012).
11. G. B. G. Stenning, G. J. Bowden, S. A. Gregory, A. N. Dobrynin, L. R. Shelford, P. Bencok, P. Steadman, T. Hesjedal, G. van der Laan, P. A. J. de Groot, *Phys. Rev. B.* **86,** 174420 (2012).
12. R. C. O'Handley, *"Modern Magnetic Materials; Principles and Applications,"* Wiley Interscience (Wiley and Sons, Inc. 2000).
13. K. H. J. Buschow, "*Handbook of Magnetic Materials; Vols 1-20*" (North Holland, 2013)
14. R. W. Eason, "Pulsed Laser Deposition of Thin Films – Applications-led Growth of Functional Materials," (Wiley Interscience, 2007).
15. N. A. Vainos, C. Grivas, C. Fotakis, R. W. Eason, A. A. Anderson, D. S. Gill, D. P. Shepherd, M. Jelinek, J. Lancok, and J. Sonsky, *Appl. Surf. Sci.* **127**, 514. (1998).
16. M. B. Park, B. J. Kim, and N. H. Cho, *IEEE Trans. Magn.* **35,** 3049. (1999).
17. A. Sposito, T. C. M. –Smith, G. B. G. Stenning, P. A. J. de Groot, and R. W. Wason, *Opt. Mater. Express.* **3,** 624. (2013).
18. C. Kittel, "*Introduction To Solid State Physics, Eighth Edition,"* (Wiley and Sons, Inc. 2005).
19. J. –M. L. Beaujour, *Ph. D. Thesis*, University of Southampton, UK (2003).
20. http://www.qdusa.com/sitedocs/productBrochures/1500-102.pdf
21. http://www.awrcorp.com/
22. http://mpd.southwestmicrowave.com/

23. J. M. L. Beaujour, A. D. Kent, D. W. Abraham, and J. Z. Sun, *J. Appl. Phys.* **103,** (2008).
24. F. Martín, F. Falcone, J. Bonache, R. Marqués, and M. Sorolla, *IEEE Microw.Wireless Compon. Lett.* **13,** 511. (2003).
25. F. Falcone, F. Martín, J. Bonache, R. Marqués, and M. Sorolla, *Microw. Opt. Technol. Lett.* **40,** 3. (2004).
26. R. A. Shelby, D. R. Smith, S. C. Nemat-Nasser, and S. Schultz, *Appl. Phys. Lett.* **78,** 489. (2001).
27. A. R. Buckingham, *Ph. D. Thesis*, University of Southampton, UK (2010).
28. http://www.nanophys.kth.se/nanophys/facilities/nfl/resists/S1813/s1800seriesDataSheet.pdf
29. http://microlab.berkeley.edu/labmanual/chap4/ksaligner.pdf
30. http://www.first.ethz.ch/infrastructure/Chemicals/Photolithography/Data_MF319.pdf

4. X-ray studies of magnetic exchange springs in *RE*Fe_2 thin films

The properties and the possible uses of exchange springs in modern day applications are presented and discussed. Investigations into the switching and reversal mechanisms, and the processes which govern them, were performed. Bulk magnetometry and soft x-ray experiments at synchrotron light sources were used to unravel the states of exchange springs that can be seen in *RE*Fe_2/YFe_2 multilayer systems.

4.1 History of magnetic exchange springs

Magnetic exchange springs can be set up in magnetic multilayers with alternating hard and soft magnetic layers. These have attracted a great deal of attention over the years for potential applications in data storage media [1-3], permanent magnets [4, 5] and MEMS [6-8]. Coupling hard magnetic layers to a magnetically soft one was first considered by Kneller *et al* [9]. It was suggested that alternate hard, soft layers which are ferromagnetically coupled could lead to significantly stronger magnets. Laves phase materials of the form *RE*Fe_2 (see Ch. 2) exhibit model magnetic exchange springs. Such spring systems have been the focus of much research over the past few decades, building upon the very early work on bulk *RE*Fe_2 of Bowden [10], Buschow [11] and Cohen [12].

The Laves phase structure shown in Figure 4.1 [13] is the classic $MgCu_2$ type cubic lattice. The *RE* (*RE* = rare earth, *e.g.* Er, Dy and Y) ions are represented by the white spheres which possess cubic symmetry (8 per unit cell), whereas the Fe ions form a tetragonal symmetry (16 per unit cell) are represented by the blue spheres. Lattice parameters and details can be found in Beaujour *et al* [14].

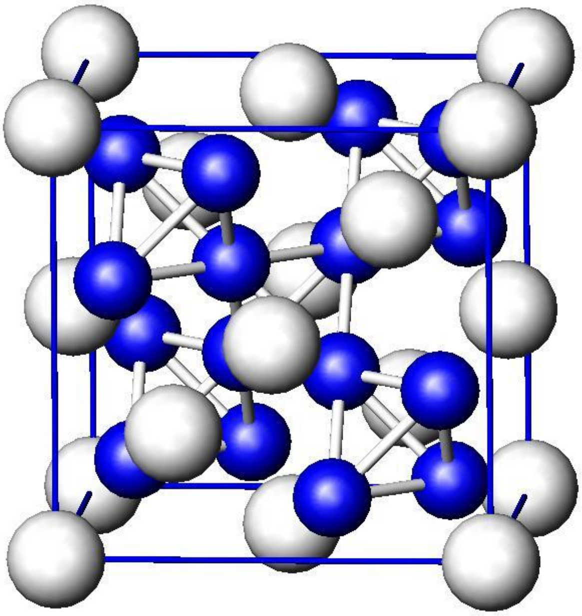

Figure 4.1: Diagram of the cubic Laves phase *RE*FE_2 structure [13]. White (Blue) spheres represent the *RE* (Fe) elements respectively.

Consider an exchange spring where the hard and soft layers are ferromagnetically coupled as shown in Figure 4.2. It has been shown that below a critical applied field the magnetisation of the hard magnetic layer remains pinned along an easy-axis of magnetisation while the soft layer magnetisation is able to rotate relatively freely. If the thickness of the soft layer is d, the applied field required to initiate soft-layer rotation is known as the 'bending field' (B_B) [15].

$$B_B \propto {}^{1}\!/_{d^2} \qquad (4.1)$$

A schematic illustration of a REFe$_2$/YFe$_2$ exchange spring can be seen in Figure 4.2. The hard antiferromagnetic RE-Fe layers are represented by the top three blue-red arrows respectively, these are coupled to the soft ferromagnetic YFe$_2$ layers (red arrows only). Given that the hard REFe$_2$ are prepared to be aligned with an easy axis, an applied field will cause the soft magnetic layer to rotate to the direction of the applied field.

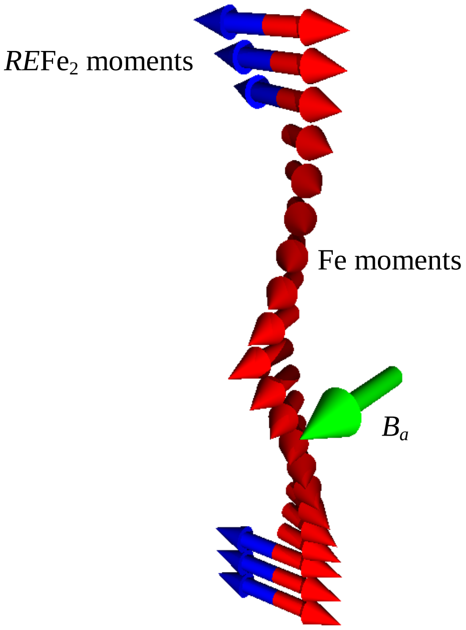

Figure 4.2: Diagram showing a multilayer exchange spring. The blue (red) arrows are the *RE* (Fe) spins respectively.

These systems have been proposed as superior data storage media since they offer additional flexibility in optimising the magnetic properties needed to increase the storage density of the hard disk drive (HDD). They have the potential to overcome the superparamagnetic limit associated with the breakdown of 'Moore's Law' [16], with respect to the aerial density of the HDD.

To overcome the superparamagnetic limit, 'bits' need to be sufficiently small to achieve the desired density required without suffering from thermally activated data loss [1]. Bilayer grains of a magnetically hard and soft layer, magnetic exchange springs set up in the soft-layer can be used to initiate rotation and hence reduce the 'write-field'.

The Laves phase materials grown by MBE (see Ch. 3) have a high epitaxial quality and are excellent model systems for the investigation of exchange spring multilayers. Here, we discuss two types of exchange spring systems (*i*) an $ErFe_2/YFe_2$ spin-flop exchange spring and (*ii*) a $DyFe_2/YFe_2$ transverse exchange spring. The $ErFe_2$ system has an out-of-plane easy axis, with the spin-flop state defined as when the Er magnetisation undergoes a high field reorientation transition from being near an out-of-plane easy $\langle 111 \rangle$ direction to an equivalent near in-plane easy $\langle 111 \rangle$ direction. The transverse exchange spring in the $DyFe_2/YFe_2$ system is an intermediate state between an antiferromagnetic state where the Dy moments aligned along the [001] and a reversed magnetic exchange spring with the Dy moments now along the $[00\bar{1}]$ hence, the transverse spring has the Dy moments out-of-plane along the [100] direction.

There are several key stages to the magnetic reversal of a magnetic exchange spring. The reversal begins at the bending field B_B, as described earlier. This is the point at which exchange springs are set up within the system, rather like artificial domain walls. As the applied field is increased beyond the bending field the Bloch domain walls start to penetrate into the hard magnetic layer until a critical applied field B_{Cr} is reached. Up until this point the process is completely reversible however beyond the critical field B_{Cr} the hard layer switches irreversibly. This process is symmetric when the applied field is reversed in direction. The typical magnetic hysteresis loop can be seen in Figure 4.3 which shows the typical exchange spring behaviour described above. Note the stack thickness and the ratio of the soft to hard layers, as this is what gives a large bending field.

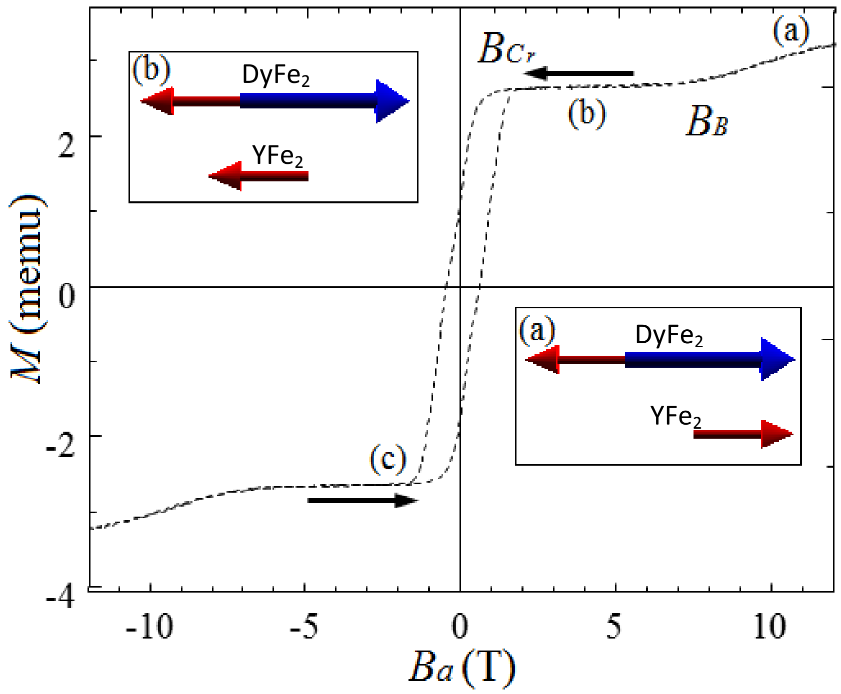

Figure 4.3: Hysteresis loop of a [DyFe$_2$ (60 Å)/YFe$_2$ (40 Å)]×40 exchange spring collected by VSM. Magnetic applied field applied along [001] and at 200 K. The arrows show the direction the loop was taken. Inserts show the DyFe$_2$ (Dy=blue, Fe=red) and YFe$_2$ spin configurations, the arrow representing the configuration in the soft YFe$_2$ layer is the average exchange spring direction in the layer [17].

Figure 4.3 shows simple exchange spring behaviour at room temperature when the field is applied along the [001] axis. The hysteresis loop was collected using a vibrating sample magnetometer (VSM) described in Ch. 3. The hysteresis loop displays the reversal of an exchange spring. At (a) the majority of the spins of the Fe (Dy) in the soft (hard) layers are parallel to the applied magnetic field respectively *i.e.* an exchange spring is set up. A proportion are still aligned antiparallel due to the exchange spring. The Fe moments in the soft YFe$_2$ layers form a tight exchange spring, as the field is reduced the Fe spins in the soft layer unwind eventually (B_a<B_B) reaching the 'net' antiferromagnetic state in zero-applied field (b) as shown in the inset of Figure 4.3. In reverse fields, the Dy moments start to rotate. Eventually in a sufficiently high reverse magnetic field the Dy moments switch (c).

In reality the rotation and switching of the magnetisation can be more complex than that described above given the presence of intermediate states and multiple axis of easy and hard magnetisation.

4.2 ErFe$_2$/YFe$_2$ spin-flop exchange spring

ErFe$_2$/YFe$_2$ is an intriguing exchange spring system. At temperatures less than 200 K, the easy axis of magnetisation lies between the [110] crystal growth axis and an out-of-plane $\langle 111 \rangle$ axis while at lower temperatures, the easy axis is out of plane, between the [111]-[110] (or $[11\bar{1}]$-[110] axis) with no *y*-component $([\bar{1}10])$. In the presence of an applied magnetic field directed along the [110] (growth) direction, a magnetic exchange spring is set-up in the YFe_2 layer. This is called a vertical exchange spring state, as all the Er spins tend to align with the film normal. This is shown schematically in Figure 4.4(a).

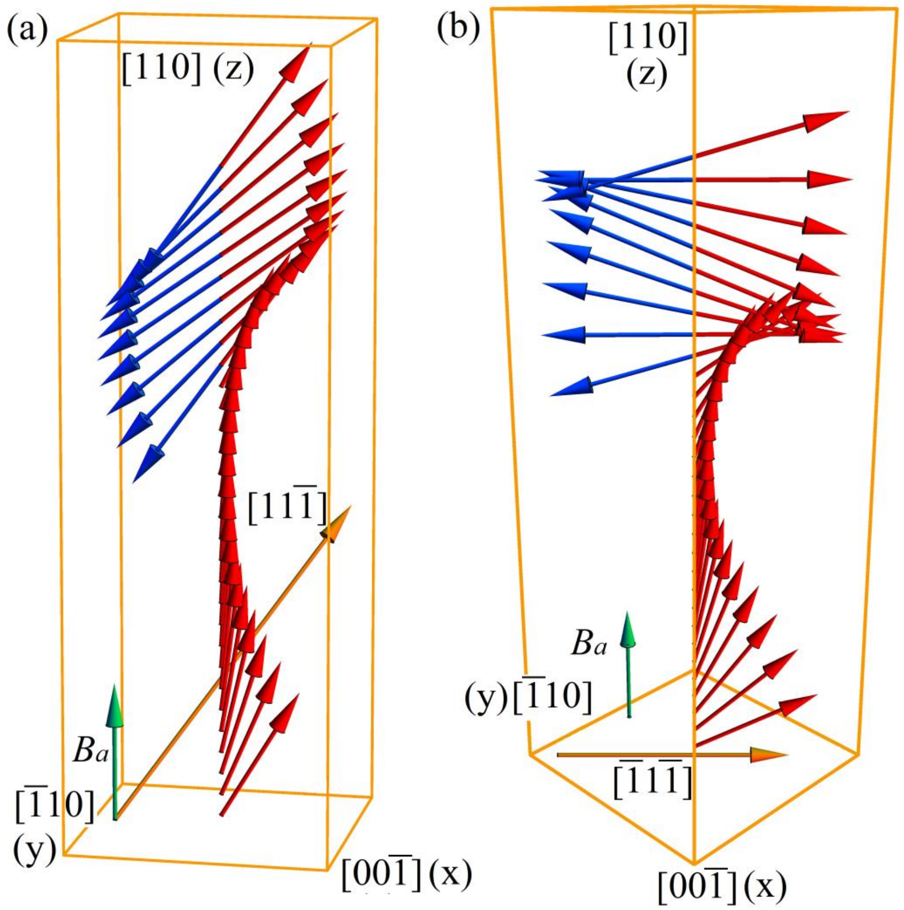

Figure 4.4: Exchange spring states in an applied field of 4 T at 220 K. Blue (red) arrows represent the Er (Fe) magnetic moments respectively. (a) Vertical exchange spring (b) Spin-flop exchange spring state. For clarity, only every other magnetic monolayer is shown. Note rotation of 3D box by 45 ° about the *z*-axis going from (a) to (b).

In the vertical exchange spring (Figure 4(a)) all the spins are confined to the $(\bar{1}10)$ plane whereas in the spin-flop exchange spring state (Figure 4(b)) the spins are confined to a $(\bar{1}12)$ plane *i.e.* the spin flop is when the Er moments fall from out-of-plane to in-plane. Following Martin *et al.* [18, 19] on magnetic superlattices of $ErFe_2/YFe_2$, bulk magnetometry and Anomalous Hall Effect at low temperatures show there is only one switch of the hard $ErFe_2$ layer from $[11\bar{1}]$ to a near $[\bar{1}\,\bar{1}\,\bar{1}]$ out-of-plane axis on reversing the magnetic moment. This is illustrated in Figure 4.5 [20]. The easy axis direction of the Er is determined by the cubic crystal field interaction at the Er^{3+} site which favours the $\langle 111 \rangle$ type-axes, however because the films are grown by MBE there are additional strain terms arising which favour the crystal growth axis [110].

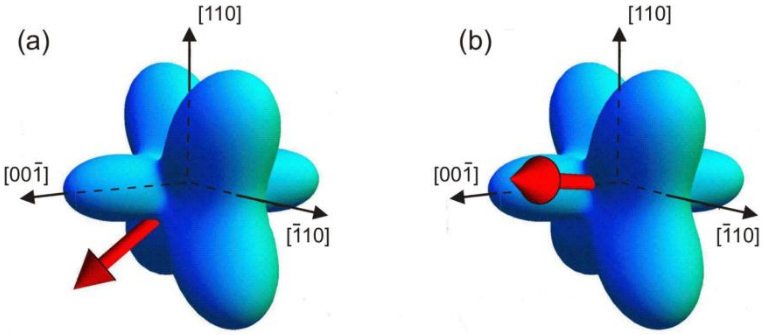

Figure 4.5: The average Er moment (red) with respect to the single-ion anisotropy energy surface (blue) for (a) the vertical exchange-spring and (b) the spin-flop state [18].

The simulated anisotropy surface (blue) is shown in Figure 4.5. The average direction of the Er moments obtained from micromagnetic simulations is shown by red arrows. It shows how easily switching can take place from an out of plane exchange spring (Figure 4.5(a)) to an in plane spin-flop state (Figure 4.5(b)). In particular it is a relatively easy matter for the Er moments to switch between the states (a) and (b) by riding up over a small energy saddle point in the anisotropy surface.

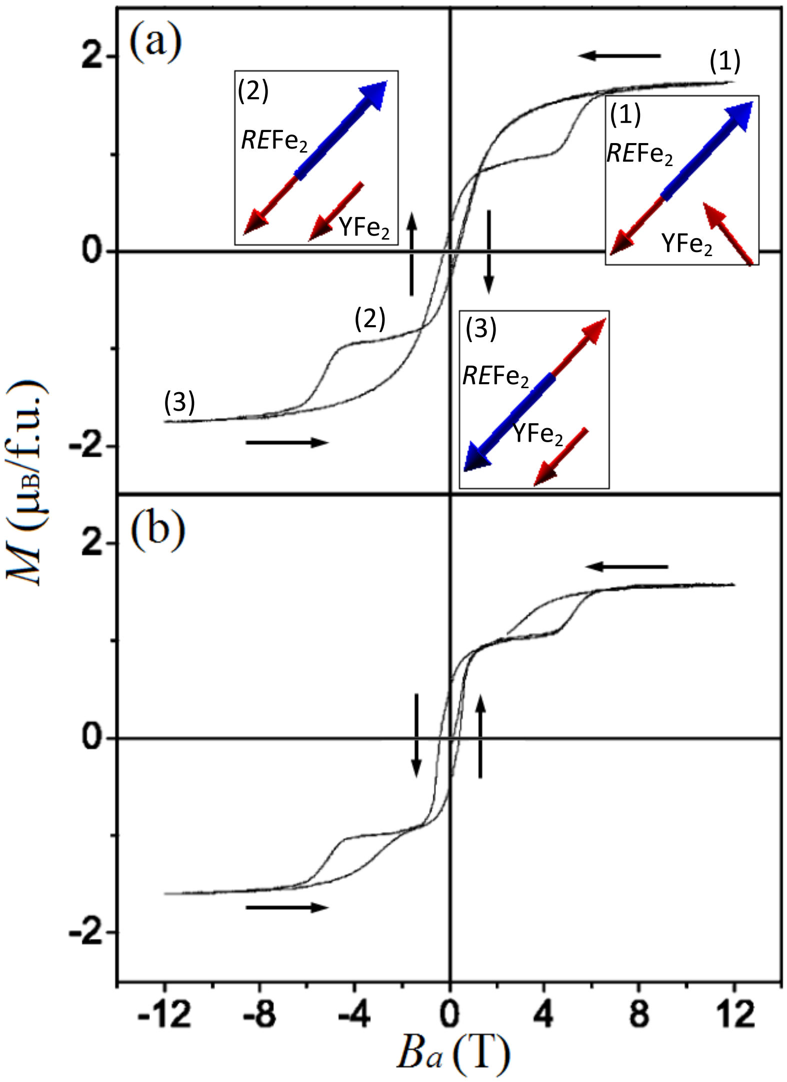

Figure 4.6: Hysteresis loops obtained for [ErFe$_2$(50 Å)/YFe$_2$(150 Å)]×20 with the applied field along the [110] at (a) 100 K with inserts representing the *RE*Fe$_2$ and YFe$_2$ spin configurations at points along the hysteresis loops and (b) 150 K. Arrows show the applied field direction [18].

Figure 4.6 shows the low temperature hysteresis loops collected using the 12 T VSM. It should be noted that for temperatures below 100 K the coercivity is negative. This occurs because the magnetisation changes sign before the applied magnetic field reaches zero.

At the lower temperatures (Figure 4.6(a)) there is only a single irreversible switch whereas at increased temperatures (Figure 4.6(b)) the sample is characterised by three irreversible steps. In Figure 4.6(b) sweeping the applied field from 12 to -12 T (Figure 4.6(a)) the first irreversible switch occurs at ~ 5 T. The second is as the applied field reverses with a positive coercivity of 0.4 T then correspondingly the third step begins at the field of -4.5 T. The difference that occurs between Figure 4.6 (a) and (b) is due to the temperature dependence of the strain term in the anisotropy and the multilayer and substrate having different thermal expansion coefficients.

At the increased temperature (Figure 4.6(b)) the additional switching at ≈ 5 T indicates a reorientation transition must occur due to it being irreversible. Computational studies that show this can be explained as the Er magnetisation flips from an $\langle 111 \rangle$ out-of-plane to a near in-plane $\langle 111 \rangle$ direction: the spin-flop state.

Computer simulations [20, 21] reveal also that the exchange-spring driven spin-flop transition at high temperatures is simply due to switching of the Er moments. However, despite switching of the Er moments, bulk magnetometry measurements only reveal a very weak magnetic signature. Changes in the $ErFe_2$ lattice are masked by concomitant changes in the YFe_2 magnetic exchange springs leading to only small changes in the total magnetic moment

4.3 Micromagnetic modelling (spin-flop exchange spring)

The magnetic exchange spring interactions can be characterised in terms of their strongest to weakest interactions. The Fe-Fe ferromagnetic exchange is the strongest (~600 K) with the antiferromagnetic Er-Fe exchange next (~100 K) the Er-Er exchange is very weak and is neglected in the model. These Fe-Fe, *RE*-Fe and *RE-RE* interactions have already been described in greater detail in Ch. 2.

The effective magnetic moments at the Er and Fe sites for T = 0 K, can be set at 9 μ_B and 1.5 μ_B respectively. This is a simplification. Band-structure calculations have shown that, in addition to the 3*d* moments on the Fe there are induced 5*d* moments which are driven primarily by the Fe 3*d* sublattice. It is a reasonable approximation to use a discrete two component ferrimagnetic model, provided we ascribe $\mu_{Er} = 9\ \mu_B$ and μ_{Fe} $(=\mu_{3d} + \mu_{5d}) = 1.5\ \mu_B$ [22].

In discrete form [23], the energy of the exchange spring takes the form:

$$E_{tot} = \sum_i \sum_j \sum_k \varepsilon_{i,j,k} \qquad (4.2)$$

Where $\varepsilon_{i,j,k}$ is the energy at site (i, j, k) given by:

$$\begin{aligned}
\varepsilon_{i,j,k} &= -\frac{1}{6}(2\mu_{FE})B_{ex}[\cos(\Omega_{i,j,k+1} - \Omega_{i,j,k}) \\
&+ \cos(\Omega_{i,j,k} - \Omega_{i,j,k-1}) + \cos(\Omega_{i,j+1,k} - \Omega_{i,j,k}) \\
&+ \cos(\Omega_{i,j,k} - \Omega_{i,j-1,k}) + \cos(\Omega_{i+1,j,k} - \Omega_{i,j,k}) \\
&+ \cos(\Omega_{i,j,k} - \Omega_{i-1,j,k})] + K_{i,j,k}(\Omega_{i,j,k}) \\
&- 2\mu_{Fe}B_A\cos(\Omega_{i,j,k} - \Omega_H) + \mu_{Er}B_A\cos(\Omega_{i,j,k} - \Omega_H)
\end{aligned}$$

(4.3)

The following assumptions have been made: (*i*) a cubic lattice has been used with nearest neighbour interactions, (*ii*) the energy at a given site is equal to that of the formula unit (1 Er (Y) atom and 2 Fe), (*iii*) generalized angles $\Omega_{i,j,k}$ are a shorthand notation for the Cartesian angles ($\theta_{i,j,k}$, $\varphi_{i,j,k}$) and (*iv*) the Fe-Fe exchange and applied fields are equal to B_{ex} and B_a respectively. Eq 4.4 shows the shorthand notation for the Cartesian angles.

$$\begin{aligned}\cos(\Omega_{i,j,k+1}-\Omega_{i,j,k}) &= \sin\theta_{i,j,k+1}\sin\theta_{i,j,k}\cos(\phi_{i,j,k+1}-\phi_{i,j,k}) \\ &\quad+\cos\theta_{i,j,k+1}\cos\theta_{i,j,k}\end{aligned} \tag{4.4}$$

The magnetic field is applied along Ω_H. The anisotropy is denoted by $K_{i,j,k}$, which is only non-zero at the Er sites. In practice, the anisotropy of the $ErFe_2/YFe_2$ multilayer film is driven by that of the Er^{3+} ions [24]. The crystal field and the magneto elastic interactions, both of which are electrostatic in nature, compete with each other. For simplicity only the first order strain term has been used, values of which can be found in Ref. 25. The values for the anisotropy parameters of the Er^{3+} ion can be found in Ref. 26. In summary, at low temperatures, the $ErFe_2/YFe_2$ system in zero applied field presents a layered antiferromagnetic state with the net moment pointing out of the plane of the film between the [110] and the $[11\bar{1}]$ axis, as shown schematically in Figure 4.5(a). The programme, developed by Prof. Bowden, determines (local) energy minima and the states associated with them and the range of stability for reversible and irreversible transitions to other states.

However to completely understand the switching in this $ErFe_2/YFe_2$ system it is necessary to perform element specific Er x-ray magnetic circular dichroism (XMCD) [20]. Previous studies of $DyFe_2/YFe_2$ [27] and $ErFe_2/YFe_2$ [18] superlattices have demonstrated the need for element specific magnetometry to unravel switching and reversal mechanisms. To this end, micromagnetic simulations for the $ErFe_2/YFe_2$ system will be presented alongside the layer-specific magnetometry measurements collected by XMCD discussed later in this Chapter.

4.4 Transverse exchange spring

In this sub-section, a $DyFe_2/YFe_2$ exchange spring system is presented which demonstrates the existence of multiple exchange spring states. The $DyFe_2/YFe_2$ multilayer film was first used to demonstrate exchange spring driven giant magneto-resistance (GMR) [17] and negative coercivity [27] (described above in section 4.2). Previous works on this system have described the reversal as a single switch from a reversed antiferromagnetic state to an in-plane magnetic exchange spring [21, 28]. This is shown in Figure 4.7 at an applied field of 5 T. However the situation is more complicated than this simple scenario. The *RE* sample again was grown by MBE (see Ch. 3) with the composition [$DyFe_2$ (60 Å)/YFe_2 (240 Å)] × 15 and was grown atop a $(11\bar{2}0)$ sapphire substrate. Magnetometry measurements were performed upon the sample and are shown below.

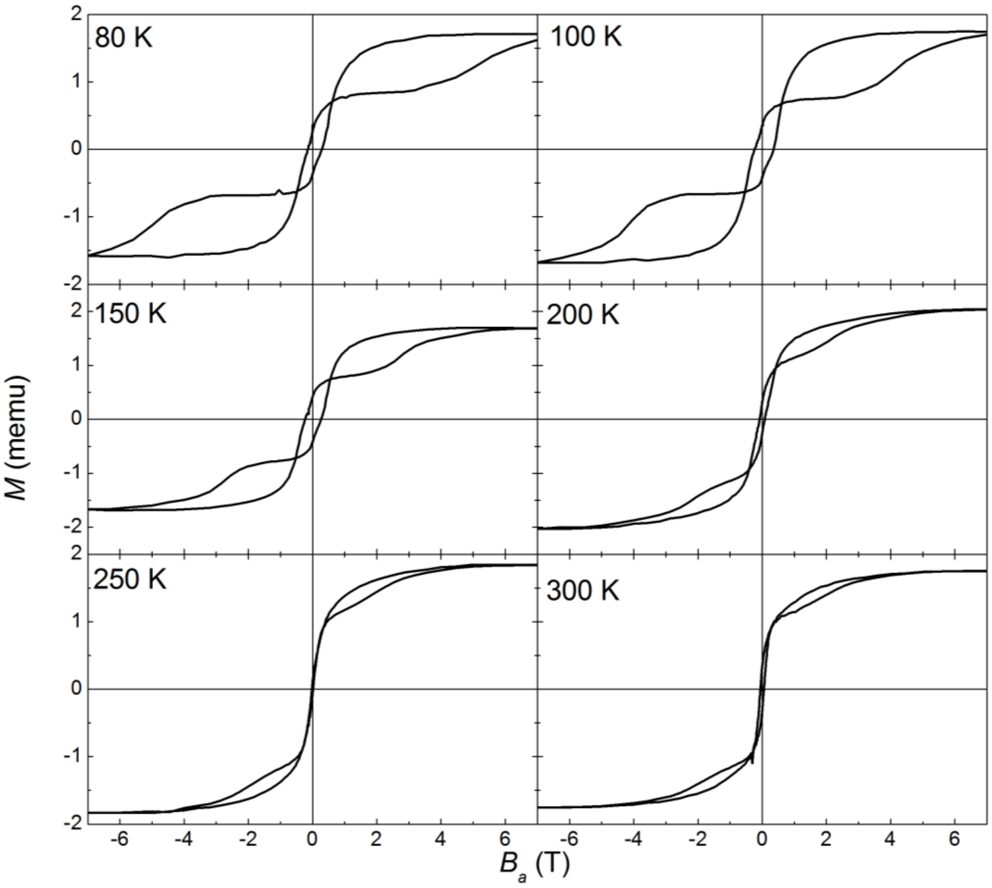

Figure 4.7: Bulk VSM magnetisation curves for a $DyFe_2/YFe_2$ multilayer at temperatures from 80-300 K. The applied field is along the [001] direction.

Figure 4.7 shows the VSM hysteresis loops (see Ch. 3 for experimental detail) for the $DyFe_2/YFe_2$ multilayer with the applied magnetic field along the in-plane [001], which is the easy axis in the temperature range 80 to 300 K. All the loops are characterised by a negative coercive field. As the field is reduced towards zero the exchange spring in the soft YFe_2 layers unwind yielding a net antiferromagnetic state with a negative coercive field [27].

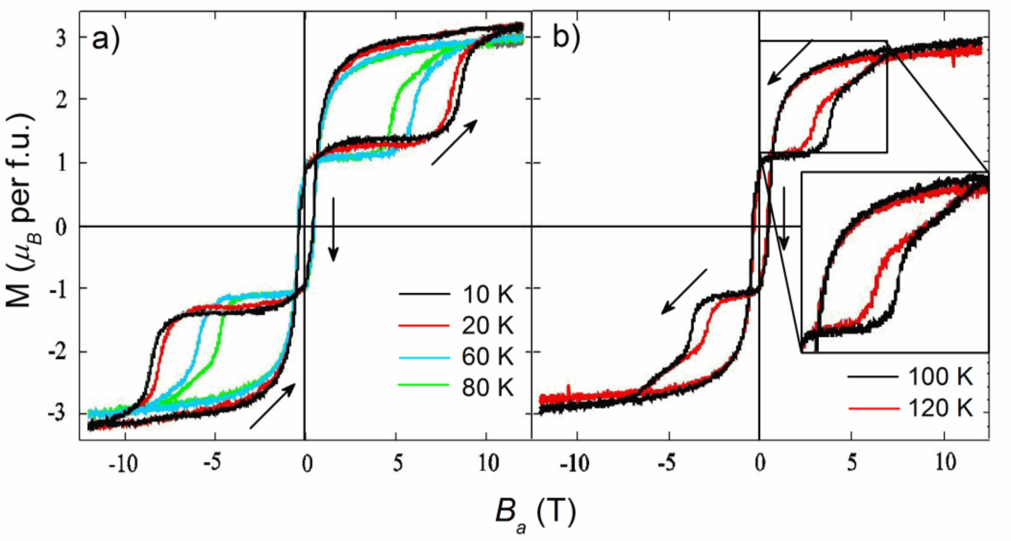

Figure 4.8: Bulk VSM magnetisation curves in a large applied field for a $DyFe_2/YFe_2$ multilayer at temperatures from 10-80 K. The applied field is along the [001] direction [14].

At very low temperatures we find a single irreversible switch is observed and displayed in Figure 4.8(a) 10 and 20 K loops. At temperatures in the range 50-80 K the irreversible switching is characterised by a two-step transition, this feature is highlighted in Figure 4.8(b) (see inset). This intermediate state is in fact a transverse out-of-plane magnetic exchange spring. More conclusive evidence of this exchange spring state will be presented in later sections which details XMCD experiments. Partial magnetic loops performed after stopping at the top of the first step in the main loop and subsequently reducing the magnetic field back to zero revealed the presence of a reversible exchange spring. For this partial loop the magnetisation vanishes when $B_a = 0$ T. As we shall see in section 4.14 this is a classic feature of a transverse exchange spring.

Figure 4.9 shows more VSM hysteresis loops for the $DyFe_2/YFe_2$ multilayer but with the applied field along the hard $[\bar{1}10]$ direction which corresponds to the low temperature hard axis.

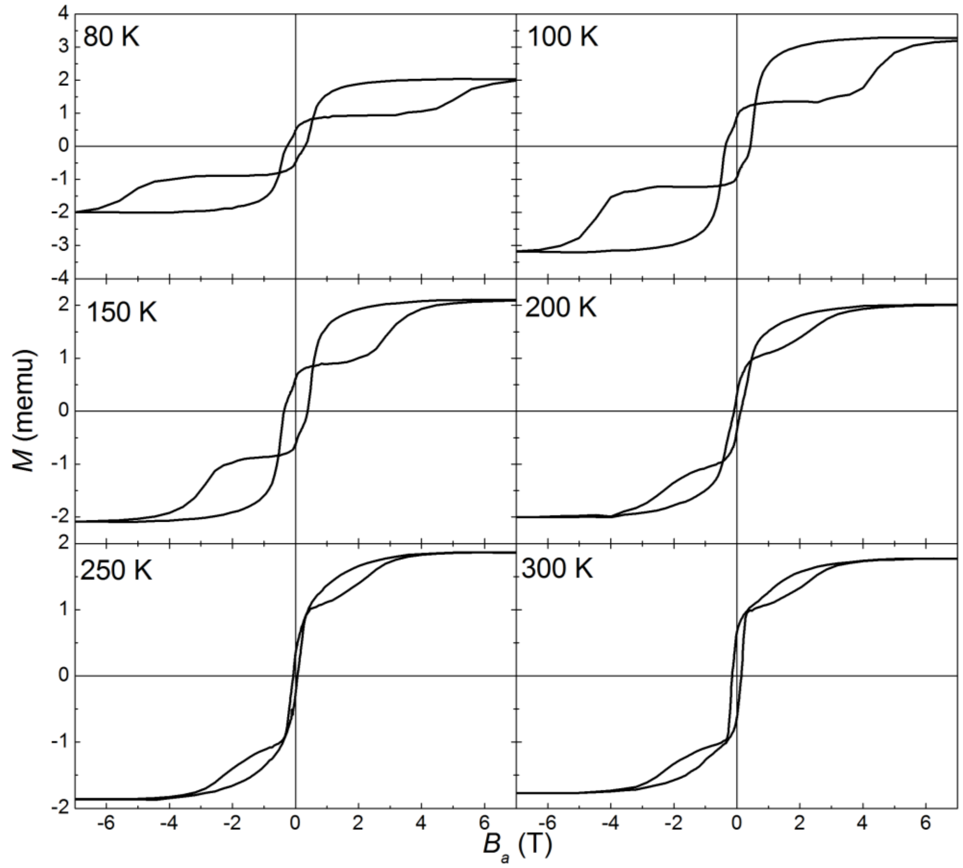

Figure 4.9: Bulk VSM magnetisation curves for a $DyFe_2/YFe_2$ multilayer at temperatures from 80-300 K. The applied field is along the $[\bar{1}10]$ direction.

The differences between the easy and hard axis magnetisation loops of Figure 4.7 and Figure 4.9, respectively, are subtle, but are most pronounced when comparing the coercivity in zero applied field. The second difference is in the shape of the second switching at high applied fields, the shape of this high field switching changes with temperature.

4.5 Micromagnetic modelling (transverse exchange spring)

Micromagnetic modelling by Prof. Bowden [28-29] has been used to identify the magnetic states in the $DyFe_2/YFe_2$ multilayer, as per Ref. [20], but this time using the Dy moments ($\mu_{Dy} = 10\ \mu_B$ and $\mu_{Fe} = 1.5\ \mu_B$) and anisotropy parameters.

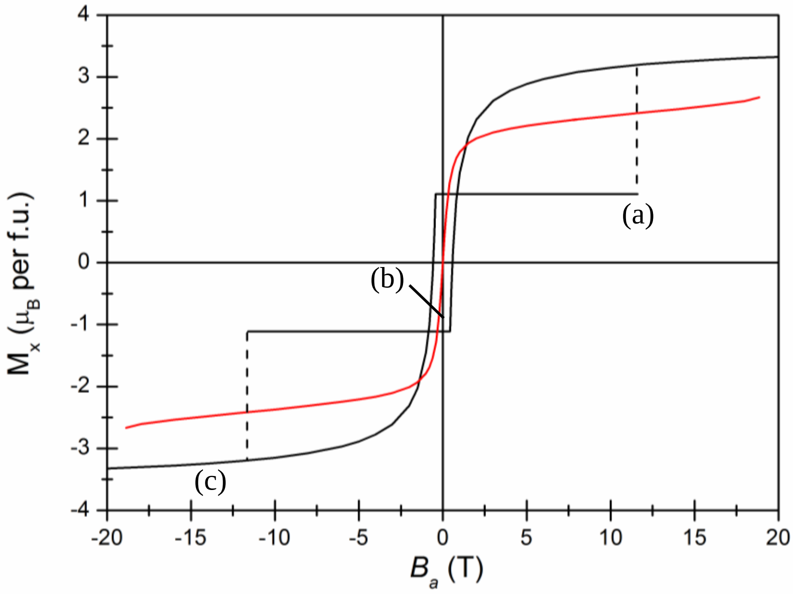

Figure 4.10: Calculated magnetisation curves at 100 K. The black curve represents the in-plane magnetic exchange spring with an irreversible switch. The red curve is the transverse exchange spring, where the Dy moments point out of the plane along a [100] axis. The calculated Stoner-Wohlfarth limit for the transverse spring is 19.3 T. The points labelled as (a), (b) and (c) correspond to Figure 4.11 where the spin configurations are presented.

Figure 4.10 shows the calculated curve for the full magnetisation loop at 100 K. The hysteresis loop has very similar features to the experimental loop collected by VSM and displayed in Figure 4.7 (100 K loop). The spin configurations for the magnetisation loop are denoted by (a), (b) and (c) which are presented in Figure 4.11. The single irreversible switch observed at ≈11.6 T, from the reversed antiferromagnetic state to an in-plane magnetic exchange spring, where the Dy moments now point along the applied field direction. The field is an estimate obtained by (*i*) determining the Stoner-Wohlfarth (SW) field [30] and (*ii*) finding that field where energy crossover occurs between the in-plane exchange spring and the reversed antiferromagnetic state B_{CO}, and (*iii*) taking the geometric mean of these two fields B_C. The only basis for this procedure is that $B_{CO} \leq B_C \leq B_{SW}$. $B_{SW} = 57.85$ T, $B_{CO} = 2.33$, $B_C = \sqrt{B_{CO} B_{SW}}$ = 11.6 T. This is still only an estimate but, in exchange spring systems, gives a more accurate value of the switching field than the Stoner Wohlfarth approximation. Figure 4.10 also shows the magnetisation curve for the transverse exchange spring (red curve). This is when the Dy moments point along a [100] out of plane easy-axis direction, perpendicular to the applied field. Evidently the Fe moments in the YFe_2 layer are still able to rotate, tending towards the magnetic field.

The magnitude of the overall magnetic moment in the transverse spring state is in agreement with the magnetic moments measured by VSM at the first step in the two-step transition. Thus micromagnetic modelling confirms that the reversal mechanism takes place in two steps as shown schematically in Figure 4.11.

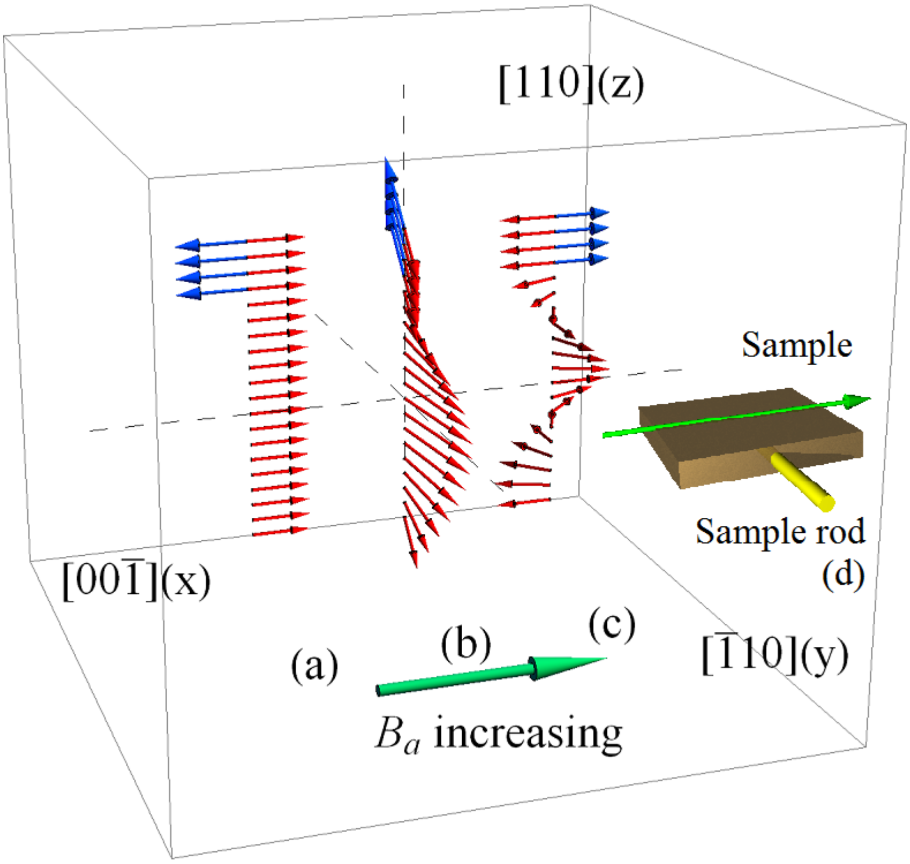

Figure 4.11: Schematic of the magnetic reversal showing the two-step process. (a) Reversed antiferromagnetic state, (b) transverse out of plane exchange spring state, and (c) in plane exchange spring. Dy (Fe) moments are blue (red) respectively, (d) Sample mounted ready for XMCD measurements. A complete wall is formed.

To investigate further the origin of the two-step transition observed in the $DyFe_2/YFe_2$ at low temperatures, as per Figure 4.8(b), we investigated both Dy-XMCD and Fe-XMCD, this is investigated in the following sections.

The powerful technique of XMCD is used to provide insight into both the magnetisation states and reversal mechanisms in $RE$$Fe_2/YFe_2$ exchange spring systems. Taken together with computational modelling gives a detailed picture of the new exchange spring states discovered and their magnetic behaviour.

4.6 Static x-ray measurements

X-ray studies of magnetic exchange springs using synchrotron facilities such as, the Diamond Light Source Ltd and BESSY II, allow unique information to be obtained via element specific magnetometry [31, 32]. Particularly, magnetisation switching and reversal mechanisms of a magnetic multilayer can be easily determined [19, 33-34]. Here, we discuss just two situations that lend themselves to this technique. First the $ErFe_2$/YFe_2 system where the root-cause of the spin-flop transition is unclear [17] (see Figures. 4.4-4.6). Secondly, the $DyFe_2$/YFe_2 system where more than one hysteretic switch is observed in the reversal mechanism (see Figure 4.8) [14].

Magnetisation experiments using x-ray magnetic circular dichroism (XMCD) to provide magnetic contrast is a powerful new tool. XMCD allows for element-specific, and hence layer-specific magnetisation loops to be collected [35]. The information gained leads to a more complete understanding of switching mechanisms and magnetic reversal. Synchrotron experiments and related procedures have led to a new branch of physics in its own right. Here we detail only that information relevant to the collection of element-specific magnetisation loops.

4.7 Synchrotron facilities

The synchrotron facility known as the Diamond Light Source Ltd is a large international facility with access time allocated to numerous research proposals submitted [see appendix]. The facility is based on a storage ring with an electron-beam current of ~300 mA. The electrons are guided by 48 large 'bending magnets' used to curve the electron beam between adjacent straight sections. To minimise collisions with background gas atoms the electron-beam circulates in an ultra-high vacuum. The x-rays are collected from the storage ring by two methods (*i*) bending magnets and (*ii*) insertion devices [36]. As the electron beam passes through a bending magnet it emits a stable beam of x-rays over a wide spectrum. On the other hand, insertion devices are located on straight sections of the storage ring. These are much more efficient at producing very narrow bright monochromatic synchrotron light. The insertion device consists of an array of magnets which force the electron to oscillate in the horizontal plane as shown schematically in Figure 4.12.

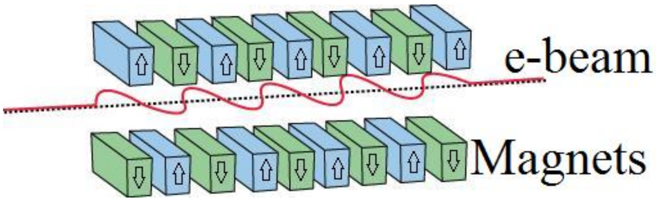

Figure 4.12: Schematic showing the working of an undulator like that fitted on I06 beamline at the Diamond Light Source Ltd.

By varying the separation of the magnet arrays it is possible to tune the energy of the x-rays generated. The resultant beam is then focused using mono-chromators, mirrors and slits down a given beamline to the end station; where the actual experiments are performed. The end stations used in this work were beamline I06 and I10, equipped with superconducting magnets of 6 T [20] and 14 T [33] respectively.

4.8 XMCD

X-ray magnetic circular dichroism (XMCD) is a powerful technique which uses resonant x-ray absorption involving for example, 3*d* (Fe) core electrons to provide magnetic contrast. Therefore for magnetic multilayers with differing elements in alternate layers the magnetisation and reversal mechanisms of alternate layers can be studied separately. The technique is sensitive, to avoid saturation the thickness of the sample is typically ~nms of a particular layer/element. It can also be used to detect magnetic moments as small as 0.001 μ_B per atom [36]. XMCD can also be used to provide information not only on the total magnetisation but also on the spin and orbital components taken separately [36]. In principle, XMCD is resonant x-ray absorption spectroscopy (XAS) performed on a magnetic sample using both left and right circularly polarized x-rays, in an applied magnetic field (H_a). The cross sections for resonant absorption are large in the soft x-ray range (500-2000 eV) [37].

A circularly polarised electromagnetic (EM) wave, or photon in the quantum mechanical regime possesses definite eigenstates of the angular momentum operator J_z, where z is perpendicular to the x-ray propagation direction. The eigenstates for right (left) circularly polarised light are $+\hbar$ ($-\hbar$) respectively [36]. If a circularly polarised photon is absorbed, conservation of angular momentum for electronic transitions must apply. The dipole transition selection rule $(\Delta\ell = \pm 1)$ is the main mechanism driving electronic transitions followed by the angular momentum conservation rule $\Delta m = +1(-1)$ for right (left) circularly polarised light respectively, this is what gives XMCD its magnetic sensitivity. The resonant absorption transitions for the *RE* elements make use of the $M_{4,5}$ transition, whereby a 3*d* electron is excited to a 4*f* state by the absorption of an x-ray of 1405, 1440 eV (1333, 1292 eV) for Er (Dy), respectively [38]. For Fe the transition is from a 2*p* to a 3*d* unoccupied state (710, 722 eV) [38]. This transition is possible due to the energy deficit between the 2*p* core to 3*d* unoccupied shell amounts to: *e.g.* 710 eV for Fe. However, Fe presents a problem in the multilayers considered here since Fe is present in all of the layers. Thus Fe- XMCD experiments yield only average values regardless of whether the Fe is associated with either the $DyFe_2$, $ErFe_2$ or YFe_2 layers. As a result Fe-XMCD experiments are therefore much harder to interpret (see section 4.13).

Y-XMCD experiments were not performed for two reasons (*i*) Y is outside the available range of the two beamlines available at the Diamond Light Source Ltd, and (*ii*) both samples contain a nonmagnetic Y capping layer protecting the multilayer from oxidation (see Ch. 3). X-rays absorbed in the Y capping layer will yield no magnetic response. Consequently for the two exchange spring systems mentioned earlier Er-XMCD and Dy-XMCD measurements were performed at the Diamond Light Source Ltd on beamlines I06 and I10, respectively.

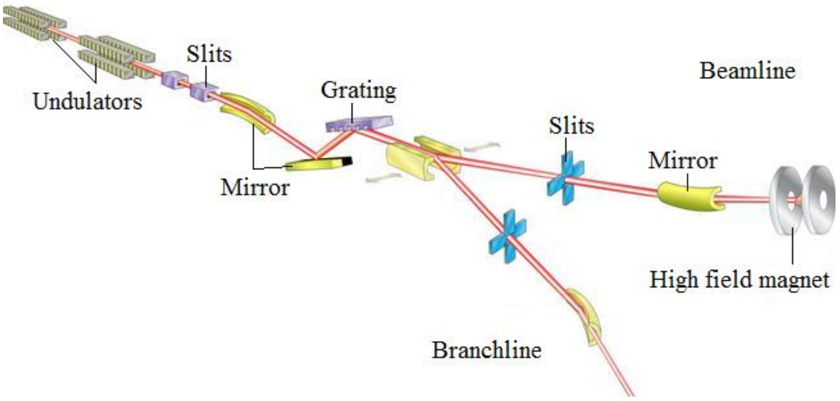

Figure 4.13: Schematic of the I10 beamline at Diamond showing the path of the x-rays from the undulator to the sample in the high field magnet [39].

Once the x-rays have been absorbed by the atom in question detection of the XAS (XMCD) can be made via two methods. As the x-ray has promoted a core electron to an unoccupied state, one of two things can occur: (*i*) Fluorescence detection via the emission of secondary x-rays from the sample as the promoted electron drops back to the core shell or (*ii*) total electron yield (TEY) where the electron is re-emitted from the sample and are detected by connecting the sample to ground through an ammeter. Generally, TEY measurements cannot probe as deeply as fluorescence [40], this is due to the escape depths of the secondary electrons generated by inelastic scattering.

4.9 XMCD experimental method 1-$ErFe_2/YFe_2$ spin-flop exchange spring

Measurements on the $ErFe_2/YFe_2$ spin-flop system were performed using the I06 beamline at Diamond Light Source Ltd. The end station is equipped with a superconducting magnet of up to 6 T and an UHV sample space of 10^{-10} mbar. The superconducting magnet can be used as either a 1 T vector magnet or 6 T along the x-ray beam direction. For the $ErFe_2/YFe_2$ spin-flop system field sweeps were conducted between ±6 T, in the temperature range 50-250 K. The sample was placed in the system via a loadlock to maintain low pressure of the beamline. It was aligned with the [110] growth direction along the applied field and x-ray beam. This arrangement allows for detection between the out-of-plane exchange spring and in-plane spin-flop state as a component of the magnetisation can only be detected along the beamline [36]. The orientations of the applied magnetic field x-ray and sample alignment are all highlighted in Figure 4.14.

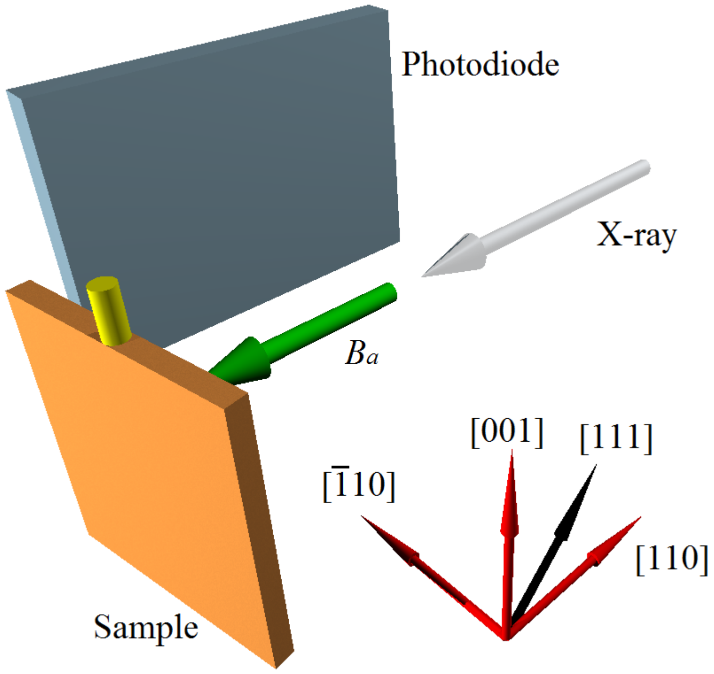

Figure 4.14: The alignment of the $ErFe_2/YFe_2$ sample with respect to the easy axis of magnetisation (black arrow) as well as the applied field. Sample is rotated 10° towards the photodiode around the [001] axis.

Er XAS was performed using the energy range 1380-1480 eV to ensure observation of the Er $M_{4,5}$ ($3d \rightarrow 4f$ at 1405, 1440 eV) edges. Experiments were also performed using the Fe $L_{2,3}$ in the energy range 680-740 eV ($2p \rightarrow 3d$ at 710, 722 eV). An example of the XAS and XMCD for Er can be seen in Figure 4.15.

In initial experiments the film normal [110] was aligned at 10° away from the x-ray beam direction, to allow for collection of both x-ray fluorescence and TEY.

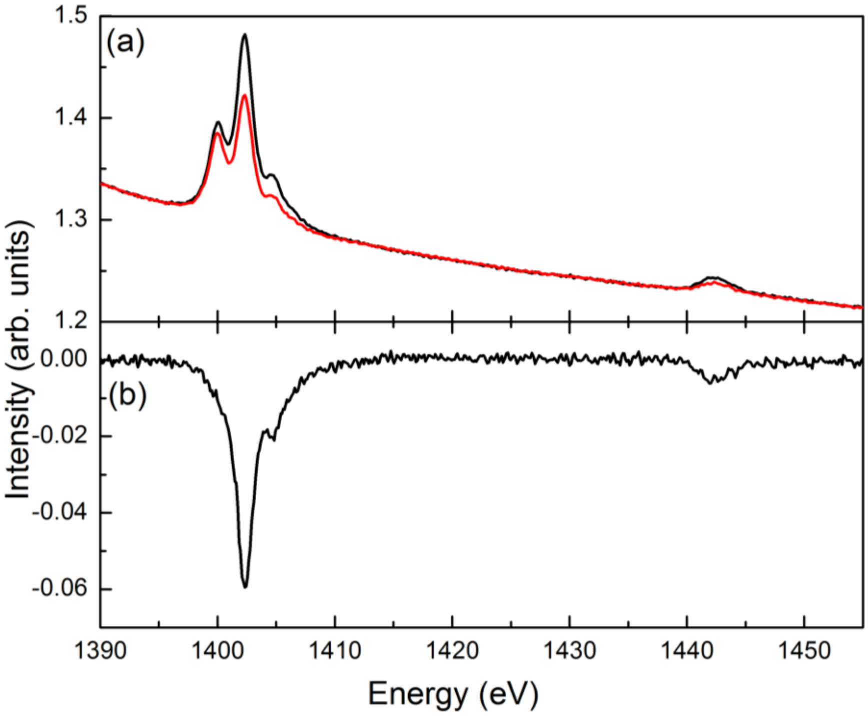

Figure 4.15: Er $M_{4,5}$ XAS in the energy range 1380-1480 eV for (a) clockwise (upper/black) and counter clockwise (lower/red) circularly polarised light. (b) The XMCD curve.

Results shown in Figure 4.15 were obtained using TEY. These results were almost identical to those obtained using fluorescence. TEY has the advantage that the sample does not need to be aligned slightly towards the photo-detector (whose plane normal was at 90° to the x-ray beam). This allows the sample to be aligned with the film normal almost parallel to the beam, as shown in Figure 4.14. This arrangement is more suited to studies of the spin-flop exchange springs as this allows for XMCD to detect when a component of the magnetisation lies in or out-of-plane of the film. As XMCD can only detect a component of magnetisation along the beam direction.

4.10 XMCD results 1-$ErFe_2$/YFe_2 spin-flop exchange spring

Er-XMCD magnetisation loops in the temperature range 50-250 K can be seen in Figure 4.16 and 4.17. It will be observed from an examination of Figure 4.16 that the loops at temperatures 50, 100, 150 and 200 K, are all characterised by a single magnetic switch. This is in agreement with the bulk magnetometry shown in Figure 4.6 (The gradual change of M_{Er} near $B_a = 0$ T may be due to a small rotation of the magnetisation from the easy axis to the film normal.) As the temperature is raised a crossover occurs at $T \approx 220$ K between the single-switching behaviour as seen in Figure 4.16 to the double switching behaviour as shown in Figure 4.17(c).

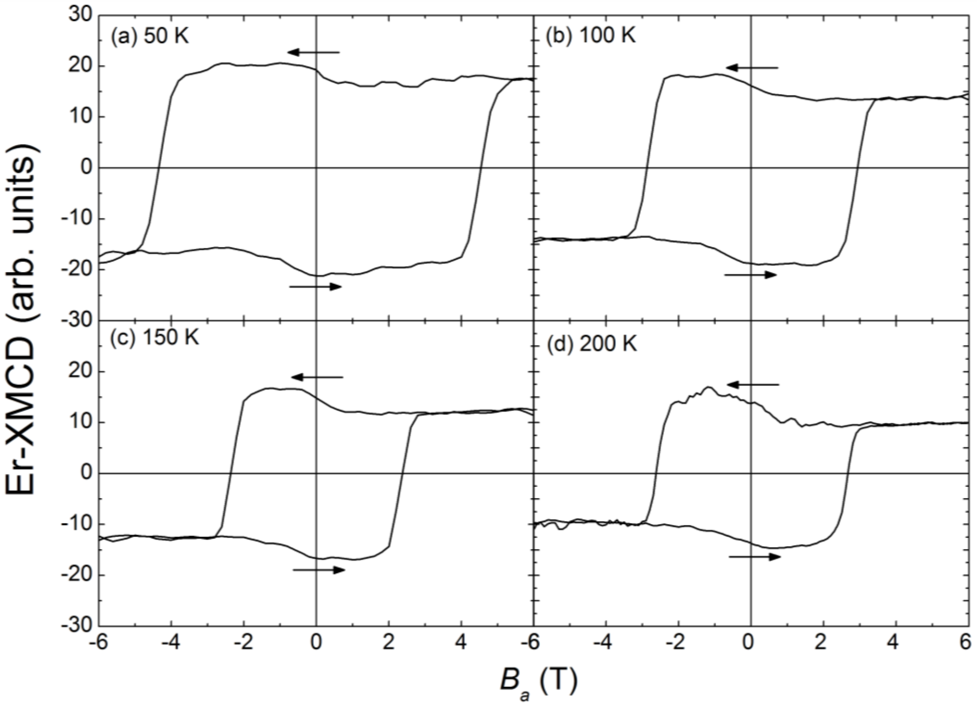

Figure 4.16: M_{Er} hysteresis loops obtained by XMCD using TEY. (a) 50 K, (b) 100 K, (c) 150 K and (d) 200 K.

On increasing the temperature the switching processes become better defined with the M_{Er} hysteresis loops now revealing two very different irreversible switching events at 250 K (Figure 4.17(d)).

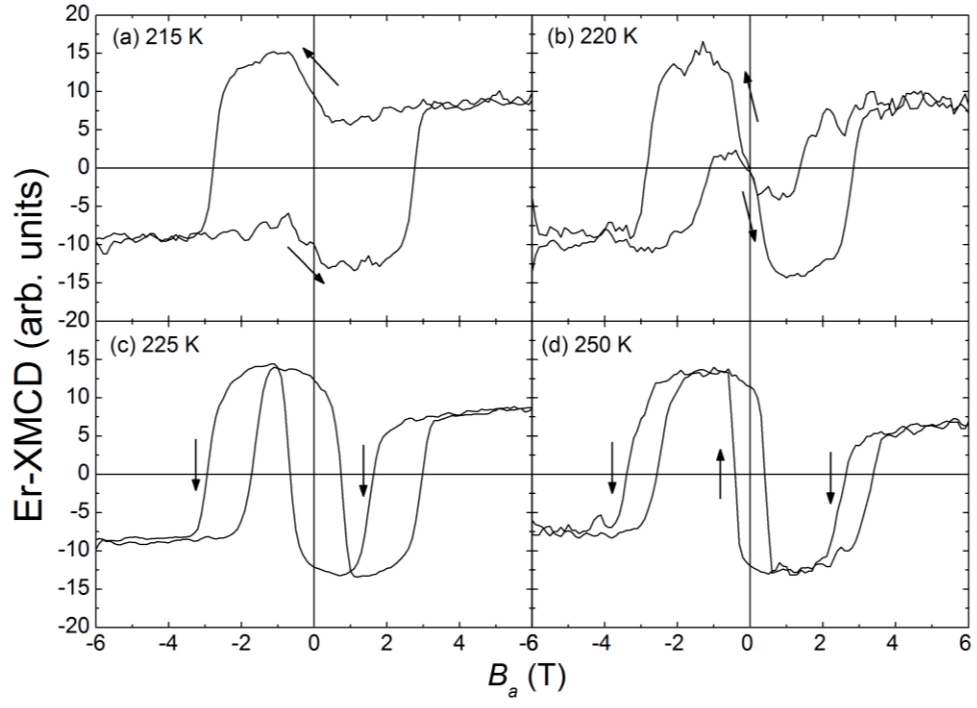

Figure 4.17: M_{Er} hysteresis loops obtained by XMCD using TEY. (a) 215 K, (b) 220 K, (c) 225 K and (d) 250 K.

The low field transition switch in Figure 4.17(d) occurs at 0.4 T with the high field transition at 3 T. Rather surprisingly, the latter increases with increasing temperature.

An explanation of the two-step switching behaviour shown in Figure 4.16 and 4.17 has been provided using the discrete micromagnetic model described earlier. The calculated results are summarised in Figure 4.18 and 4.19.

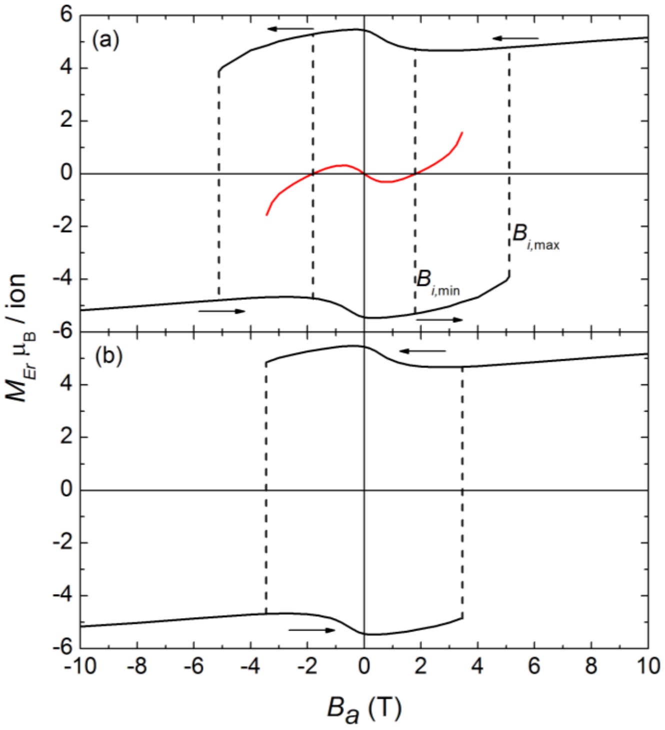

Figure 4.18: (a) Simulated M_{Er}-B_a hysteresis loop at 150 K. Solid (black) lines represent the vertical exchange spring state. The vertical outer dashed lines at 5.12 T correspond to $B_{i,\mathrm{max}}$. The inner dashed lines at 2.04 T are where the energy of the two spring states is identical $B_{i,\mathrm{min}}$. The red curve at $B_a = 0$ T, $M_{\mathrm{Er}} = 0$ gives the M_{Er} stable spin-flop state. (b) Expected M_{Er}-B_a hysteresis loop at 150 K.

Figure 4.18(a) above shows two stable spin configurations, the vertical exchange spring (black) and the spin-flop (red) state. It clearly shows that when starting from saturation the spin-flop state is never reached, so any switching between the vertical exchange spring and the spin-flop state is negated. As a result the magnetic loop is characterised by a simple one-step magnetic reversal. In reaching this conclusion we have made use of the following arguments. First the range of stability for a particular state is determined, outside this field range the magnetic system must perforce switch to another spin state. For example, in Figure 4.18(a) the outer dotted lines show the limit of the vertical exchange spring stability) *i.e.*, $B_{i,\mathrm{max}} \pm 5.12$ T, this is the Stoner-Wohlfarth transition. We have modified this model and extended it to exchange spring systems. In the Stoner-Wohlfarth model only a single ferromagnetic slab subject to a reversed magnetic field is considered. Stability is ensured via ${}^{\partial E}/_{\partial \theta} = 0$ and ${}^{\partial^2 E}/_{\partial \theta^2} > 0$. A similar, but more complex situation occurs in exchange springs.

Here stability is ensured by (*i*),

$$\partial E \big/ \partial \theta_i = 0 \qquad (4.5)$$

for all i=1, N and (*ii*) the generalisation of,

$$\partial^2 E \big/ \partial \theta_i \partial \varphi_j = 0 \qquad (4.6)$$

for all θ_i, φ_j ect. The latter leads to a N×N matrix where eigenvalues must always be definite positive values for stability. This is the exchange spring equivalent of the Stoner-Wohlfarth model [30]. For the second lower limit, this is obtained by assuming that the system switches when the energies of the vertical exchange state and its reverse state are identical (the inner dotted lines, $B_{i,\mathrm{min}} = \pm 2.04$ T in Figure 4.18(a)). As noted earlier, the actual switching must take place between these two upper and lower values. An average is taken ($B_C = 3.58$ T) [20] which is found to be a good approximation based on earlier magnetometry studies of spring systems. The average switching is displayed in the expected hysteresis loop of Figure 4.18(b). For the remainder of this thesis only the averaged values of the two calculated switching fields will be used. There is very good agreement with the XMCD results of Figure 4.16(c) and the calculated loop of Figure 4.18(b). Nevertheless, Figure 4.18(a) shows that *in principle* both exchange spring states can exist at 150 K within the field range ±4 T.

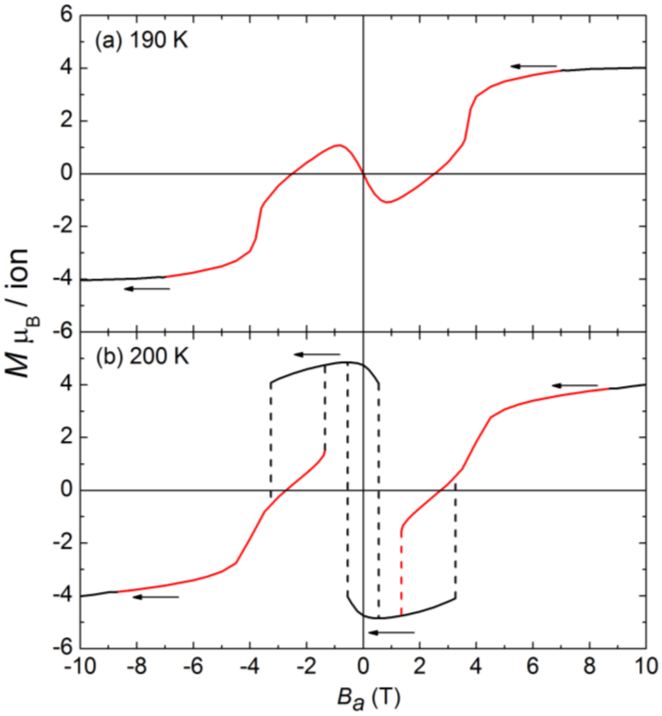

Figure 4.19: Simulated Er magnetisation curves for (a) 190 K, and (b) 200 K.

On increasing the temperature from 150 K to 220 K (190 K from simulation) the shape of the M_{Er}-B_a loop changes greatly. In Figure 4.17(b), (c) the reversal mechanism involves two clear switching fields again in agreement with the simulations shown in Figure 4.19. The differences in temperature between the XMCD data and simulations may be attributed to (*i*) inaccuracies in the Er^{3+} anisotropy values used [23], (*ii*) neglect of the small anisotropy associated with the YFe_2 layers or (*iii*) neglect of the dipole-dipole interactions in micromagnetic simulations which employ cyclic boundary conditions. As a test of the latter calculations have been performed with approximately 20 bilayer repeats, with no cyclic boundary conditions. Calculations also allow Er magnetisation loops to be obtained from just the top $ErFe_2$ layer, as well as the bulk. It was found that the two Er magnetisation curves calculated in this way differed by only a few percent.

4.11 Instabilities in $ErFe_2/YFe_2$

Following Ref. [28] it is possible to determine not only the nature of the spin configurations but also their stability by examining the eigenvalues of the double differential energy matrix E''_{Total}. Examining the differentials of the energy matrix yields firstly the maximum and minimum in the energy surface ($E'_{Total} = 0$) and if the spin configuration is stable at these positions ($E''_{Total} > 0$). Figure 4.20 shows the average inclination angle $\langle\theta\rangle_{Er}$ for Er moments above and below the spin-flop transition in the 190-220 K range. It is seen in Figure 4.20 at 190 K the spin-flop state is stable for all applied fields (solid red curve) whereas at a raised temperature of 220 K (blue line) the spin-flop state is unstable in the applied field range of 0.19-2.17 T. In this region the spin-flop state cannot exist and so therefore relaxes into a vertical exchange spring where the Er moment are now out of plane.

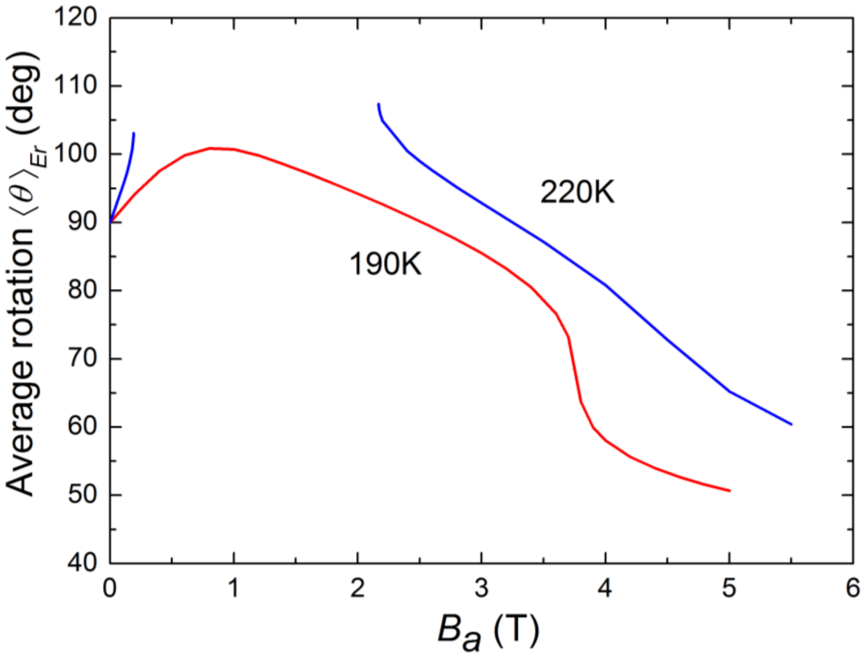

Figure 4.20: Average $\langle\theta\rangle_{Er}$ for stable spin-flop state at 190 K (red) and 220 K (blue) from computational modelling.

To examine these instabilities still further the spin-flop instability at 200 K was examined in more detail. In Figure 4.21 the average calculated angles $\langle\theta\rangle_{Er}$ for the inclination angle and

$\langle \phi \rangle_{Er}$ for the in-plane angle of the Er moments respectively can be seen. Starting from a high applied field only the vertical exchange spring is stable. At a field of 10 T $\langle \theta \rangle_{Er}$ and $\langle \phi \rangle_{Er}$ correspond to 40° and 0° respectively. However as the field is reduced below 8.7 T the vertical exchange spring state morphs into the spin-flop state (red-curve) at a continuous transition (a). As the field is reduced still further, $\langle \phi \rangle_{Er}$ rotates away from the *z*-*x* plane reaching a peak of ≈ 45° (b) until at 1.3 T where it undergoes a first order discontinuous transition collapsing into the vertical exchange spring (c). In practice this can take place with relatively little anisotropy energy change because of the presence of a small energy saddle point between the in and out of plane $\langle 111 \rangle$ axes (see Figure 4.5). This behaviour is mirrored in the XMCD data of Figure 4.17.

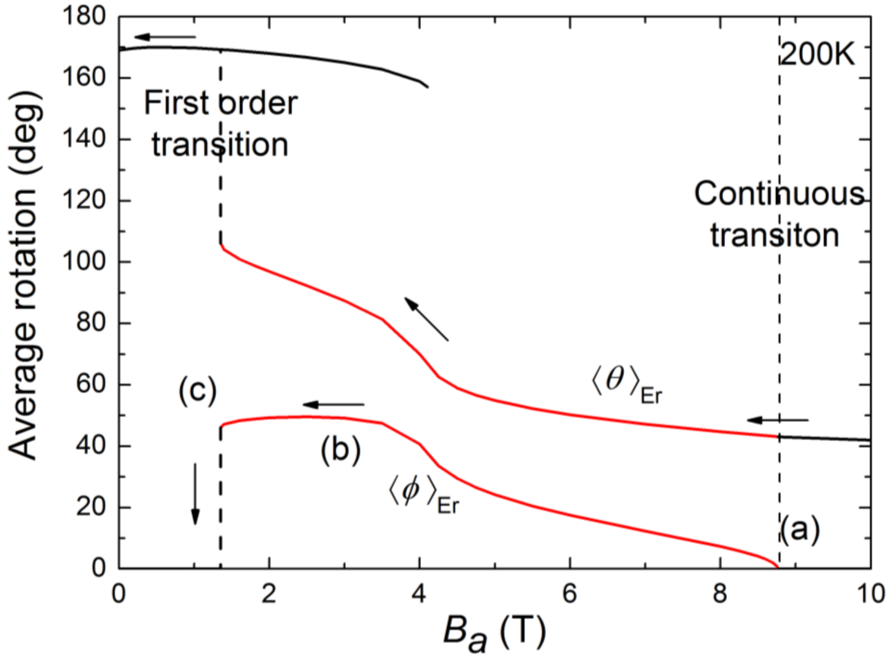

Figure 4.21: Average $\langle \theta \rangle_{Er}$ and $\langle \phi \rangle_{Er}$ for 200 K.

4.12 Transverse exchange springs in a $DyFe_2/YFe_2$ superlattice

Measurements on a new transverse spring system in a $[DyFe_2(60Å)/YFe_2(240Å)]_{15}$ multilayer were performed using the new I10 beamline at Diamond Light Source Ltd. The end station was equipped with a 14 T superconducting magnet. The magnet is a new 14 T system with the field usually applied along the x-ray beam direction. Field sweeps were conducted in the range between ±14 T and in the temperature range 4-300 K.

The film [110] growth-axis was aligned along the applied field B_a and the x-ray beam direction. The experimental arrangement possesses two fluorescence detectors, one perpendicular and the other parallel to the incident x-ray beam as shown in Figure 4.22, TEY was not available for the duration of this experiment and so all following results were obtained in fluorescence yield.

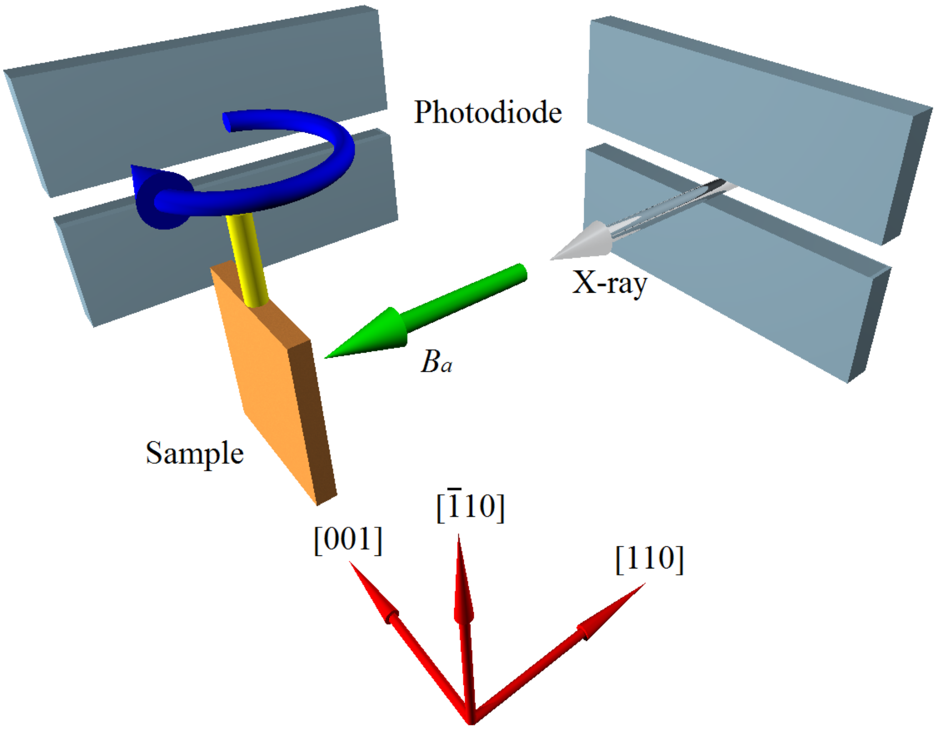

Figure 4.22: Experimental arrangement and sample orientation on the I10 beamline end station, for the $DyFe_2/YFe_2$ experiments.

Loading of the sample into the beamline and XMCD measurements were performed in the same way as for the $ErFe_2/YFe_2$ system described in Section 4.9. The Dy XAS and XMCD results can be seen in Figure 4.23

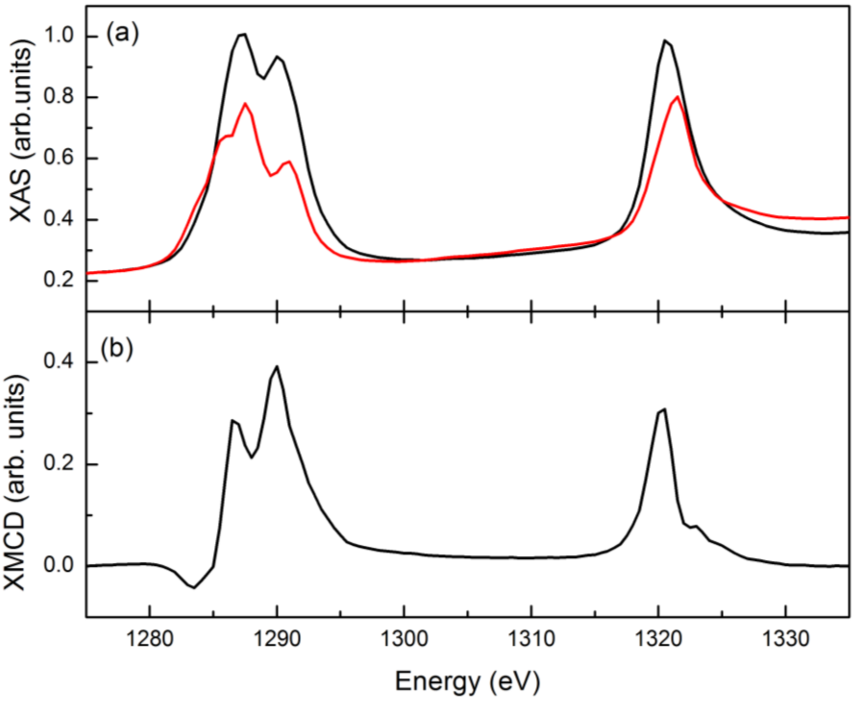

Figure 4.23: Dy $M_{4,5}$ (a) XAS, (b) XMCD collected by fluorescence detection.

The Dy-XMCD curve can be seen in Figure 4.23. It shows the Dy $M_{4,5}$ ($3d \rightarrow 4f$) absorption edges at (1327, 1293 eV). Fe-XMCD was also collected at the absorption edges stated in Section 4.9.

Before hysteresis loops can be taken a history dependent procedure must be followed to set-up a transverse exchange spring state. The sample is first mounted in the magnet system as per Figure 4.24(a). At this stage the [110] growth direction is collinear with both the applied field and the x-ray beam, which is the final arrangement of the sample. At this point in time the magnetic state of the multilayer is uncertain.

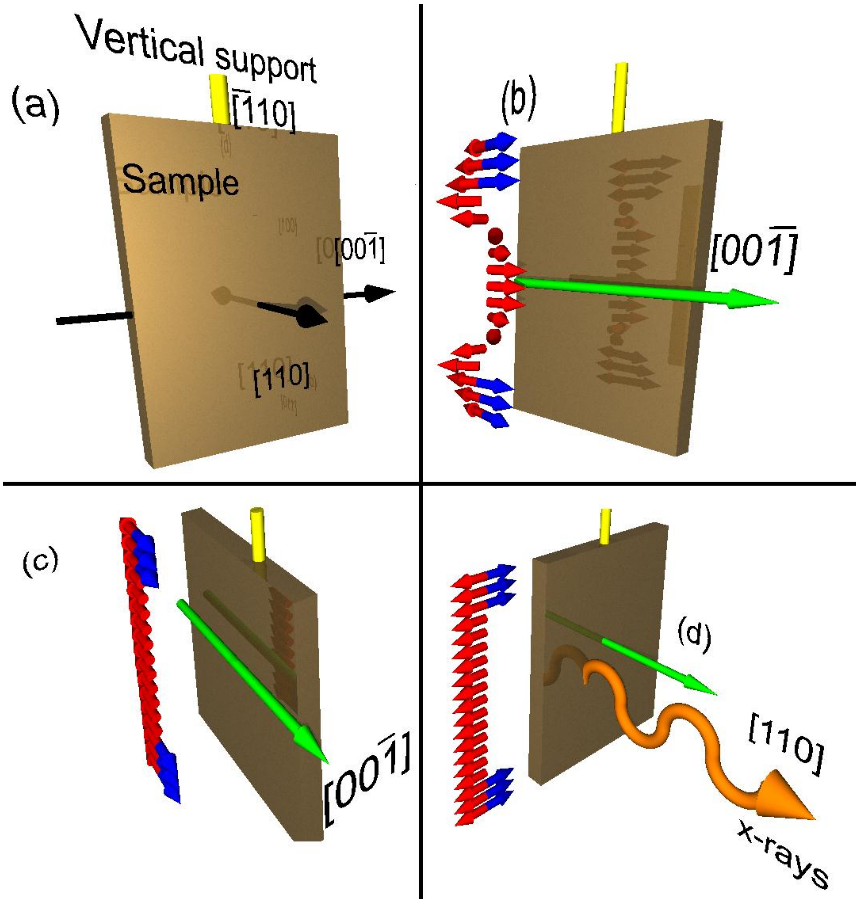

Figure 4.24: The consecutive steps required to prepare a transverse exchange spring state. The insets show the spin configurations at the different stages. The Dy (Fe) moments are blue (red) respectively. (b) B_a = 14 T, (c) B_a = 0 T, and (d) B_a = 0 T.

To define the magnetic state of the sample it was rotated 90° anticlockwise about the vertical support such that the $[00\bar{1}]$ –axis is pointing along the field direction as shown in Figure 4.24(b). The sample is then magnetised backward and forward taking the sample through a conventional in-plane magnetic loop. The applied field is then reduced to zero leaving the sample in a net antiferromagnetic state with the Dy moments along the $[00\bar{1}]$ axis

(Figure 4.24(c)). Finally the sample is then rotated back through 90°. The Dy moments should now be aligned perpendicular to the applied field as shown schematically in the inset of Figure 4.24(d).

If an applied field is then directed along the [110] axis the Dy moments will attempt to rotate to align with the applied field but this is resisted by the strong Dy^{3+} crystal field anisotropy. In larger applied fields the Dy spins are pulled out of plane to align with either the [010] or the [100] easy axis.

To ensure that the state is defined correctly and that the Dy moments were aligned along the $[00\bar{1}]$ axis (perpendicular to the x-ray beam) the sample was rotated from 0° to 100°, in zero applied field while monitoring the Dy XMCD. When the magnetisation is aligned perpendicular to the beam the XMCD signal should be zero. The results can be seen in Figure 4.25.

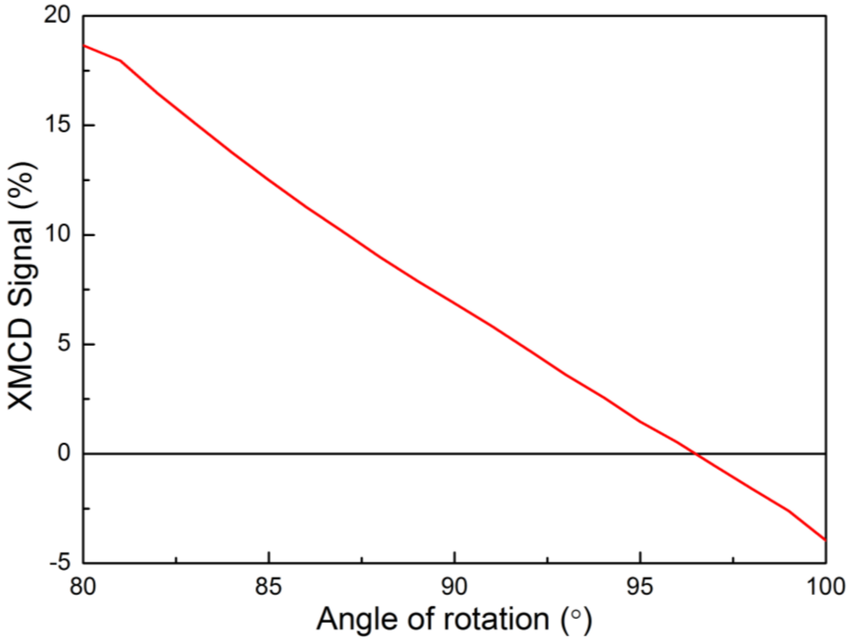

Figure 4.25: Dy XMCD signal at 100 K with $B_a = 0$ T. 90° corresponds to the [110] along x-ray beam.

The Dy XMCD which was expected to equal 0% at 90° in fact occurred at an angle of ≈96°, this we attribute to the formation of non-isotropic domains due to anisotropy when B_a=0 T, or noncollinear spin and orbital moments.

4.13 Dy-XMCD results for the-$DyFe_2$/YFe_2 transverse exchange spring

Figure 4.26 shows the Dy magnetisation hysteresis loop for the superlattice at a temperature of 100 K with the applied field 6° away from the [001] axis thereby allowing for the x-ray beam to hit the sample at grazing incidence. The black curve was collected by cycling the applied magnetic field between ±12 T. On closer inspection of the hysteresis loop it can be noted that there is a change in gradient when the XMCD signal approaches $B_a = \pm 3$T. To investigate this further a minor loop was performed (blue loop). Saturating the sample at 12 T (a) then reducing the field to B_a = -3.2 T (b) and then subsequently returned to zero. This minor loop resembles a smaller version of the full loop showing that only one step of the two step reversal is accessed. Between points (*ii*) and (*iii*) the Dy moments are clearly not aligned either antiparallel or parallel to the applied field.

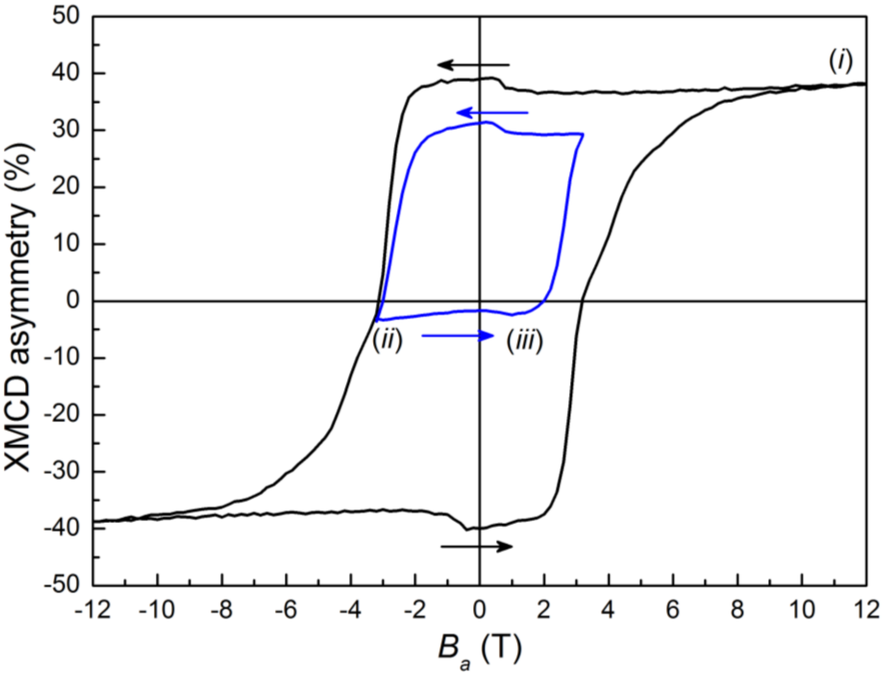

Figure 4.26: Dy XMCD magnetisation loop. Full (minor) loop is black (blue) respectively. Applied field 6° away from the [001] axis.

On cycling the magnetic field between points (*ii*) and (*iii*) it was found that the Dy XMCD is (a) reversible provided that one avoided the upturn in the blue curve (B_a>2 T) and (b) that the asymmetry of the Dy XMCD is very weak. The latter is shown more clearly in Figure 4.27.

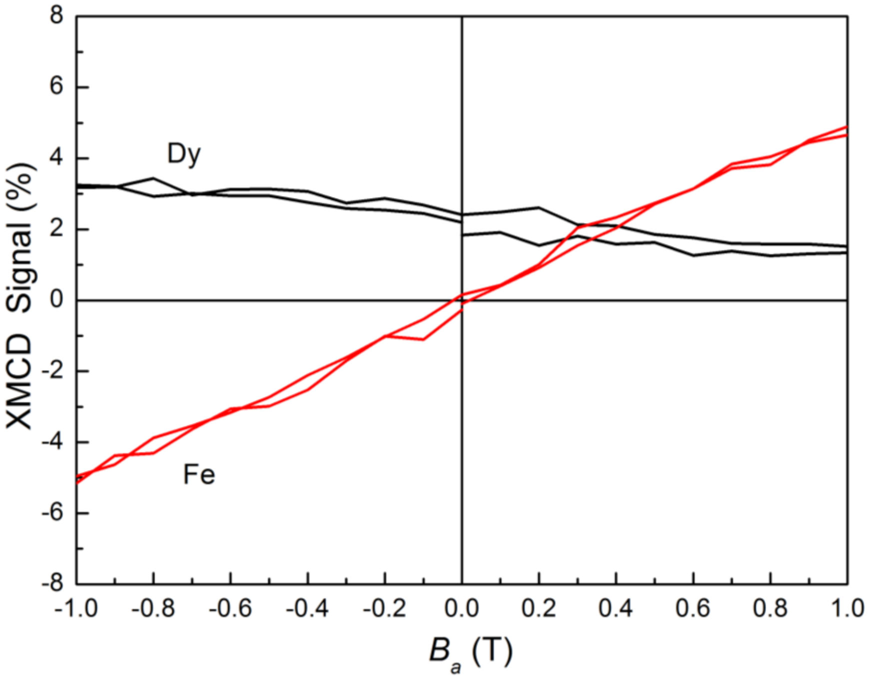

Figure 4.27: Dy (black) and Fe (red) XMCD reversible magnetisation curves in the range ±1 T at 100 K, for the transverse exchange spring state.

The weak Dy XMCD corresponds with the Dy moments now at right angles to the magnetic field pointing in the plane of the sample *i.e.* a transverse exchange spring state. By contrast, the Fe-XMCD signal is much larger, over the reversible field range. This is to be expected given that the Fe moments in the soft YFe_2 layers are free to rotate into the direction of the applied field, beyond this field range (±1 T), irreversibility rapidly sets in. In summary the results support (*i*) a double step magnetic reversal process and (*ii*) the existence of an intermediate transverse exchange spring.

The results from the Fe XMCD obtained over a much larger field range can be seen in Figure 4.28. It indicates the presence of the exchange spring in the second and fourth quadrants of the hysteresis loop. The partial loop in Figure 4.28 (blue) was obtained in the same way as the minor loop detailed above for Dy starting from B_a=12 T then reducing to -3.2 T before cycling between ±1 T. The partial loop is completely reversible and centred near zero. This is also in agreement with the existence of a transverse exchange spring in small applied fields. In summary therefore the reversal mechanism can be described as switching from an in-plane [001] reversed antiferromagnetic state to an out-of-plane [100] transverse exchange spring and then to an in-plane $[00\bar{1}]$ exchange spring state.

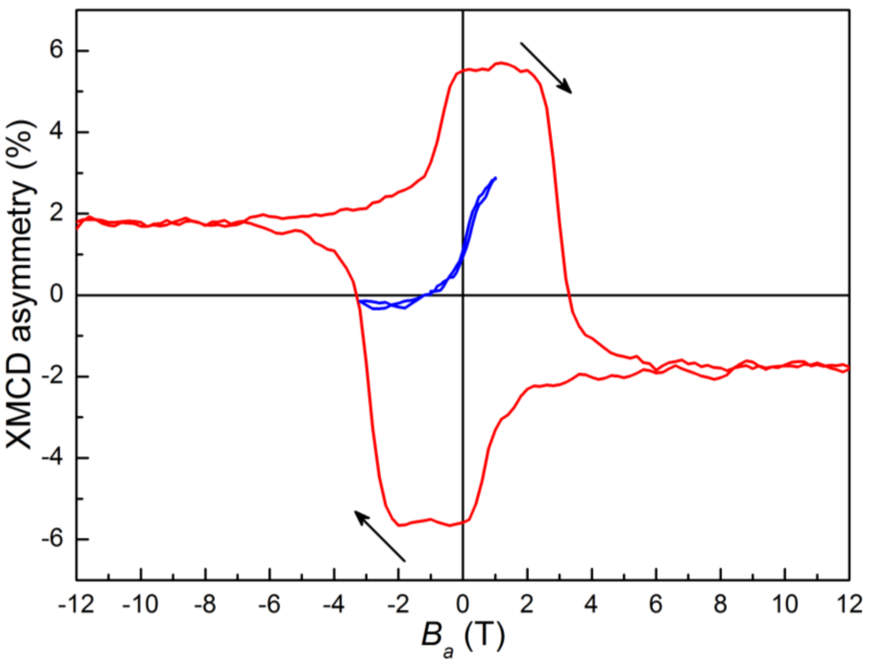

Figure 4.28:Fe XMCD magnetisation curve at 100 K. Full (partial) loops are shown in red (blue) respectively.

Dy-XMCD measurements were also obtained starting from B_a = 0 T in a prepared transverse exchange spring state (as discussed in Figure 4.24) with the magnetic field applied along a hard [110]-axis. The results can be seen in Figure 4.29.

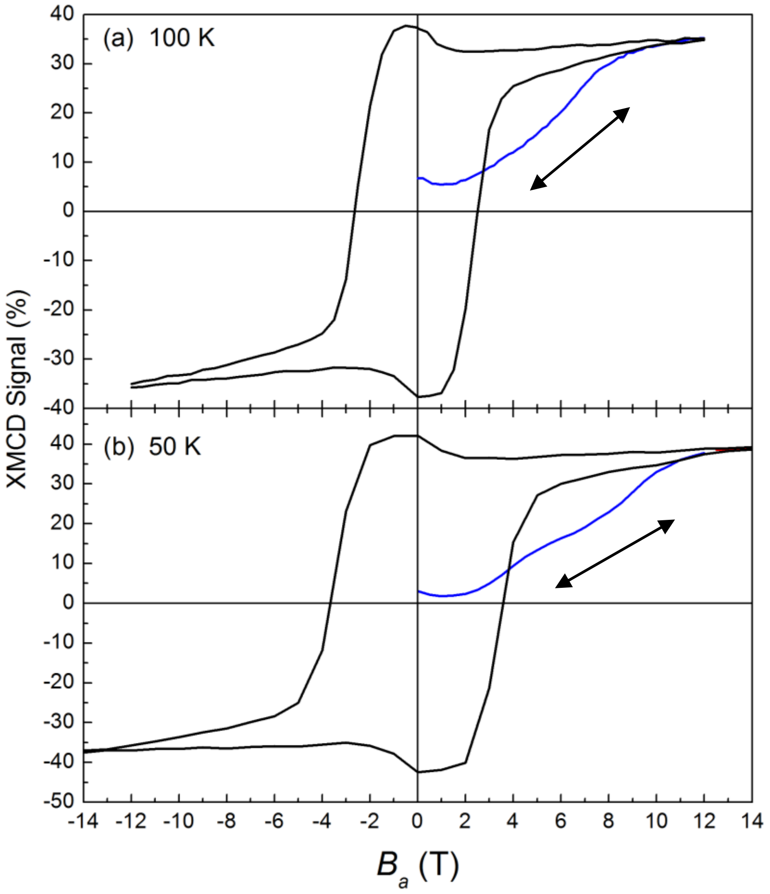

Figure 4.29: Dy XMCD magnetisation curves for (a) 100 K, (b) 50 K. The blue line is starting from the transverse exchange spring state. Applied field along the [110] axis.

Partial loops show that the Dy XMCD loops are now far from reversible (black hysteresis loops in Figure 4.29). The Dy moments have been pulled up out of the film plane to exploit easy out of plane [010] or [100] axes. The reason for this behaviour can be understood by reference to Figure 4.30, which shows the anisotropy surface associated with the Dy^{3+} ions.

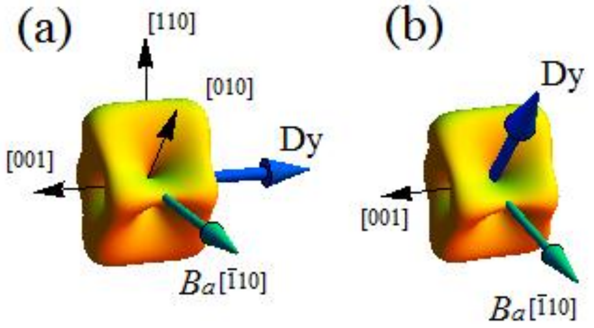

Figure 4.30: Crystal field anisotropy surface for the Dy^{3+} ion at 100 K. (a) After initial preparation the Dy moments (blue) point along the easy $[00\bar{1}]$ (b) After a large applied magnetic field applied along the $[\bar{1}10]$ axis and subsequently reduced to zero, the Dy moments point along an out of plane [010] axis.

Once the Dy spins have reached the [010]-axis as shown in Figure 4.30(b), they cannot return to the in-plane $[00\bar{1}]$-axis. The magnetic loop is then characterised by an irreversible out of plane exchange spring system.

4.14 *RE*Fe$_2$ exchange spring conclusion

In this chapter we have studied two exchange spring systems. Using a variety of techniques from bulk magnetometry and computational modelling to XMCD, new exchange spring states have been discovered. Bulk magnetometry in both cases shows additional weak transitions masked by the large exchange spring of the thicker YFe$_2$ layers. Rare earth XMCD has allowed the probing of the individual layers to pinpoint the origin of these additional transitions, which otherwise would not have been possible. This study into exchange spring behaviour has therefore given a greater insight into the various switching and reversal mechanisms in these systems. The insights gained in this study will aid understanding the family of exchange spring multilayers which have the potential for magnetic data storage. The conclusions for the individual exchange spring systems is presented below.

Spin-flop ErFe$_2$/YFe$_2$

It has been shown that XMCD experiments carried out using the Er $M_{4,5}$ edge reveals incisive information concerning magnetic reversal in a ErFe$_2$/YFe$_2$ system. Measurements reveal a crossover from a single magnetic switch at T<200 K to a double magnetic switch at T>220 K, in agreement with conclusions originally inferred from bulk magnetometry [18]. In addition, micromagnetic modelling was found to give good agreement with the double switching observed in the XMCD data [20]. The latter was traced to instabilities in the spin-flop and vertical exchange spring configurations at approximately 200 K. This instability was finally traced back to the Er^{3+} single ion anisotropy surface in particular the existence of low energy saddle points between $\langle 111 \rangle$ type directions (see Figure 4.5) allowing the Er magnetic moments to change direction relatively easily avoiding any large changes in magnetic anisotropy.

Transverse exchange spring DyFe$_2$/YFe$_2$

Magnetic reversal in a DyFe$_2$/YFe$_2$ multilayer system has been investigated using XMCD. It has been shown that the reversal mechanism can be described as first a switch from an in-plane [001] antiferromagnetic state to an out-of-plane [100] transverse exchange state, followed later by a transition to an in-plane $[00\bar{1}]$ exchange spring. This system can be seen as a model case for magnetic reversal. In addition, a history dependent procedure has been presented for the preparation of transverse exchange spring states.

Furthermore, from an experimental point-of-view it is worth noting that the ability to rotate the sample obviates the need for two mutually orthogonal fields. This is a serious consideration when large magnetic fields are required. Moreover, rotation also allows four different classes of $DyFe_2/YFe_2$ magnetic exchange springs to be accessed. These are: (*i*) an easy axis in plane spring, (*ii*) a hard axis out of plane spring, (*iii*) an in plane transverse spring and (*iv*) an out of plane transverse spring.

References

1. D. Suess, T. Schrefl, R. Dittrich, M. Kirschner, F. Dorfbauer, G. Hrkac, and J. Fidler, *J. Mag. Mag. Mater.* **290,** 551. (2005).
2. D. Suess, T. Schrefl, S. Fahler, M. Kirschner, G. Hrkac, F. Dorfbauer, and J. Fidler, *Appl. Phys. Lett.* **87,** 012504. (2005).
3. R. H. Victora, and X. Shen, *IEEE Trans. Mag.* **41,** 537. (2005).
4. R. Skomski, and J. M. D. Coey, *IEEE Trans. Mag.* **29,** 2860. (1993).
5. R. Skomski, and J. M. D. Coey, *Phys. Rev. B.* **48,** 15812. (1993).
6. M. R. J. Gibbs, *J. Magn. Mag. Mater.* **290,** 1298. (2005).
7. A. Ludwig, and E. Quandt, *J. Appl. Phys.* **87,** 1691. (2000).
8. C. T. Pan, and S. C. Shen, *J. Mag. Mag. Mater.* **285,** 422. (2005).
9. E. F. Kneller, and R. Hawig, *IEEE Trans. Mag.* **27,** 3588. (1991).
10. G. J. Bowden, D. St. P. Bunbury, A. P. Guimaraes, and R. E. Snyder, *J. Phys. C.* **1,** 1376. (1968).
11. K. H. J. Buschow, *Rep. Prog. Phys.* **40,** 1179. (1977).
12. R. L. Cohen, *Phys. Rev.* **134,** A94. (1964).
13. http://www.geocities.jp/ohba_lab_ob_page/structure5.html
14. J. –M. L. Beaujour, *Ph. D. Thesis*, University of Southampton, UK (2003).
15. E. Goto, N. Hayashi, T. Miyashita, and K. Nakagawa, *J. Appl. Phys.* **36,** 2951. (1964).
16. G. E. Moore, *Electronics Magazine.* **38,** (1965).
17. S. N. Gordeev, J. -M. L. Beaujour, G. J. Bowden, B, D. Rainford, and P. A. J. de Groot, *Phys. Rev. Lett.* **87,** 186808, (2001).
18. K. N. Martin, K. Wang, G. J. Bowden, A. A. Zhukov, J. P. Zimmermann, H. Fangohr, R. C. C. Ward, and P. A. J. de Groot, *Appl. Phys. Lett.* **89,** 132511. (2006).
19. K. N. Martin, C. Morrison, G. J. Bowden, R. C. C. Ward, and P. A. J. de Groot, *Phys. Rev. B.* **78,** 172401. (2008).
20. G. B. G. Stenning, A. R. Buckingham, G. J. Bowden, R. C. C. Ward, G. van der Laan, L. R. Shelford, F. Maccherozzi, S. S. Dhesi, and P. A. J. de Groot, *Phys Rev. B.* **84,** 104428. (2011).
21. J. P. Zimmermann, G. Bordignon, R. P. Boardman, T. Fishbacher, H. Fangohr, K. N. Martin, G. J. Bowden, A. A. Zhukov, and P. A. J. de Groot, *J. Appl. Phys.* **99,** 08B904. (2006).
22. G. van der Laan, and B. T. Thole, *Phys. Rev. B.* **43,** 13401. (1991).
23. G. J. Bowden, K. N. Martin, B. D. Rainford, and P. A. J. de Groot, *J. Phys: Condens. Matt.* **20,** 015209. (2008).
24. U. Atzmony, and M. P. Dariel, *Phys. Rev.B.* **13,** 4006. (1976).
25. G. J. Bowden, P. A. J. de Groot, B. D. Rainford, K. Wang, K. N. Martin, J. P. Zimmermann, and H. Fangohr, *J. Phys: Condens. Matt.* **18,** 5861. (2006).

26. K. N. Martin, P. A. J. de Groot, B. D. Rainford, K. Wang. G. J. Bowden, J. P. Zimmermann, and H. Fangohr, *J. Phys:. Condens. Matt.* **18,** 459. (2006).

27. J. –M. L. Beaujour, S. N. Gordeev, G. J. Bowden, R. C. C. Ward, M. R. Wells, B. D. Rainford, and P. A. J. de Groot, *Appl. Phys. Lett.* **78,** 964. (2001).

28. G. J. Bowden, J. –M. L. Beaujour, A. A. Zhukov, B. D. Rainford, P. A. J. de Groot, R. C. C. Ward, and M. R. Wells, *J. Appl. Phys.* **93,** 6480. (2003).

29. G. J. Bowden, A. R. Buckingham, G. B. G. Stenning, and P. A. J. de Groot, *J. Phys. Condens. Matter.* **22,** 291001. (2010).

30. R. C. O'Handley, *"Modern Magnetic Materials; Principles and Applications,"* Wiley Interscience (Wiley and Sons, Inc. 2000).

31. K. Dumesnil, C. Dufour, Ph. Mangin, A. Rogalev, and F. Willhelm, *J. Phys. Condens. Matt.* **17,** 215. (2005).

32. K. Dumesnil, S. Fernandez, A. Avisou, C. Dufour, A. Rogalev, F. Willhelm, and E. Snoeck, *Eur. Phys. J. B.* **72,** 159. (2009).

33. G. B. G. Stenning, G. J. Bowden, S. A. Gregory, J. –M. L. Beaujour, A. N. Dobrynin, L. R. Shelford, P. Bencok, P. Steadman, T. Hesjedal, G. van der Laan, P. A. J. de Groot, *Appl. Phys. Lett.* **101,** 072412. (2012).

34. G. B. G. Stenning, G. J. Bowden, S. A. Gregory, A. N. Dobrynin, L. R. Shelford, P. Bencok, P. Steadman, T. Hesjedal, G. van der Laan, P. A. J. de Groot, *Phys. Rev. B.* **86,** 174420. (2012).

35. E. Goering, J. Will, J. Geissler, M, Justen, F. Weigand, G. Schuetz, *J. Alloys. Comp.* **328,** 14. (2001).

36. J. Als-Neilsen, D. McMorrow, "Elements of Modern X-ray physics," (Wiley and Sons, Ltd 2001).

37. D. Attwood, "Soft X-rays and extreme ultraviolet radiation: Principles and applications," (Cambridge University Press, 2007).

38. A. Thompson, D. Attwood, E. Gullikson, M. Howells, K. –J. Kim, J. Kortright, I. Lindau, Y. Liu, P. Pianetta, A. Robinson, J. Scofield, J. Underwood, G. Williams, H. Winick, "*X-ray data booklet*," Lawrence Berkeley National Laboratory (Third edition, 2009).

39. http://www.diamond.ac.uk/Home/Beamlines/I10/layout.html

40. B. H. Frazer, B. Gilbert, B. R. Sonderegger, G. De. Srasio, *Surf. Sci.* **537,** 161. (2003).

5. X-rays studies and magnetisation dynamics in exchange coupled bilayers

In the study of magnetic films the speed and character of magnetic reversal is an important topic. In particular the reaction of the magnetisation to a fast time-dependent magnetic field involves numerous parameters such the *g*-factor, natural resonances, magnetic anisotropy and damping.

This knowledge of magnetisation dynamics is relevant for their many uses in applications. In recent years magnetic multilayers have attracted a great deal of attention because of their potential application in data storage media [1-3], MEMS [4-6], nonreciprocal microwave devices [7] and magnetic garnets in low-loss microwave devices. In applications it is important to have a detailed knowledge of the magnetisation dynamics as manipulating the magnetic sample may yield increased read and write speeds of magnetic hard drives and increase/decrease strong switching and damping [8].

In this chapter the results of ferromagnetic resonance experiments, obtained using broadband VNA-FMR techniques, are presented and discussed. This experimental technique is standard for determining the magnetisation dynamics of a system. The experimental technique is described in Ch. 3, section 3.5.

The samples detailed here are transition metal magnetic films and magnetic garnets. In addition to the transition metal films, rare earth (*RE*'s) magnetic multilayer films such as $DyFe_2/YFe_2$were also studied. The latter however did not yield any useful results, due to large magnetisation of the film and more crucially because of damping due to the large anisotropy associated with the *RE*s. To observe the *RE*-FMR high power pulsed rf fields or optical pump-probe techniques must be used instead of continuous wave methods. For the remainder of this thesis only transition metal films and magnetic garnets, which are characterised by low damping were investigated.

5.1 History of magnetisation dynamics

Much research has been carried out into magnetisation dynamics with the main focus upon the transition metals and magnetic garnets. The latter are characterised by a weak damping term in the Landau-Lifshitz-Gilbert equation (see section 2.9). Much of the early research has been carried out using cavity FMR. However in recent years planar FMR has become the primary focus of interest since it offers new potential applications. Advantages of planar FMR over cavity are: (*i*) broadband capability, (*ii*) small and easy to include in an experimental setup, such as high field and synchrotron experiments and (*iii*) well suited for magnetic thin films. Substantial early work on magnetisation dynamics had been performed on bulk materials such as yttrium iron garnet (YIG). In particular, the various magnetostatic modes of these materials have been identified [9]. In addition experiments have been performed by Walker [10] who detailed the resonant modes of a manganese ferrite sphere. This showed that the h_{rf} field direction in relation to the applied field gives rise to multiple resonance peaks dependent on the geometry of both fields. A sphere was used to minimise the demagnetisation factors (see Ch. 2, section 2.6). In contrast Damon and Eshback [11] investigated the modes of a ferromagnetic slab. In the 1960s research moved onto investigating the properties of discs and rods (Dillon [12]). This yielded information about the linewidth of the resonances and various modes. These additional modes can occur at applied fields both above and below the Kittel equation for a flat magnetic film (Ch. 2, Eq. 2.13) [13]. Recently, the spotlight has moved onto transition metal thin films which are the predominant material used in magnetic data storage. Magnetic tunnel junctions and magnetic multilayers have also become the focus of recent research. By investigating the damping parameters and the exchange between the adjacent layers, Stamps *et al*. [14, 15] and Martin *et al*. [16] have contributed much information in this research area. In the last few years however research into thin film multilayers using synchrotron techniques, has given further depth to our understanding of their behaviour [17].

5.2 Results of exchange-coupled transition metals

Figure 5.1 shows a typical ν-B_a map, of a simple transition metal film. It shows the normalised transmission parameter $\left|S_{21}^{N}\right|$ (described in Ch. 3). The composition of the film is:

$$\text{Fe (30 Å)/Pt (300 Å)/Ni}_{0.81}\text{Fe}_{0.19}\text{ (400 Å)/Pt (50 Å)}$$

It was grown by MBE (see Ch. 3). What can be observed is the FMR absorption as a function of applied field and frequency.

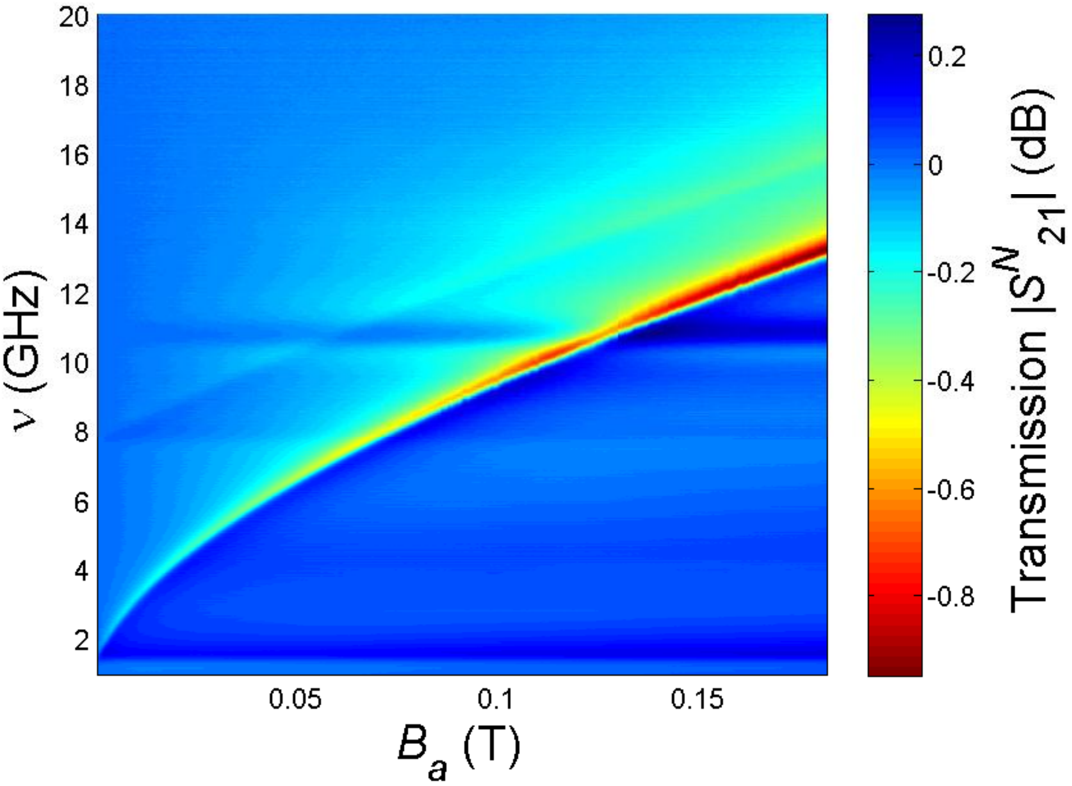

Figure 5.1: ν-B_a map showing the FMR of a NiFe film.

The frequency-field (ν-B_a) map displayed in Figure 5.1 shows the FMR of the NiFe film. The FMR follows the simple Kittel formula (Eq. 2.13). The horizontal streaks which can appear across the ν-B_a map are parasitic resonances arising from the CPW itself. This is due to the CPW being an effective microwave cavity. A close inspection of Figure 5.1 reveals that there are two features to be noted. Firstly, the linear resonance which is much weaker than the main resonance, this is the ferromagnetic anti-resonance [18]. Secondly, the absorption varies in the range of 0.1 dB → -0.9 dB which is a large dynamic absorption range for a thin magnetic film.

The next sample investigated was a NiFe/CoFe bilayer film, to provide insight into the physics behind the coupling of ferromagnetic films with a view to potential for applications. The sample has the following composition:

Fe (30 Å)/Pt (300 Å)/$Ni_{0.81}Fe_{0.19}$ (400 Å)/$Co_{0.9}Fe_{0.1}$ (400 Å)/Pt (50 Å)

The Fe and Pt are grown to provide a seed and buffer layer respectively (Ch. 3, Section 3.2).

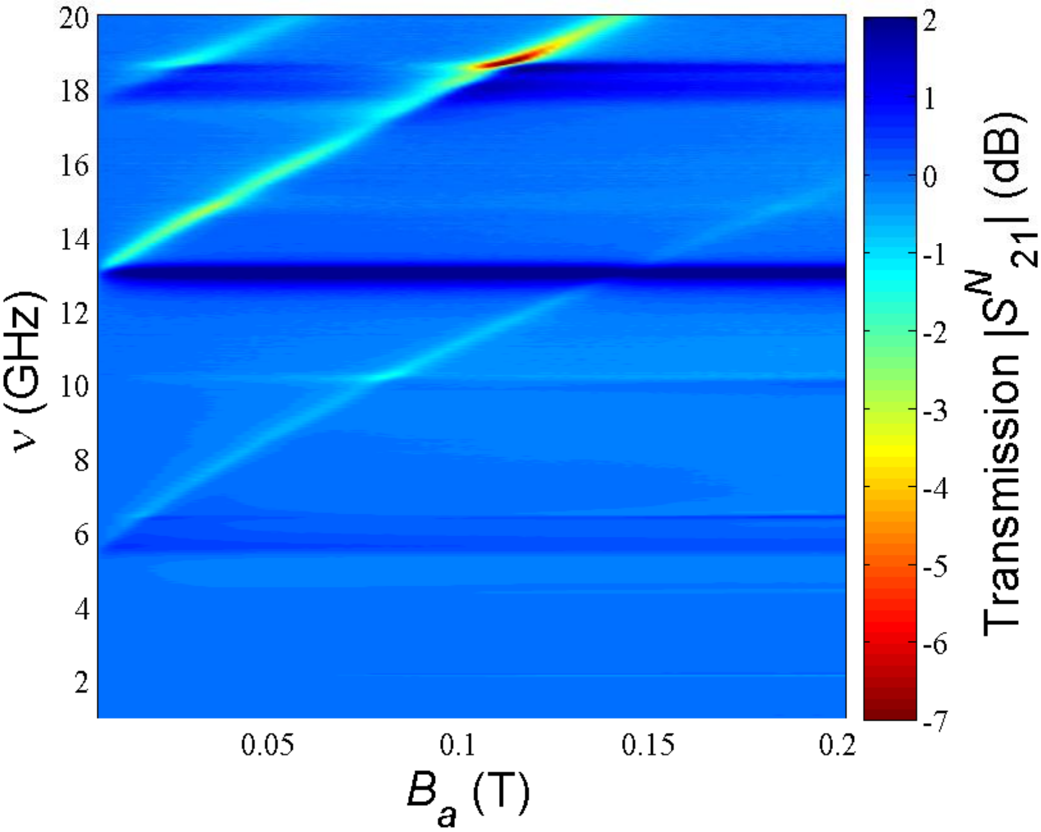

Figure 5.2: ν-B_a map of a $Ni_{0.81}Fe_{0.19}$ (400 Å)/$Co_{0.9}Fe_{0.1}$ (400 Å) bilayer system. Horizontal streaks are parasitic resonances.

The sample displayed in Figure 5.2 shows a very different ν-B_a response from that in Figure 5.1. The primary difference is the evidence of multiple resonances. For simplicity the ν-B_a map is now only displayed in positive applied fields as the FMR is symmetrical about the magnetisation direction (no exchange bias). Multiple resonances arise because the FMR of NiFe and CoFe layers must now be considered. This bilayer system cannot be simply described in terms of the FMR of each constituent layer (NiFe, CoFe) because the two magnetic layers are exchange-coupled to one another. Exchange coupling (covered in Ch. 2) results in a preferred direction of the magnetisation in the two layers being transferred across the interface when two different magnetic materials are in close contact with one another. Hence the resonant modes visible in Figure 5.2 are in effect the exchange-coupled FMR modes of the NiFe/CoFe bilayer system.

The FMR spectroscopy rig was built at Southampton University and when used with this type of sample presents some limitations of the technique. Most noticeably, with the sample described in Figure 5.2, because (*i*) limited range in that only resonances up to 20 GHz can be studied, (*ii*) as usual in FMR, it is a bulk technique and does not give information on the behaviour of the individual layers and (*iii*) that the S-parameters (S_{21}) is proportional to the amplitude of the resonance as the CPW presents an inhomogeneous rf-field, so the amount of magnetic material coupled to the CPW is critical for the observed amplitude.. For determining which resonant mode originates from which layer and also for the determination of other parameters such as: the damping parameter (α from Eq. 2.12, Ch. 2), the cone angle of precession ('amplitude of resonance') [19] as well as the relative phase of the magnetic layers, time resolved FMR must be undertaken. This detail is conveniently offered by x-ray detected ferromagnetic resonance (XFMR) [17, 19]. The subject will be covered in more detail in section 5.7.

In Figure 5.2 the absorption varies with the resonant mode in question. For example the absorption of the three modes at $B_a = 0.025$ T with an increase in frequency give absorptions of 0.5, 2.4 and 1.67 dBm respectively. This demonstrates that each resonance does not precess with the same amplitude and is dependent upon the type of each mode.

Figure 5.1 at $B_a = 0$ T shows that the FMR absorption occurs at very low frequency (< 1 GHz). This is very different from that of Figure 5.2 where at $B_a = 0$ T there are three resonant modes at ≈ 6, 13 and 18 GHz. The shift between these modes is driven primarily by the anisotropy of the magnetic bilayer. The effective field then describing the system is:

$$\overline{H}_{eff} = \overline{H}_a + \overline{H}_{dem} + \overline{H}_k \qquad (5.1)$$

Eq. 5.1 shows the individual terms of $\overline{H}_{eff}$ where, $\overline{H}_{dem}$ is the demagnetising field and $\overline{H}_k$ the anisotropy fields that contribute to the Kittel equation for thin films. The in-plane applied field is defined as $\overline{H}_a$, see Eq. 5.1. $\overline{H}_k$ the anisotropy field is which is the field needed to saturate the magnetisation in the hard direction. It is the anisotropy field arising from the CoFe layer which offsets the different resonant modes in the vertical direction in the ν-B_a map. It is apparent in Figure 5.1 which consists of a single layer of NiFe showing no such effects. The reason why three modes are present however is not simple. This will require the use of XFMR which provides layer-specific information. Nonetheless they can for the time being, be assumed to be different spin wave modes of the bilayer system.

Exchange coupling between a hard magnetic layer, such as CoFe, to a softer NiFe layer yields multiple resonances all shifted to higher resonant frequencies. By manipulating the CoFe ratio it may be possible to achieve other systems with lower frequency resonant modes using the Slater-Pauling curve for CoFe [20]. This determines the composition of the CoFe with respect to the Bohr magneton thereby controlling the magnetic moment and hence, resonant frequency of the system based upon the Kittel resonance equation [13].

Changing the composition of the bilayer from $Co_{0.9}Fe_{0.1}$ to $Co_{0.5}Fe_{0.5}$ gives very different results. The NiFe composition remained the same as previously, as did the thicknesses of the layers. The sample for which the data is shown in Figure 5.3 has the composition of:

Fe (30 Å)/Pt (300 Å)/$Ni_{0.81}Fe_{0.19}$ (400 Å)/$Co_{0.5}Fe_{0.5}$ (400 Å)/Pt (50 Å)

The change in composition of the CoFe brings about some differences (compare Figure 5.2 and 5.3). Notably there are only two resonant modes instead of three and both now occur at lower frequencies. As the two observable resonant modes both appear at $B_a = 0$ T below 10 GHz, this sample is well-suited for XFMR experiments at Diamond (for experimental reasons the maximum frequency that can be investigated is approximately 10 GHz; this is explained further in section 5.4).

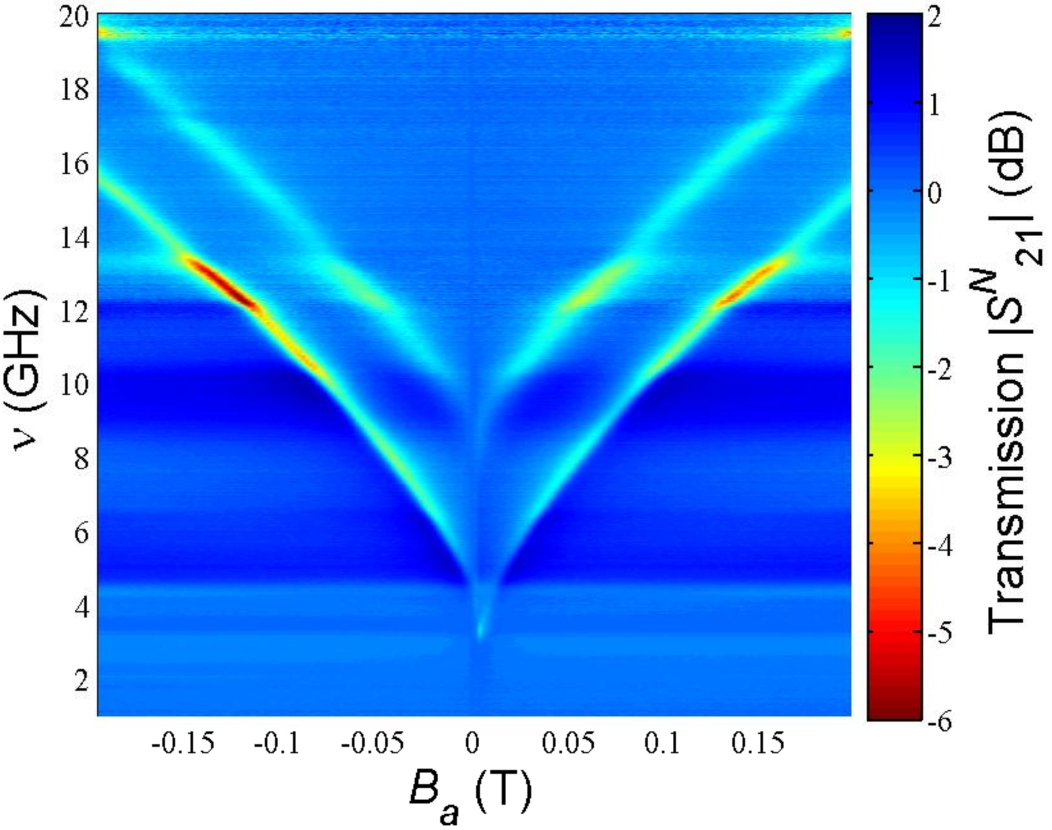

Figure 5.3: ν-B_a map of a $Ni_{0.81}Fe_{0.19}$ (400 Å)/$Co_{0.5}Fe_{0.5}$ (400 Å) bilayer film.

The absorption between the two modes again differs by 0.3 dBm at $B_a = 0.05$ T with an increase in frequency. By taking an individual field sweep at fixed excitation frequency a cross-section of the ν-B_a map is obtained. An example is given in Figure 5.4. An excitation microwave frequency 9.5 GHz was chosen so that both modes would be visible. The microwave absorption is greater and the full-width half maximum (FWHM) of both modes is 16 mT for the FMR at $B_a = 70$ mT (c) and is broader than the FMR at $B_a \approx 0$ T (a) even though the mode is incomplete. The middle resonant mode (b) visible in Figure 5.4 arises from the Fe seed layer due to patterning of the sample and will be discussed in more detail with XFMR results. In comparison the FWHM of a NiFe film as in Figure 5.1 is 9.56 mT at 9.5 GHz because of weaker damping. In practice, the FWHM can be used to determine the damping parameter α which appears in the LLG equation.

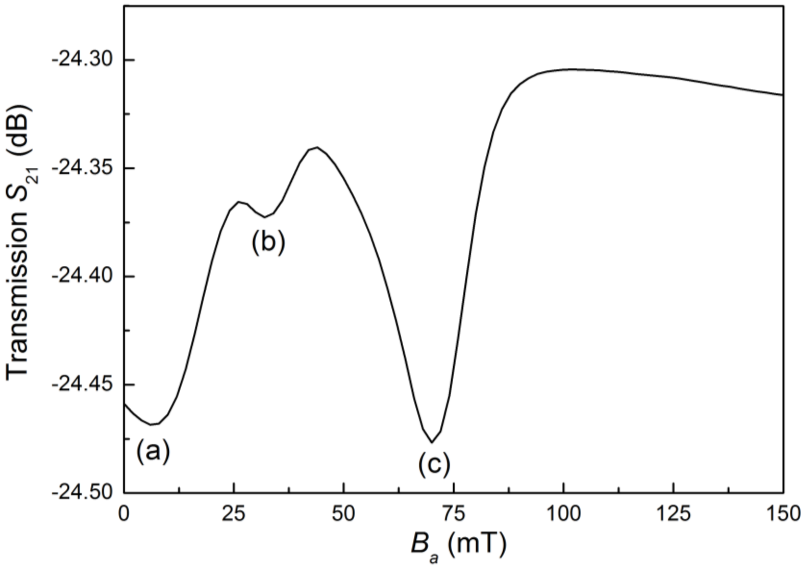

Figure 5.4: Field sweeps at constant microwave excitation of 9.5 GHz of the $Ni_{0.81}Fe_{0.19}$ (400 Å)/$Co_{0.5}Fe_{0.5}$ (400 Å) bilayer.

A magnetic hysteresis loop of the bilayer in question can be observed in Figure 5.5. It was obtained using an MPMS SQUID vibrating sample magnetometer (VSM) in the temperature range 4-300 K and in fields of 0-±7 T (This technique is described in greater detail in Ch. 3). VSM is a bulk magnetometry technique and can give an absolute value of the saturation magnetisation. The double switching seen in Figure 5.5 (a) is in good agreement with measurements taken in-situ during the growth of the sample (see Ch. 3). This indicates that there is a good interface between the adjacent layers of the bilayer indicating strong exchange coupling. It is highlighted in Figure 5.5(a) that the double switching of the magnetisation would take on a sharper switching at B_a=0 if the magnetic layers were acting independently. However, it is shown that there is a curve rather than the sharp switching, this suggests a rotation of the magnetisation (red circle (Figure 5.5)) until a sufficiently high applied field is reached to switch one of the layers.

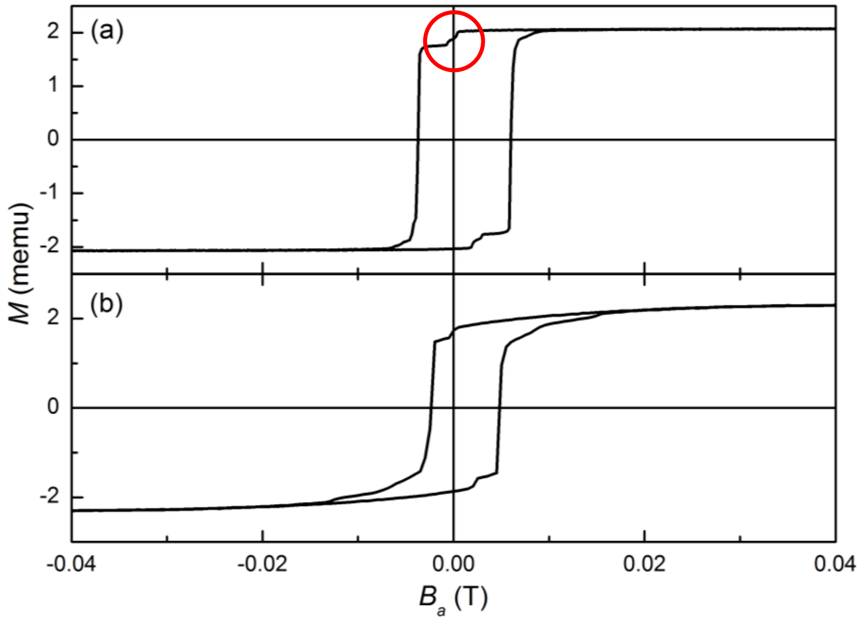

Figure 5.5: Magnetic hysteresis loop of a $Ni_{0.81}Fe_{0.19}$ 400 Å/$Co_{0.5}Fe_{0.5}$ 400 Å bilayer with the applied magnetic field in-plane along the (a) easy axis, (b) hard axis of magnetisation.

The hysteresis loop of the NiFe/CoFe bilayer with a magnetic field applied along the hard direction of magnetisation can be seen in Figure 5.5(b). In an attempt to understand the anisotropy of the bilayer, angle dependent FMR measurements were performed. These measurements involved sweeping the applied magnetic field at a fixed excitation frequency while continuously monitoring the microwave absorption. Field sweeps were taken every 5° for the full 360°. This was achieved using a vector magnet which allows magnetic fields up to 0.9 T to be applied in any direction. Subsequently a Lorentzian lineshape was then fitted to the FMR peak and the resonance is plotted as a function of the applied field angle as shown in Figure 5.6. The excitation frequency was set to 15 GHz to ensure both resonant modes were clearly visible.

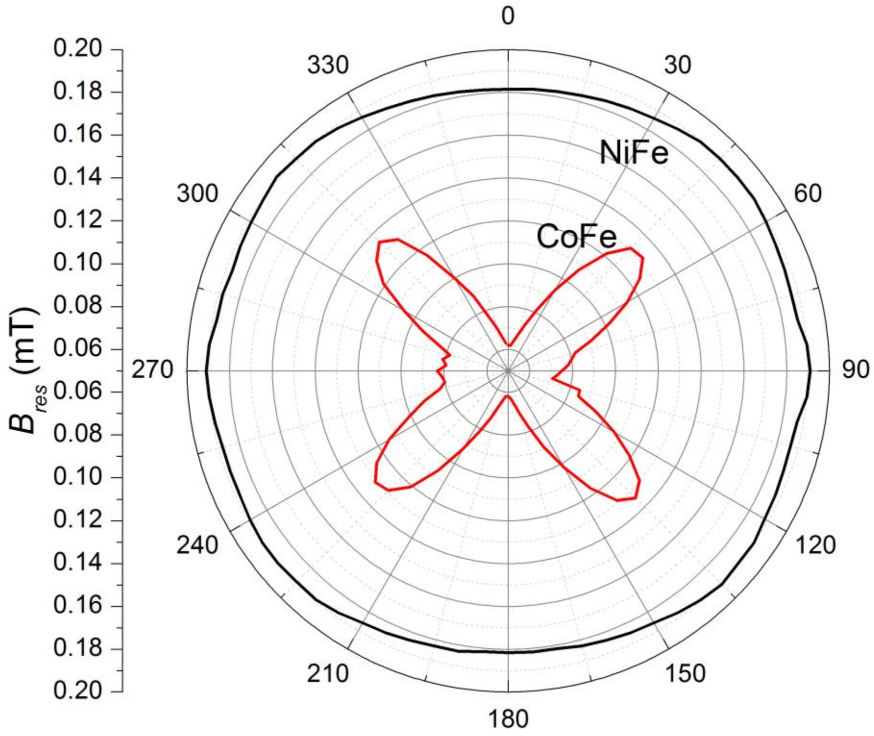

Figure 5.6: Anisotropy plot of the $Ni_{0.81}Fe_{0.19}$ 400 Å/$Co_{0.5}Fe_{0.5}$ 400 Å bilayer as a function of the magnetic field angle. The red (black) represent the two different resonant modes for the high (low) frequency resonant mode. The excitation frequency was set to 15 GHz.

Figure 5.6 displays two very different modes. For a given applied field red (black) corresponds to a high (low) frequency resonant mode. The high frequency FMR mode (red) shows a strong four-fold anisotropy with the easy axis aligned at 0, 90, 180 and 270 ° with the hard axis aligned at 45 ° to these angles. We ascribe this mode, primarily, to the CoFe layer. The second FMR at lower frequencies (black) is mostly isotropic but with an anisotropy related to the high-frequency mode, therefore deviating slightly from a circle associated with an isotropic medium. We ascribe this resonance, to the NiFe layer. The linewidth position as a function of in-plane field angle displayed in Figure 5.6 are anisotropic and the linewidth is a minimum when the field is applied along the easy axis of magnetisation and a maximum when along the hard axis.

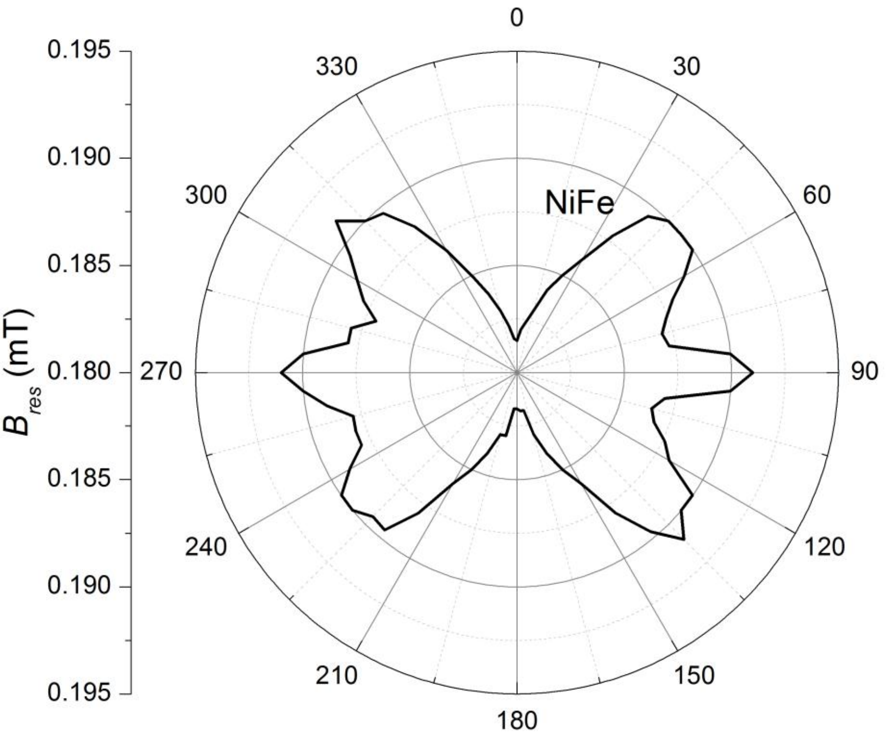

Figure 5.7: High-field NiFe resonance of Figure 5.6 on an expanded scale. The excitation frequency was set to 15 GHz.

Figure 5.7 exhibits an expanded scale of the high field low frequency resonant mode. This demonstrates that this NiFe mode does indeed possess some anisotropy but in comparison to the CoFe mode it is very weak. Samples were also investigated with layer thickness ratios to NiFe:CoFe of 0.5:1, 1:0.5 and 0.5:0.5 all with respect to the sample thickness of 400 Å CoFe/400 Å NiFe. The samples with ratio 0.5:1 and 1:0.5 yield very similar results to that of Figure 5.3. But the ratio of 0.5:0.5 pushes the higher frequency mode to the observable limit (resonant frequency of 19 GHz for B_a = 0.02 T) and is therefore not suitable for XMFR and hence this sample was not pursued further.

Next we will revisit these two modes from an XFMR point of view. Such experiments yield important and conclusive insights into the magnetisation dynamics of the bilayer.

X-ray detected ferromagnetic resonance (XFMR) is now used to study the magnetisation dynamics of a strongly coupled NiFe/CoFe magnetic bilayer grown by molecular beam epitaxy.

5.3 XFMR

The focus here is on an exchange-coupled bilayer sample described earlier namely:

(MgO/Fe (30 Å)/Pt (300 Å)/$Ni_{0.81}Fe_{0.19}$(400 Å)/$Co_{0.5}Fe_{0.5}$(400 Å)/Pt (50 Å))

These materials are commonly used both in research and in applications such as permanent magnets [21-22], nonreciprocal microwave and spin transfer devices [23]. We will show that strong exchange coupling between these two layers leads to increased damping [24] and therefore faster switching behaviour. Such systems are characterised by higher resonant frequencies and therefore potentially faster writing speeds.

Ferromagnetic resonance (FMR) has been widely used to study the magnetisation dynamics of multilayer systems [25-27] and exchange coupled bi- and trilayer films [28]. Both broadband coplanar waveguide (CPW) and cavity FMR techniques have been commonly employed. However both methods are limited in that they can only detect the net response of the multilayer sample. In practice the response of individual layers can only be inferred indirectly by comparing the experimental FMR spectrum with micromagnetic modeling. In contrast x-ray detected FMR (XFMR) is a powerful synchrotron-based experimental technique that allows investigation of 'element selective' magnetisation dynamics [16, 17, 29-35]. The magnetic contrast is provided by x-ray magnetic circular dichroism (XMCD) (see Ch. 4). XMCD is an experimental technique which utilizes the dependence of the polarisation of the x-ray beam (left or right circular) upon the direction of the magnetisation. Specifically XMCD is the difference in absorption between the two different polarisations [34] measured along the direction of the magnetisation. To achieve the layer-specificity the x-ray energy is tuned to an absorption edge of a chosen element which must be unique to that particular layer. Element specificity leads to clear advantages of XFMR over that of FMR. For example when the two layers are magnetically identical the intensity of an optical mode in FMR will be necessarily zero. In such experiments the intensity of the optical mode is proportional to the difference in effective magnetisation of the two layers and inversely proportional to the interlayer exchange [35]. This problem is negated in XFMR where the element specificity can be used to advantage. Phase contrast is provided by stroboscopic XMCD measurements by exploiting the time structure of the synchrotron beam.

5.4 Experimental details

The magnetic bilayer was grown by MBE methods described in Ch. 3. The sample possesses atomically abrupt interfaces and well defined anisotropies. There is a notable four-fold in-plane CoFe anisotropy (see Figure 5.6). This anisotropy induces weak anisotropy in the NiFe layer [36].

Prior to XFMR experiments being performed the sample must first be patterned into a coplanar waveguide (CPW). The reason is two-fold: (*i*) it increases the rf excitation field present in the film and (*ii*) it enables XMCD transmission experiments to be performed. Equation (5.2) below details the relationship between the B_{rf} produced by the CPW, the width of the signal line W and the input power P available [17]:

$$B_{rf} = \frac{\mu_0}{2W}\sqrt{\frac{P}{Z_0}} \qquad (5.2)$$

Here W = 500 μm, Z_0 ≈50 Ω the characteristic impedance and P is the microwave input power (dBm).

The first step in the patterning process s involves depositing a 100 nm of Cu via e-beam techniques atop the bilayer structure. The Cu and the bilayer film were subsequently patterned into a CPW with 50 Ω characteristic impedance, using photolithography and ion etching techniques as described in section 3.7 of Ch. 3. The 50 Ω impedance CPW was designed with the sample properties embedded into the calculations [37] (*i.e.* dielectric constant of the substrate and various thicknesses of the constituent layers) thus ensuring that the transition from sample CPW to PCB is matched as well as possible. The Cu layer atop the magnetic film allows for in-phase excitation of the NiFe and CoFe layers underneath [16] whilst providing a maximum microwave driving field B_{rf} to the underlying NiFe/CoFe film (B_{rf} = 175 μT) [17]. The deposited Cu was sufficiently thin to allow the transmission of the x rays. The patterned sample was then mounted on a CPW by wirebonding as shown in Figure 5.8.

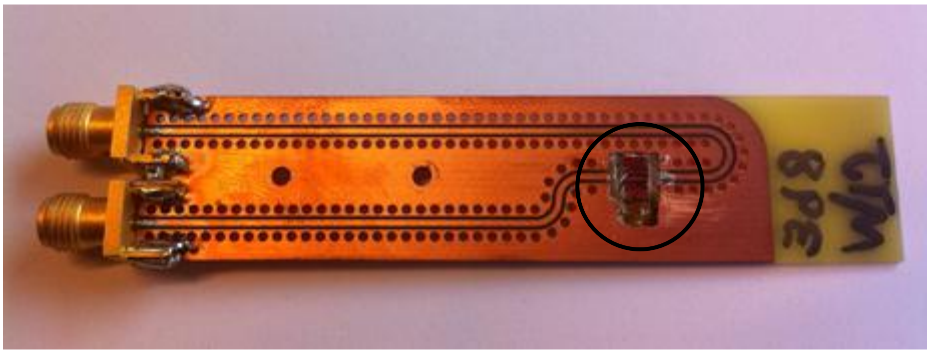

Figure 5.8: Photo of a ready sample patterned as a CPW, wirebond mounted onto a PCB CPW. The sample is indicated by the black circle.

The U-shape of the CPW in Figure 5.8 is unusual due to the requirements imposed by the incoming x-ray beam, the applied field, and the rf-field. The XFMR experiments were performed at beamlines I06 at the Diamond Light Source and PM3 at BESSY II synchrotron light source. The experimental setup is displayed schematically in Figure 5.9. It is similar to that already described in the literature [29, 30].

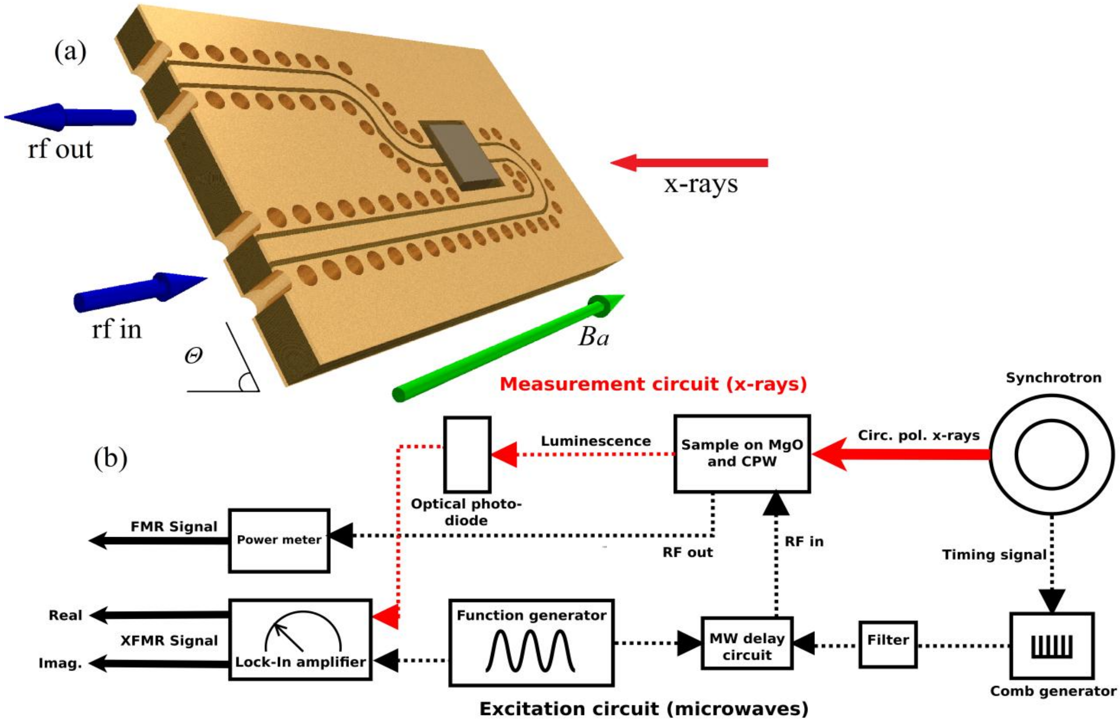

Figure 5.9: (a) A schematic representation of the sample mounted onto a CPW (within the portable octopole magnet system chamber). The holes (vias) improve microwave transmission. The plane of the bilayer sample was set to Θ = 30°, the applied field B_a is 90° to the x-ray beam. (b) XFMR experimental arrangement showing both the microwave excitation circuit and the x-ray detection system. A delay line enables phase shifting of the microwave signal with respect to the x-ray pulses in steps of 0.5 ps.

Phase sensitivity in XFMR is achieved by driving the magnetic resonance at harmonics of the synchrotron storage ring repetition frequency. The repetition rate is ≈500 MHz at both Diamond and BESSY, so the magnetisation dynamics can be driven at integers of 500 MHz. The required harmonics are generated using a custom microwave comb generator (Atlantic Microwave), driven by the master oscillator of the storage ring. Filters and amplifiers were used to select a single high power (25-30 dBm) rf-field for the CPW. A delay line incorporated into the setup enables phase shifting of the microwaves with respect to the x-ray pulses with a 0.5 ps step resolution. The rotation of the magnetisation was detected stroboscopically by measuring the XMCD of the component normal to the static magnetic moment. A limiting factor determining the maximum frequency detectable by XFMR is that set by the pulse width of the x-rays, which is ~35 ps (14 GHz). Other factors bring down the upper frequency such as microwave losses, which limit the upper range of operational frequencies to 11 GHz. Lower frequencies are available at 500 MHz intervals. Timing jitter of the master oscillator signal at Diamond was measured using a spectrum analyzer found to be less than 0.5 ps.

Phase-resolved XFMR requires the sample to be magnetised normal to the incoming x-ray beam [17], while static XMCD measurements require the magnetisation to be projected along the x-ray beam. In practice compromises have to be made and the final arrangement used is shown schematically in Figure 5.8 and 5.9. At the I06 beamline the applied field was supplied by the portable octopole magnet system (POMS). This allows the magnetic field to be applied in any direction up to a maximum of 0.9 T. At BESSY the magnetic field was supplied by two sets of orthogonal coils mounted inside the measurement chamber. Incoming x-rays were incident on the central signal line of the CPW-patterned sample in both cases, therefore avoiding stray fields from non-uniform rf generated by the CPW particularly in the region of the gaps [36]. The sample plane was oriented at a small angle of incidence to the x-ray beam, ensuring that XMCD is sensitive to the in-plane magnetisation dynamics. X-ray absorption was measured in transmission geometry by detecting luminescence emerging from the MgO substrate, caused by secondary electrons. The photo-diode used for this purpose was mounted directly behind the sample.

As indicated earlier a delay line enabled the microwaves to be phase shifted with respect to the x-ray pulses with a 0.5 ps step resolution. XFMR was detected by setting (*i*) the x-ray energy to a resonant absorption edge, (*ii*) the applied field to the FMR value for the chosen frequency and (*iii*) subsequently phase shifting the microwaves with respect to the x-ray pulse. The procedure allows the precession of the spins to be mapped out with an accuracy $\Delta\varphi \sim 7°$ steps at 10 GHz [35]. To double the effective size of the XMCD signal arising from the small angle precession, the phase of the rf-field was switched between 0° and 180°, for each angle φ on the precessional cycle (phase modulation) allowing the use of lock-in detection. Alternatively XFMR can also be measured by sweeping the bias field at a fixed microwave phase with respect to the x-ray pulses. For each point in an XFMR scan the XAS signal below the resonance absorption energy is subtracted from that at the resonance to yield a relative XMCD amplitude signal.

5.5 VNA characterisation of hybrid modes

The VNA-FMR 'flip-chip' [38] results obtained using the bilayer NiFe/CoFe film have previously been presented (see Figure 5.3 and 5.4). The 2D ν-B_a plot of the measured transmission S_{21} [39] shows that there are two principle resonance branches. For the purpose of this thesis they will be labelled as the lower (higher) frequency branch and the 'acoustic-natured mode (NiFe type mode)' ('optic-natured mode' (CoFe type mode)) respectively. This is in line with similar observations for coupled identical ferromagnetic layers reported by Martin *et al.* [16] and Crew *et al.* [15] who observed an optic and acoustic mode over a narrow field range. In the lower frequency mode all the spins in both layers rotate in phase. Whilst in the high frequency mode the spins in the two magnetic layers rotate out-of-phase with respect to each other. This is shown schematically in Figure 5.10.

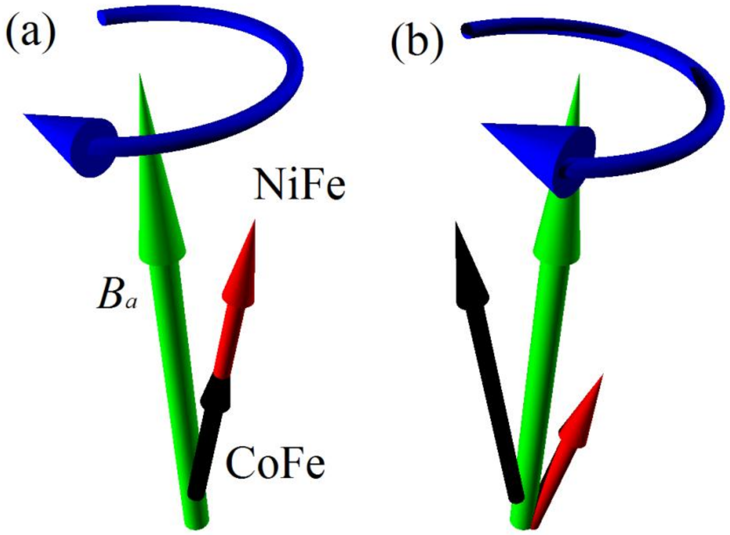

Figure 5.10: Schematic representation of the magnetic (a) acoustic-natured (low frequency) and (b) optic-natured (high frequency) mode procession for Ni and Co in the bilayer sample.

5.6 XMCD

To investigate the nature of the two resonant modes in greater detail, XFMR was subsequently performed. Prior to taking dynamic measurements it is necessary to determine the absorption edges of the elements within the sample to achieve the maximum dichroic signal for XFMR. The absorption edges used were the $L_{2,3}$ ($2p \rightarrow 3d$) for both Co (793, 778 eV) and Ni (870, 852 eV) [40]. Static XMCD spectra measured in transmission through the bilayer sample are displayed in Figure 5.11. Fe XMCD (710, 722 eV) [40] were also performed but had the disadvantage that Fe is present in both layers.

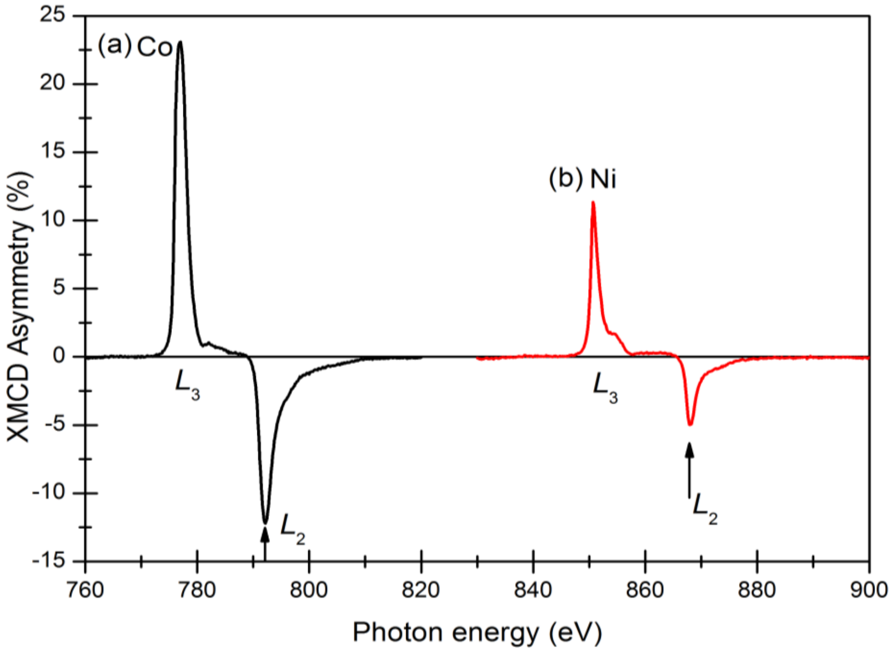

Figure 5.11: Typical static XMCD spectra for (a) cobalt and (b) nickel, Showing the $L_{2,3}$ absorption edges measured in transmission mode. The XFMR was measured at the L_2 edge indicated by the arrows.

The arrows in Figure 5.11 indicate the respective peak (L_2) to which the energy of the beamline were set. The L_2 peak was chosen as 'saturation effects' were observed on the Co L_3. The latter occurs as the soft x-rays (energy range ≈ 0-1400 eV) are attenuated exponentially as they pass through the bilayer film. The amount of Co material in the x-ray propagation direction corresponds to a length scale which is larger than the x-ray attenuation length. The XMCD spectra can be used to quantify the amount of magnetic moment along the beamline direction, thus allowing for both the collection of magnetic hysteresis loops and the determination of the cone angle of precession in magnetisation dynamics [19]. In practice, the cone angle precession only amounts to a few degrees, therefore the dynamic XMCD signal is much smaller than its static counterpart.

Figure 5.12 (a) shows the x-ray absorption spectra (XAS) hysteresis loops for both Ni and Co with the applied magnetic field parallel to the CPW direction and hence the easy axis of magnetisation of the CoFe. Both elements give rise to a simple hysteresis loop much as expected. This changes greatly as the applied field is rotated about the in-plane direction. Figure 5.12 (b) shows the hysteresis loops of the two elements with the applied field rotated in-plane 35° from the easy axis of magnetisation hence favouring the hard axis of the CoFe at 45°, this will be covered more in section 5.9 along with XFMR data. Figure 5.12(a) highlights the bilayer exchange-coupled together as the switching field of the two layers coincide. The hysteresis loops in Figure 5.12 (a) were only collected using positive circular light due to time constraints at the synchrotron.

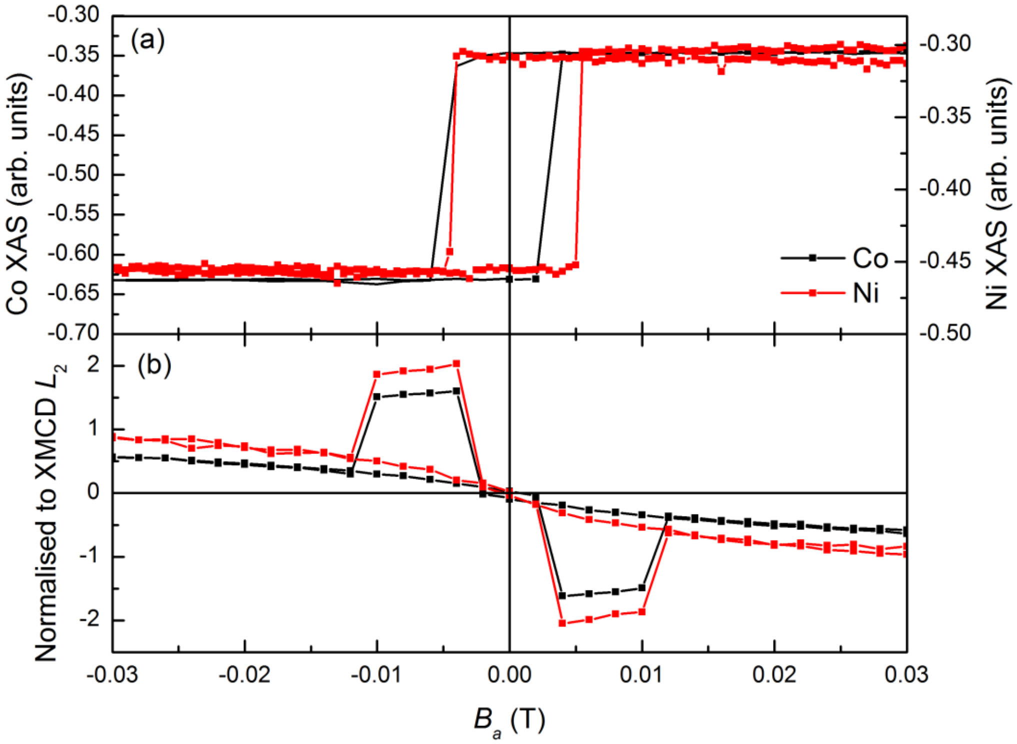

Figure 5.12: Hysteresis loops for (a) Ni and Co (positive circular x-rays) with the applied field along the easy axis and (b) Ni and Co XMCD normalised to the L_2 absorption edge with the applied field at 35° to the easy axis.

5.7 XFMR

Here the results of x-ray detected ferromagnetic resonance (XFMR) are presented and analysed. Fixing the microwave excitation to 8 GHz (any integer value of 500 MHz suitable for the sample) and the x-ray energy absorption edge for the element under investigation, then microwave delay to maximise the signal, the applied magnetic field was then swept to observe the resonance. The latter was observed using the luminescence emerging from the MgO substrate.

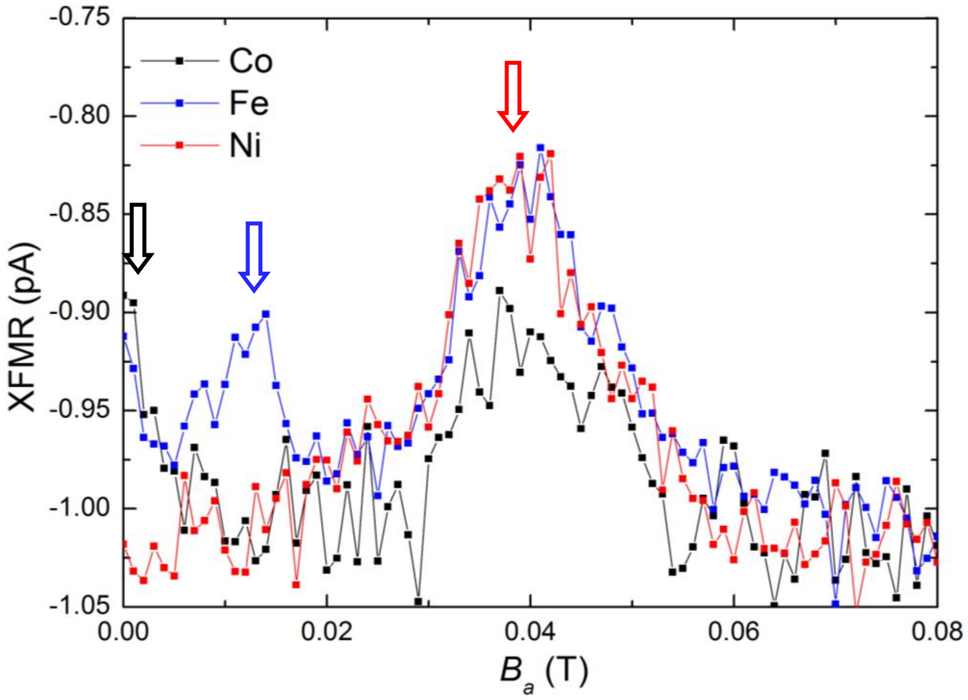

Figure 5.13: Photodiode current (XFMR signal) versus magnetic field at the Ni, Co and Fe edges with the excitation frequency set at 8 GHz and the microwave delay at 602 ps. Three resonant modes highlighted by arrows.

Figure 5.13 above shows the result of field sweeps obtained at the Ni, Co, and Fe edges. It indicates three resonances, one at 0.04 T, 0.012 T and the beginning of a third peak close to 0 T. The principle resonant mode is that of the low frequency acoustic type mode at 0.04 T (red arrow), although all the elements process at 0.04 T their amplitudes differ. The amplitudes can only be inferred from the lock-in current, as for a true value it must be normalised to the XMCD signal. It can be observed that the amplitude of the Co signal is weaker than that of either Ni of Fe. Contrastingly, the reverse occurs at the 0 T mode (black arrow) where the Co amplitude is dominant over that of the Ni. The reasons underlying this behaviour, are unveiled using delay scans (see section. 5.8 below). Note that the Fe-signal shown in Figure 5.13 is more difficult to interpret given that it originates from both layers in the sample. The third resonant mode at 0.012 T (blue arrow) is only present in the Fe which suggests that this mode is not coupled to either the CoFe or NiFe layers. We suggest therefore that this mode is an FMR signal arising from the thin Fe-seed layer underlying the bi-layer sample. This mode arises here and not in VNA-FMR because patterning the sample into a CPW increases the rf-field present at the Fe seed layer in the sample. The Fe in the seed layer is the only Fe present which is isolated by the Pt layer (30 nm) from both the NiFe and CoFe layers. A decision was therefore taken not to study the Fe-signal originating from the seed layer. Instead it is much more instructive to analyse the Ni and Co dynamic signals, given that they originate from the two separate layers in which we are interested.

5.8 Delay scans

Delay scans are useful in that they show the precession of the Co and Ni magnetic moments in a very direct way. Delay scans were obtained by fixing the excitation frequency and applied field to a given resonance peak, and subsequently using a delay line to advance/retard the microwave rf-field. The results shown in Fig 5.14 can be used to determine any phase differences between the Ni and Co signals originating from the two separate layers

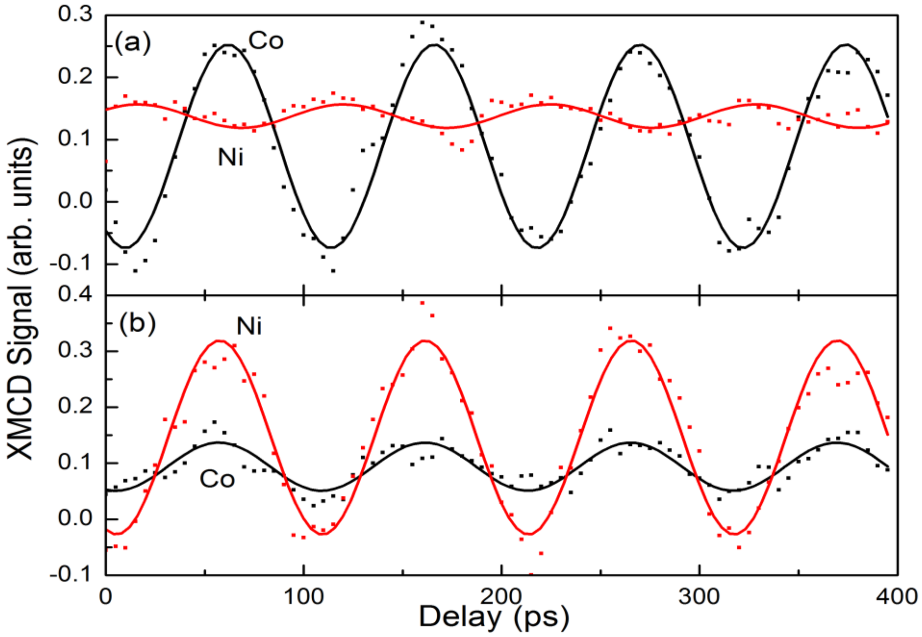

Figure 5.14: Delay scans showing the precession of the Co and Ni spins in (a) B_a set to the high frequency (optic) mode peak at 6.22 mT and (b) B_a set to the low frequency (acoustic) mode peak at 71 mT. Both scans were obtained at 9.5 GHz. For the optic (acoustic) mode the phase difference was found to be 166° (4°) respectively.

Figure 5.14 shows the delay scans for both Ni and Co at the low frequency (acoustic) mode and high frequency (optic) modes. Both measurements were performed at the higher frequency of 9.5 GHz in order to fully capture the high frequency optic mode. The solid lines represent sinusoidal fits to the data whereas scattered dots represent the experimental data averaged over several delay scans.

An increase in the excitation frequency can be problematic. The timing structure of the x-ray beam is set by the ‘bunches’ of x-rays each of which has a bunch width of 35 ps (corresponding to 14 GHz) with 2 ns between bunches [41]. It is the bunch width which determines the upper frequency limit available. In practice as the excitation frequency is increased, the cone angle of precession decreases. The statistics and therefore count time must be increased to obtain a reasonable signal/noise ratio.

Figure 5.14 indicates that the Co and Ni signals are essentially 180° out of phase for the high frequency (optical) mode while they are in phase for the low frequency (acoustic) mode. This justifies our choice of nomenclature for the two modes in question. More information can be obtained from the relative strengths of the Co and Ni XFMR signals. In the high frequency (Optic) mode the amplitude of the Co signal is much larger than that of the Ni. While in the low frequency (acoustic) mode the reverse is true. The high frequency mode appears to be driven primarily by the CoFe layer (Figure 5.14(a)) while the low frequency mode is dominated by the NiFe layer (Figure 5.14(b)). Similar effects have been observed in the amplitude of multiple resonant spin valves [42].

5.9 Field scan results

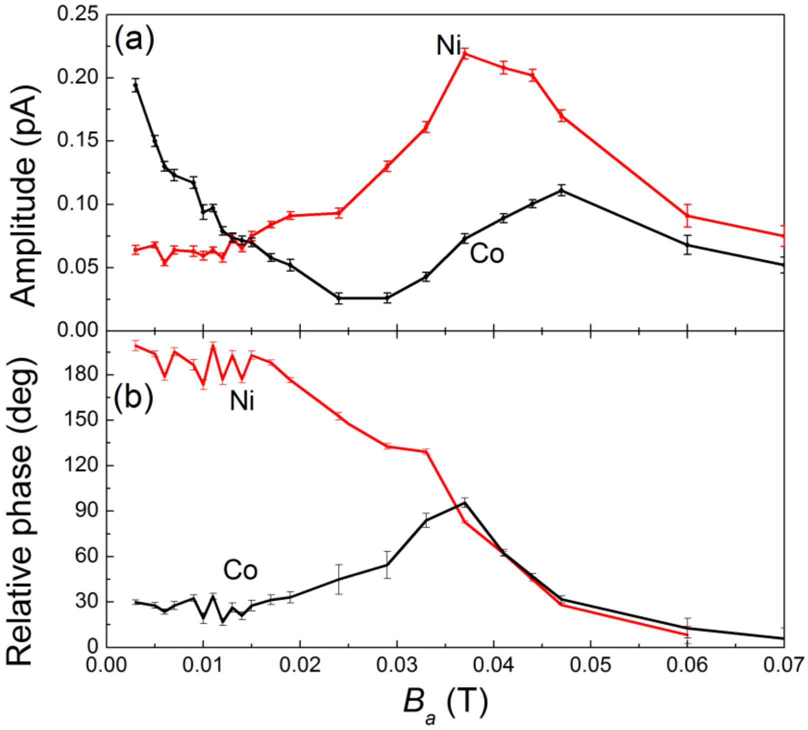

Figure 5.15: (a) Amplitudes of Ni and Co resonances derived from delay scans. (b) Phases of Ni and Co. Both (a) and (b) were obtained using an excitation frequency of 8 GHz.

Figure 5.15 (a) shows the amplitude of the Ni and Co resonances obtained at 8 GHz. A frequency of 9.5 GHz was not possible as the delay scans of Figure 5.14, off resonance the signal/noise was less pronounced as the cone angle of precession is smaller. The data was accumulated by performing numerous delay scans of the form shown in Figure 5.14. From this data an informative picture of the resonant modes was built up as a function of applied field (compare Figure 4 of Ref. [17] and Figure 3 of Ref. [19] respectively). Figure 5.15 shows a prominent low frequency (acoustic) mode at 0.04 T and the onset of the high frequency (optic) mode at low applied fields. It should be noted, as earlier, that the low frequency mode is predominantly Ni dominated, but induces precession in the Co layer. At resonance both the Ni and Co precess in phase. In contrast near $B_a \approx 0$ T, where the high frequency mode is dominant, the Ni and Co layers are essentially 180° out of phase. Further, at the low frequency resonance as the field is increased to 35 mT the low frequency mode, dominated by the Ni signal, becomes large. In addition the Ni changes from 180° to 0° [43] on passing through the low frequency resonance. The Co is coupled to the Ni, such the Co phase shows a peak at resonance which corresponds to 90°. Finally above the low frequency (acoustic) mode resonance (B_a>40 mT), the Ni and Co signals are in phase.

Further measurements were performed to investigate the anisotropy of the bilayer. The measurements were performed by applying the magnetic field in plane. Figure 5.16 shows the field sweeps obtained by VNA-FMR with the in-plane magnetic field rotated using the POMS system.

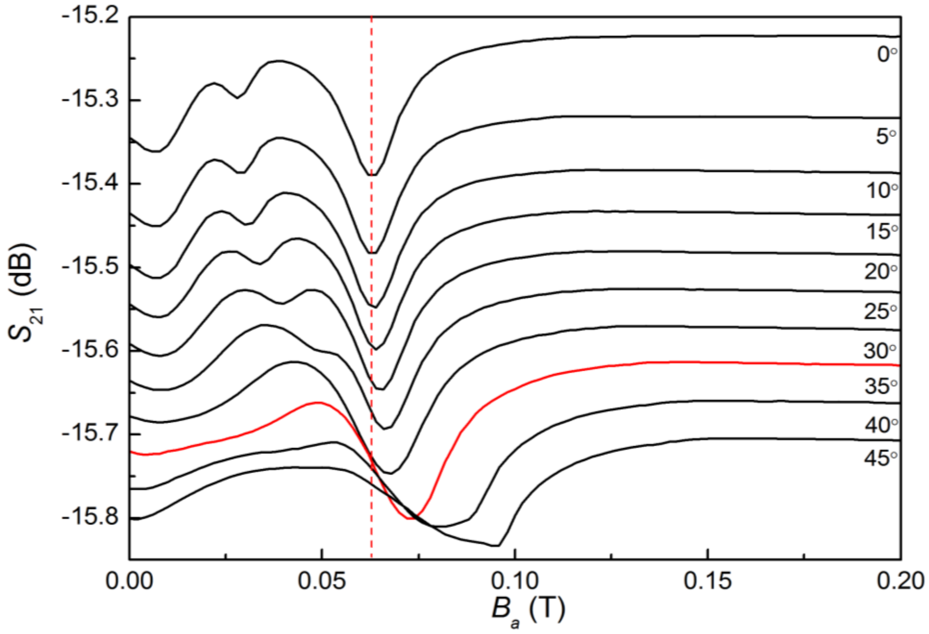

Figure 5.16: Field sweeps performed at 9.5 GHz *vs.* the in-plane magnetic field angle with respect to the CPW propagation direction. Red line represents the angle of magnetic field for the results presented in Figure 5.17.

The field sweeps demonstrate how the resonant modes shift and change as the magnetic field is rotated away from the easy axis. XFMR was subsequently performed with the magnetic field at 35° to the CPW direction. The more logical choice of 45° was not used as this angle did not show sufficient XFMR signal due to (*i*) the need to keep B_{rf} and B_a non-parallel to one another and (*ii*) the need to maximise the magnetisation parallel to the x-ray beam.

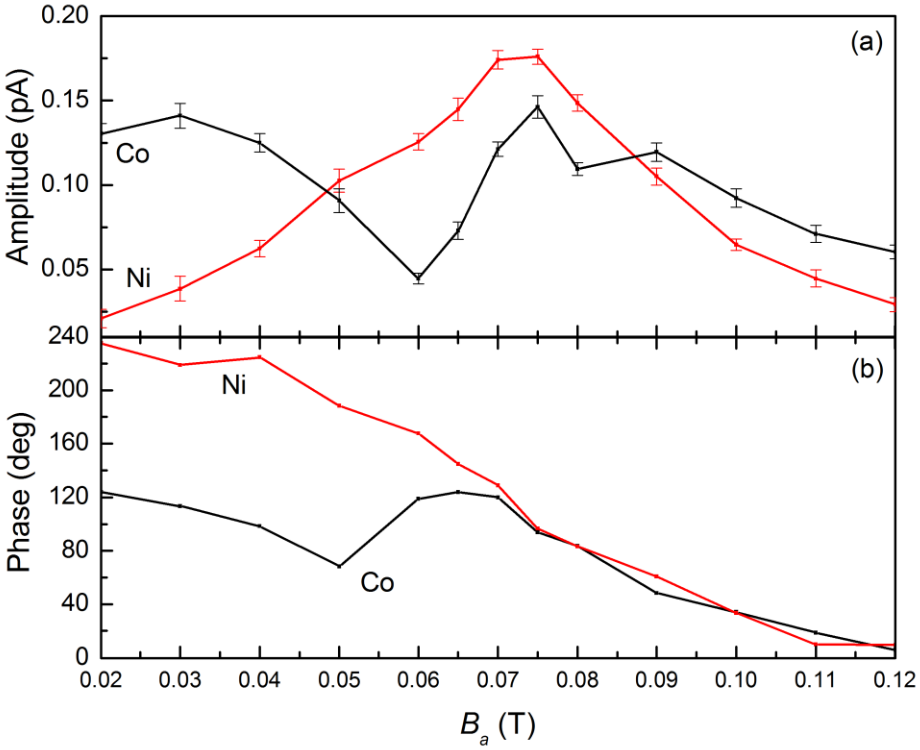

Figure 5.17: XFMR performed with the applied magnetic field at 35° to the easy axis of the CoFe showing (a) the amplitude of both Co and Ni and, (b) their relative phase. The excitation frequency was set to 9.5 GHz.

The results are summarised in Figure 5.17 which shows both the phase and amplitude of Ni and Co signals, with the applied magnetic field set at 35° to the easy axis (see section 5.2 Figure 5.6). The XMFR results at 35° shows similar features to that of Figure 5.15 in that the low frequency mode is dominated by the NiFe and the high frequency mode by CoFe, respectively. However there are significant changes which should be noted: (*i*) the resonant position of both the low and high frequency (acoustic and optic) modes have shifted to higher applied fields, and (*ii*) the phase of the Ni now no longer changes by 180° across the low frequency resonance but, in comparison the Co signal changes phase, this greatly differs from that of Figure 5.15(b) with the field at 0°. This occurs due to two competing effects. Firstly, the low frequency NiFe dominated mode now precesses at an angle which favours the CoFe anisotropy more strongly (Figure 5.6). Thus the Co will have a greater contribution to the resonance, as shown by the amplitude of the Ni and Co in Figure 5.17 approaching the same value. By contrast, in Figure 5.15 the difference in amplitudes is much greater. This is further highlighted in the extra magnetic switchings detailed in Figure 5.12 (b), when the applied field is applied at 35° from the easy axis of magnetisation.

5.10 Simulation

To simulate the bilayer dynamics a quasi-1D model of the bilayer system was investigated using the finite element micromagnetic simulation code Nmag [44, 45]. This code has previously been used to model the dynamics of exchange-spring coupled systems [46]. The Nmag simulation work was performed by Greg Ashton as his final year project for his undergraduate degree at the Physics and Astronomy department of the University of Southampton. The model takes the form of an 80 × 10 × 10 nm^3 cuboid crossing the CoFe/NiFe interface with the interface at the *yz* plane ($x = 0$), NiFe for $x < 0$ and CoFe for $x > 0$ (see Figure 5.18). As a consequence of using the quasi-1D model is that the demagnetisation field had to be ignored to avoid unrealistic alignment perpendicular to the bilayer film. The demagnetisation field is influenced by the geometry of the 1D cell. With the demagnetisation field removed, the moments align along the correct relaxed state expected for a quasi 1D cell in the centre of a film. This model should be viewed only as a qualitative theory giving detailed information about the structure of the various modes but not about the correct resonance conditions (*i.e.* frequency *vs.* B_a) because the demagnetisation field changes the internal field significantly.

Initially the quasi-1D model was prepared in an 'excited state' by applying a magnetic field B_a at a small angle $\theta = 0.6°$ away from the *y*-axis (*i.e.* small component along the *z*-axis). After the magnetisation has settled into this initial state reaching a local equilibrium configuration, the main dynamic simulation starts. At $t = 0$ the angle of the applied field was suddenly switched from 0.6° to 0.0°. Hence, for $t>0$, with B_a along the *y*-axis, the system subsequently allowed to relax to its minimum energy configuration. This modest change of the angle of the bias field excites the system sufficiently leading to spin waves propagating through the system. The magnetic response $M(x,y,z,t)$ for $t>0$ was determined using Nmag. A Fourier transform of the spatially resolved and spatially averaged magnetisation as a function of time was subsequently performed allowing both amplitude and phase of the modes to be determined. The spatially averaged analysis showed to have little dependence on *z* and *y* hence only the *x* dependence (normal to the film) is shown as per Figure 5.18.

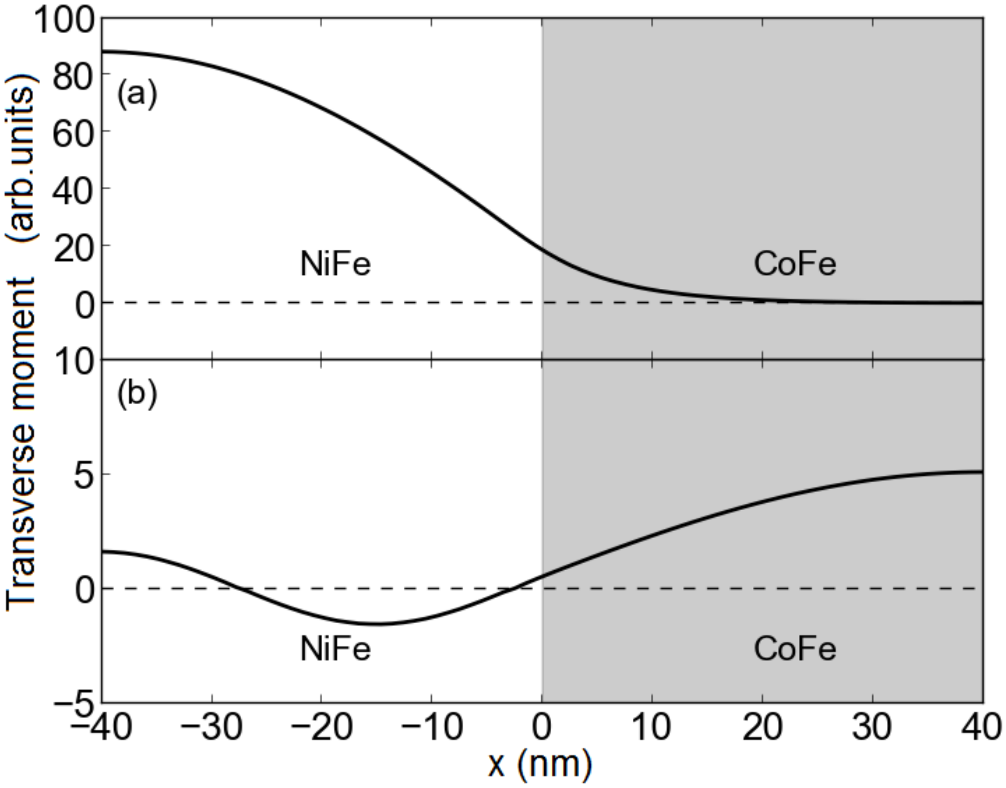

Figure 5.18: Simulated spatial form of the (a) low (acoustic) and (b) high (optic) frequency modes, across the interface of the bilayer ($x = 0$), showing the spatial structure of the excitations calculated using Nmag.

The transverse moment is described as the projection of the magnetisation along the z-axis. The advantage of the 1D model is that it provides a unique insight into the spatial form of each mode. Figure 5.18(a) shows that in the low frequency mode of the NiFe possesses larger amplitude over that of the CoFe. In contrast in the high frequency mode the CoFe amplitude dominates over that of the NiFe. In Figure 5.18(b) the NiFe amplitude varies from positive to negative leading to a degree of cancellation of the precession and therefore a low net XFMR signal which is in agreement with XFMR data is expected. The material parameters which were used, to produce Figure 5.18, were 13×10^{-12} Jm^{-1} and 20×10^{-12} Jm^{-1} for the exchange coupling of NiFe and CoFe respectively, with a saturation magnetisation of 8.6×10^{5} Am^{-1} and 1.88×10^{6} Am^{-1} for NiFe and CoFe [47].

Both the XFMR and VNA-FMR data indicate that the two resonances are dominated by the NiFe and CoFe layers respectively. The micromagnetic simulations show that each mode possesses a ‘near node’ near the interface (small precession amplitude). The Nmag simulations performed act as a good first order qualitative approximation to modelling the bilayer system. With these ideas in mind a simple approximate approach was used to fit the data shown in

Figure 5.3 and Figure 5.19 using the Kittel resonance equation, for the two layers taken separately. This was performed as the overall net response will occur as if the films are separate due to the thicknesses of the constituent films. The ratio between the thicknesses of the two films exchange-coupled together and that of the remaining material in a layer, separated by more than the exchange length against the other layer. Hence, to a first order approximation can be taken as two films independent of one another. The Kittel resonance condition for a thin film sample [48] is given by,

$$\omega_0 = \gamma\sqrt{(B_a + B_k)(B_a + B_k + \mu_0 M_0)}$$
$$\left(B_k = \frac{2K_1}{\mu_0 M_0}\right) \qquad (5.3)$$

Here B_k and K_1 are the anisotropy field and first order anisotropy constant respectively and M_0 is the saturation magnetisation. A least squares fit to the experimental data of Figure 5.3 was used to determine the parameters M_0, and B_k for each of the layers. For CoFe, M_0 was found to be 1.78×10^6 Am^{-1} and $K_1 = 46\times10^3$ Jm^{-3}. The values are in close agreement with values found in the literature [49, 50]. Contrastingly for NiFe the value of $M_0 = 9.06\times10^5$ Am^{-1} [51] was found to be in agreement with previous determinations while the value of K_1 (12×10^3 Jm^{-3}) is much higher than expected. A table showing a summary of the findings is shown below.

	CoFe	CoFe literature	NiFe	NiFe literature
Magnetisation $\times10^6$ (Am^{-1})	1.78	1.70	0.9	0.8
Anisotropy K_1 $\times10^3$ (Jm^{-3})	46.0	46.8	12.0	≈0

Table 5.1: Parameters calculated from least squares fit and literature for the saturation magnetisation and first order anisotropy constant.

We ascribe the NiFe anisotropy to a transfer of residual four-fold anisotropy from the CoFe to the NiFe layer via the strong exchange interaction across the interface. The results of the least squares fit to the experimental data are shown in Figure 5.19 (solid lines). For the NiFe resonance there is a slight deviation from the fit to experimental data at low fields, this is due to the presence of an exchange spring [52] in the NiFe layer pinned at the interface by the anisotropic CoFe. In summary the bilayer behaves to first order as two separate layers but with a transfer of the anisotropy from the CoFe to the NiFe layer. This is reflected in the linewith of the modes observed. The modes predicted by micromagnetic simulations and by fitting the Kittel equation (Eq. 5.3) are in reasonable agreement with the experimental data of Figure 5.3 and Figure 5.15 collected both from VNA-FMR and XFMR.

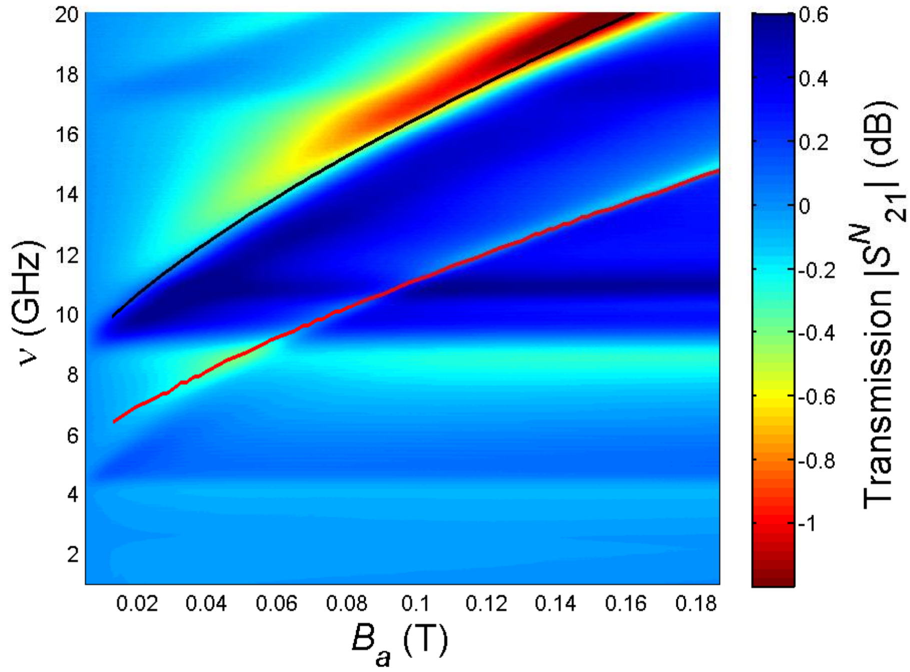

Figure 5.19: Normalised $\left|S_{21}^{N}\right|$ ν-B_a map of bilayer sample. Included as solid lines, are the results of a least-squares fit to the Kittel resonance equation for the two layers taken separately.

Figure 5.19 above shows a ν-B_a map of the bilayer obtained by VNA-FMR with the least-squares fit to the Kittel resonance overlaid. It shows good agreement between them except at low applied fields where the exchange coupling occurs (Figure 5.5).

The Nmag simulations also provide qualitative phase information confirming the behavior of the observed modes (see Figure 5.15). For the low frequency (acoustic) NiFe mode on passing through resonance, the phase flips by ~180° in agreement with experimental results. In contrast, the non-resonant CoFe layer does not show phase reversal on passing through the NiFe resonance. This result is consistent with the XFMR data. In summary the quasi-1D model can be used as a good, first approach to study the dynamics of the bilayer system. However, a study of improved micromagnetic modeling, which includes the demagnetisation effect is now underway.

5.11 Conclusion

Magnetisation dynamics have been investigated by designing and building a VNA-FMR spectroscopy rig. The properties of various magnetic films were investigated, most notably the different modes of a transition metal bilayer.

Generally, for multilayer films with multiple resonances, the data is hard to interpret. The methods employed in observing the FMR are bulk and therefore cannot differentiate between the layers and hence resonant modes of the sample. By contrast, XFMR then becomes the experimental method of choice [16-18].

Synchrotron-based XFMR experiments combined with micromagnetic modeling give a detailed understanding of the magnetisation dynamics of a NiFe/CoFe bilayer film which is coupled by strong exchange. In particular XFMR allows the two layers to be probed individually yielding details of the nature and origin of the observed resonant modes. The low frequency high field mode can be described as an ‘acoustic-natured mode’ with all spins in-phase. For this mode the amplitude is a maximum in the NiFe film but decays as it penetrates into the CoFe layer. In contrast the low field mode is an ‘optical-natured mode’ with the spins in the two layers in question almost 180^o out of phase with each other. In this mode the amplitude is a maximum in the CoFe film as revealed by XFMR results. Calculations using the simple Kittel equation for FMR indicate that the two layers comprising the NiFe/CoFe bilayer film act almost independently of each other. It is also evident that the anisotropy of the CoFe film has been ‘transferred’ to the softer NiFe film via the strong exchange coupling across the bilayer interface.

References

1. D. Suess, T. Schrefl, R. Dittrich, M. Kirschner, F. Dorfbauer, G. Hrkac, and J. Fidler, *J. Mag. Mag. Mater.* **290,** 551. (2005).
2. D. Suess, T. Schrefl, S. Fahler, M. Kirschner, G. Hrkac, F. Dorfbauer, and J. Fidler, *Appl. Phys. Lett.* **87,** 12504. (2005).
3. R. H. Victora, and X. Shen, *IEEE Trans. Mag.* **41,** 537. (2005).
4. M. R. J. Gibbs, *J. Magn. Mag. Mater.* **290,** 1298. (2005).
5. A. Ludwig, and E. Quandt, *J. Appl. Phys.* **87,** 4691. (2000).
6. C. T. Pan, and S. C. Shen, *J. Mag. Mag. Mater.* **285,** 422. (2005).
7. B. K. Kuanr, V. Veerakumar, R. Marson, S. R. Mishra, R. E. Camley, and Z. Celinski, *Appl. Phys. Lett.* **94,** 202505. (2009).
8. Y. P. Chen, X. Fan, Q. Lu, and J. Q. Xiao, *J. Appl. Phys.* **110,** 053905. (2011).
9. T. Yukawa, and K. Abe, *J. Appl. Phys.* **45,** 3146. (1974).
10. L. R. Walker, *J. Appl. Phys.* **29,** 318. (1958).
11. R. W. Damon, and J. R. Eshback, *J. Phys. Chem. Solids.* **19,** 308. (1961).
12. J. F. Dillon, Jr. *J. Appl. Phys.* **31,** 1605. (1960).
13. C. Kittel, "*Introduction To Solid State Physics, Eighth Edition,"* (Wiley and Sons, Inc. 2005).
14. M. Kostylev, A. A. Stashkevich, A. O. Adeyeye, C. Shakespeare, N. Kostylev, N. Ross, K. Kennewell, R. Magaraggia, Y. Roussigne, and R. L. Stamps, *J. Appl. Phys.* **108,** 103914. (2010).
15. D. C. Crew, K. J. Kennewell, M. J. Lwin, R. C. Woodward, S. Prasad, and R. L. Stamps, *J. Appl. Phys.* **97,** 10A707. (2005).
16. T. Martin, G. Woltersdorf, C. Stamm, H. A. Durr, R. Mattheis, C. H. Back, and G. Bayreuther, *J. Appl. Phys.* **103,** 07B112. (2008).
17. D. A. Arena, Y. Ding, E. Vescovo, S. Zohar, Y. Guan, and W. E. Bailey, *Rev. Sci. Instrum.* **80,** 083903. (2009).
18. J.F.Cochran, and B. Heinrich, *IEEE Trans. Mag.* **16,** 660 (1980).
19. D. A. Arena, E. Vescovo, C.-C. Kao, Y. Guan, and W. E. Bailey, *J. Appl. Phys.* **101,** 09C109. (2007).
20. R. C. O'Handley, *"Modern Magnetic Materials; Principles and Applications,"* Wiley Interscience (Wiley and Sons, Inc. 2000).
21. R. Skomski and J. M. D. Coey, *IEEE Trans. Mag.* **29,** 2860. (1993).
22. R. Skomski and J. M. D. Coey, *Phys. Rev. B.* **48,** 15812. (1993).
23. W. H. Rippard, M. R. Pufall, M. L. Schneider, K. Garello, and S. E. Russek, *J. Appl. Phys.* **103,** 053914. (2008).
24. J. M. Shaw, H. T. Nembach, T. J. Silva, *Appl. Phys. Lett.* **99,** 012503. (2011).

25. P. J. Metaxas, R. L. Stamps, J. -P. Jamet, J. Ferre, V. Baltz, B. Rodmacq, and P. Politi, *Phys. Rev. Lett.* **104,** 237206. (2010).

26. R. Magaraggia, K. Kennewell, M. Kostylev, R. L. Stamps, M. Ali, D. Greig, B. J. Hickey, and C. H. Marrows, *Phys. Rev. B.* **83,** 054405. (2011).

27. J. F. Cochran, B. Heinrich, and A. S. Arrott, *Phys. Rev. B.* **34,** 7788. (1986).

28. Z. Zhang, L. Zhou, P. E. Wigen and K. Ounadjela, *Phys. Rev. B.* **50,** 6094. (1994).

29. M. K. Marcham, P. S. Keatley, A. Neudert, R. J. Hicken, S. A. Cavill, L. R. Shelford, G. van der Laan, N. D. Telling, J. R. Childress, J. A. Katine, P. Shafer, and E. Arenholz, *J. Appl. Phys.* **109,** 07D353. (2011).

30. M. K. Marcham, W. Yu, P. S. Keatley, L. R. Shelford, P. Shafer, S. A. Cavill, H. Qing, A. Neudert, J. R. Childress, J. A. Katine, E. Arenholz, N. D. Telling, G. van der Laan, and R. J. Hicken, *Appl. Phys. Lett.* **102,** 062418. (2013).

31. J. Goulon, A. Rogalev, F. Willhelm, G. Goujon, C. Brouder, A. Yaresko, J. B. Youssef, and M.V. Indenbom, *J. Magn. Mag. Mater.* **322,** 2308. (2010).

32 G. Boero, S. Mouaziz, S. Rusponi, P. Bencok, F. Nolting, S. Stepanow and P. Gambardella, *New. J. Phys.* **10,** 013011. (2008).

33 Y. Guan, W. E. Bailey, C. -C. Kao, E. Vescovo, and D. A. Arena, *J. Appl. Phys.* **99,** 08J305. (2006).

34. G. van der Laan, and B. T. Thole, *Phys. Rev. B.* **43,** 13401. (1991).

35. J. Lindner, and K. Baberschke, *J. Phys.: Condens. Matter.* **15,** R193. (2003).

36. A. M. Kaiser, C. Schoppner, F. M. Romer, C. Hassel, C. Wiemann, S. Cramm, F. Nickel, P. Grychtol, C. Tieg, J. Lindner, C. M. Schneider, *Phys. Rev. B.* **84,** 134406. (2011).

37. http://www.awrcorp.com/

38. J. M. L. Beaujour, A. D. Kent, D. W. Abraham, and J. Z. Sun, *J. Appl. Phys.* **103,** 07B519. (2008).

39. G. B. G. Stenning, G. J. Bowden, L. C. Maple, S. A. Gregory, A. Sposito, R. W. Eason, N. I. Zheludev, and P. A. J. de Groot, *Opt. Express.* **21,** 1456. (2013).

40. A. Thompson, D. Attwood, E. Gullikson, M. Howells, K. –J. Kim, J. Kortright, I. Lindau, Y. Liu, P. Pianetta, A. Robinson, J. Scofield, J. Underwood, G. Williams, H. Winick, "*X-ray data booklet*," Lawrence Berkeley National Laboratory (Third edition, 2009).

41. C. A. Thomas, G. Rehm, H. L. Owen, N. G. Wyles, S. W. Botchway, V. Schlott, and M. Wahl, *Nucl. Instr. and Meth. A.* **566,** 762. (2006)

42. K. Lenz, T. Tolinski, E. Kosubek, and K. Baberschke, *Phys. Rev. B.* **69,** 144422. (2004).

43. D. A. Arena, E. Vescovo, C. -C. Kao, Y. Guan, and W. E. Bailey, *Phys. Rev. B.* 74, 064409. (2006).

44. http://nmag.soton.ac.uk/

45. T. Fischbacher, M. Franchin, G. Bordignon, and H. Fangoh, *IEEE. Trans Magn.* **43,** 2896. (2007).

46. M. Franchin, J. P. Zimmermann, T. Fischbacher, G. Bordignon, P. A. J. de Groot, and H. Fangohr, *IEEE. Trans. Magn.* **43,** 2887. (2007).

47. G. Ashton, *MPhys Degree*, University of Southampton. (2012).

48. C. Kittel, *Phys. Rev.* **73,** 155161. (1948).

49. T. Uemura, Y. Imai, M. Harada, K. Matsuda, and M. Yamamoto, *Appl. Phys. Lett.* **94,** 182502. (2009).

50. M. Munakata, S. Aoqui, and M. Yagi, *IEEE. Trans. Magn.* **41,** 3262. (2005).

51. M. Madami, S. Tacchi, G. Gubbiotti, V. Bonanni, D. Bisero, P. Vavassori, A. O. Adeyeye, S. Goolaup, N. Singh, and C. Spezzani, *J. Appl. Phys.* **105,** 07C115. (2009).

52. G. B. G. Stenning, G. J. Bowden, L. R. Shelford, S. A. Gregory, P. Bencok, P. Steadman, A. N. Dobrynin, T. Hesjedal, G. van der Laan, P. A. J. de Groot, *Phys. Rev. B.* **86,** 174420. (2012).

6. Magnetic control of metamaterials

In this chapter some novel features in the emerging science of metamaterials are presented and discussed. In general, metamaterials are made up of metallic resonators (metamolecules) which possess desirable properties over a limited frequency range. We demonstrate that by coupling a split ring resonator to a magnetic material such as yttrium iron garnet (YIG), it is possible to 'tune' the frequency of the composite metamaterial and the modulation depth using an applied magnetic field. In particular we detail the magnetisation dynamics of the hybrid system using a vector network analyser (VNA).

6.1 YIG FMR

A magnetic garnet such as yttrium iron garnet (YIG) is a ferrimagnet with a strong magnetic moment, which give a saturation magnetisation of 139.26×10^{3} A/m [1], and more importantly a very narrow linewidth. As a result YIG is often used in microwave applications. Before any metamaterials studies can begin we must first optimise and understand the magnetisation dynamics of the YIG alone before incorporating the more complex system of the metamaterial. The YIG film used was grown by PLD (see Ch. 3, section 3.3). Feedback was provided to the grower to obtain an optimised growth method which gives a narrow FMR linewidth. The YIG film is grown on a substrate of gadolinium gallium garnet (GGG) providing a good lattice match. Literature states that a sphere of bulk YIG material yields linewidths as narrow as 0.02 mT [2]. For our PLD-grown films the FMR linewidth of 1.8 mT was achieved. This is an increased value in comparison to the bulk sphere and this can be due partly to the demagnetising effects based on the film shape as mentioned earlier in Ch. 2 as well as the inhomogeneous rf laterally across the CPW.

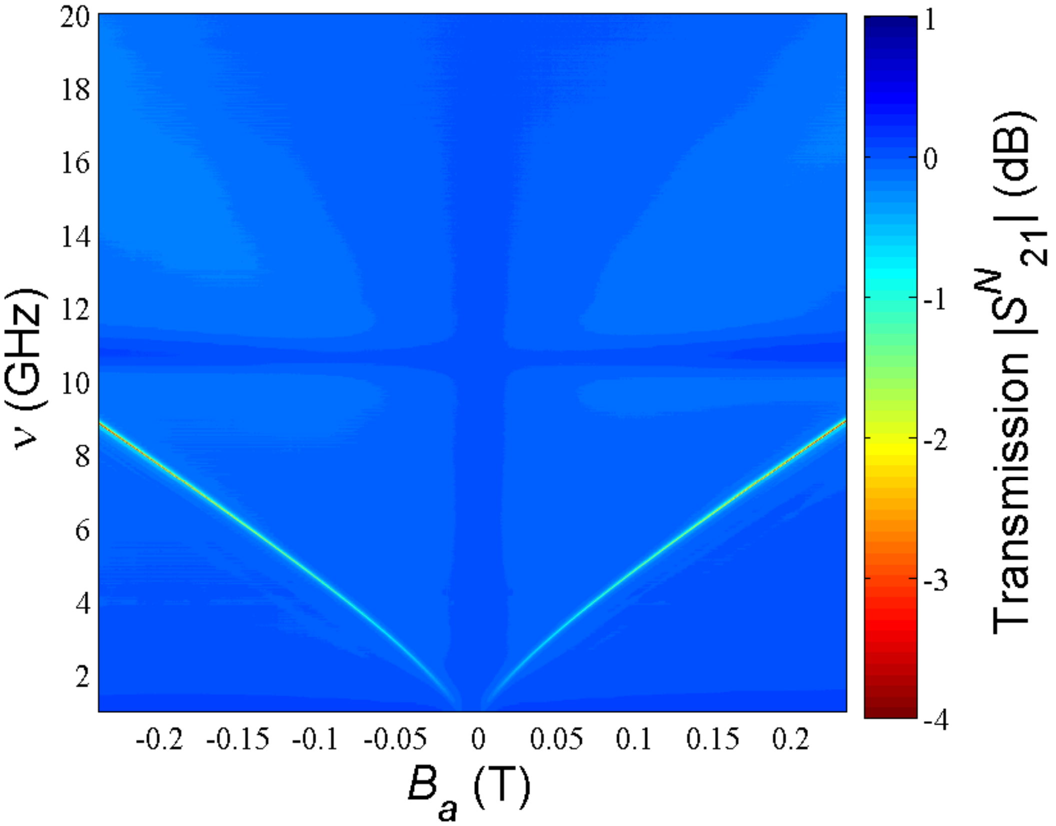

Figure 6.1: ν-B_a map of 2.4 µm YIG on GGG.

Figure 6.1 clearly shows a narrow resonance linewidth with a width of 1.8 mT. A strong absorption of the FMR can be observed also in Figure 6.2.

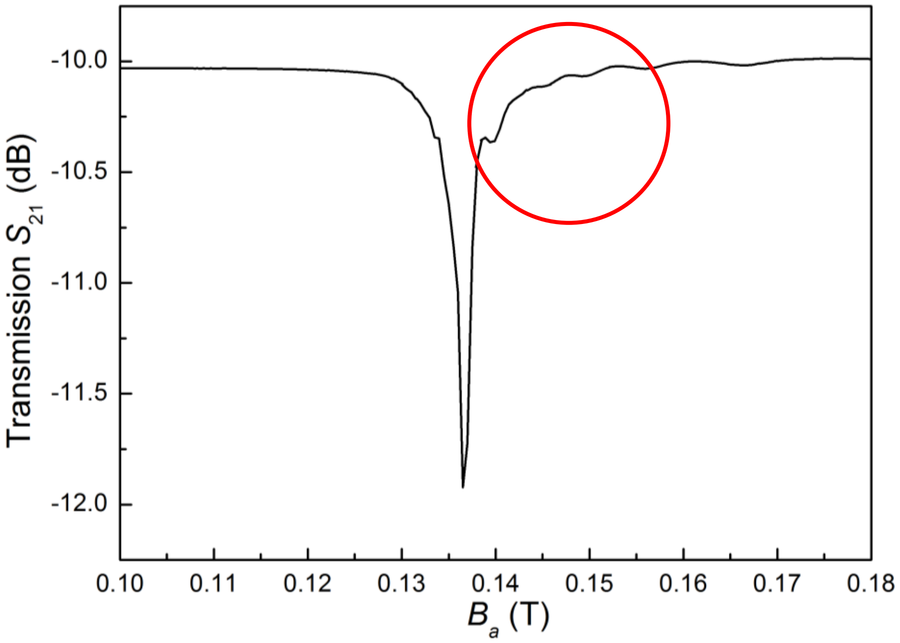

Figure 6.2: Field sweep at a fixed frequency of 6 GHz.

Figure 6.2 shows the FMR linewidth of the same YIG film as that shown in Figure 6.1. The excitation frequency used for the field sweep was set at 6 GHz. YIG possessed a low damping parameter (α), a high saturation magnetisation (M_s) and approximately no anisotropy. The linewidth observed in comparison to the bulk linewidth associated with that of a high quality YIG sphere is 100 times broader. One of the reasons is due to magnetostatic modes being set up in the sample [3, 4]. These are dependent upon the geometry between the rf field and the $\overline{H}_{eff}$. They can be observed in Figure 6.2 as the small oscillations on the high field side of the main FMR peak (highlighted in the circle). There is reason to believe that these modes can hide the true intrinsic linewidth of the YIG. More detail and analysis of the YIG modes will be covered later in this Ch. where YIG is used to couple to a metamaterial.

6.2 Magnetic metamaterial

The subject now known as metamaterials is a developing area of physics which offers prospects for new science and applications. Metamaterials are man-made patterned structures which exhibit unusual electromagnetic properties. In recent years this subject has developed into a rich research field motivated by the promise of both ground-breaking science and device applications. Metamaterials can be engineered to exhibit unusual electromagnetic properties such as negative permeability (μ) and/or negative permittivity (ε). Such materials can possess a negative index of refraction (n) [5] and therefore enable 'cloaking' at microwave frequencies [6]. In general such desirable properties are achieved at frequencies close to the resonance of the periodic metamolecules that comprise the metamaterial. To date research has concentrated primarily on manipulating relatively simple materials such as ohmic metals and low-loss dielectrics. The most commonly employed metamolecule is the split ring resonator (SRR), which has been exclusively studied ever since its original proposal by Pendry *et al* [7]. The resonant frequency of the individual metamolecule (ω_{mm}) is determined by the capacitance (C) and the inductance (L) of the SRRs' geometry:

$$\omega_{mm} = \frac{1}{\sqrt{LC}} \qquad (6.1)$$

The SRR dimensions are typically 10% of the incident wavelength used to excite the structure. Such SRR systems are often restricted to a narrow frequency band due to the resonant character of the individual metamolecule. To bridge this gap attention has turned to tunable metamaterials. Composite structures involving both a high-conductivity SRR and an active magnetic component were investigated in this thesis. In particular we have used a thin film of yttrium iron garnet (YIG) coupled to a SRR, hence creating a hybrid structure. There are two different resonances that need to be considered (*i*) that of the SRR and (*ii*) that of the YIG. Since the latter is field-dependent, tunability of the composite structure can be achieved by applying a magnetic field. Tunability of magnetic resonances in the microwave regime also offers a powerful means to realize controllable, loss-compensating, multi-frequency antennas [8].

Kang *et al.* [9] were the first to report a magnetically tuneable metamaterial, made up from an SRR array and small rods of YIG all placed in an X-band waveguide. The resulting complex resonances were subsequently interpreted by Gollub *et al.* [10]. Our research centres on the interaction between a thin (2.4 µm) YIG film and a single SRR excited by a broadband coplanar waveguide (CPW). The results are shown in section 8.3, and are interpreted using (*i*) the EM field simulation package COMSOL performed by Lewis Maple for the degree of Doctor of Philosophy and (*ii*) a simple two-state model for a SRR and YIG film respectively [11, 12]. The interaction between the SRR and the YIG provides a fertile breeding ground for the excitation of spin-waves, magnetostatic surface wave (MSSW) and backwards volume magnetostatic wave (BVMSW) [13]. It will be demonstrated that both the MSSW and BVMSW can be incorporated into the simple two-state model.

6.3 Experimental details

Martin *et al.* [14] and Falcone *et al.* [15] have shown that resonances in SRR systems can be studied and exploited in a coplanar arrangement in close proximity to a broadband coplanar waveguide (CPW). Such an arrangement presents increased opportunities for applications as a broadband tunable device. It is further found that SRRs placed on the reverse side of the CPW substrate couple effectively to the CPW resulting in lower transmission losses, while still revealing strong metamaterial resonances [16]. Schematic diagrams, showing the physical arrangement of the CPW, SRRs, and the YIG film used in this work can be seen in Figure 6.3. This arrangement possesses extensive advantages. The planar geometry is suited to applications and only small quantities of YIG are required.

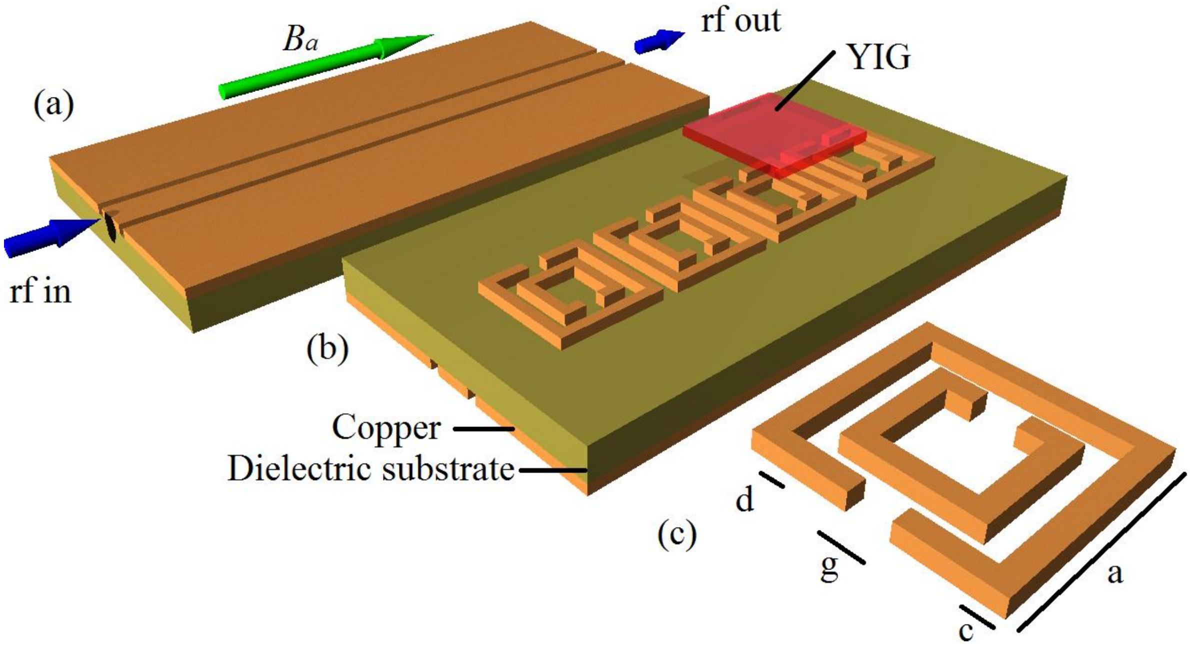

Figure 6.3: A Schematic view of (a) Top view of the CPW. (b) SRRs (metamaterial) located on the underside of the CPW substrate. The YIG film is placed directly on top of one SRR and (c) single split ring resonator (SRR). Dimensions of a = 3.93 mm, c = 0.375 mm, d = 0.45 mm, g = 0.69 mm. Field direction as shown by B_a.

The experimental arrangement used is the same as that described in section. 3.5; however the design of the CPW is different. The CPW has a signal line width and gap size of 1.1 mm and 200 μm, respectively, as shown in Figure 6.3(a) which allows the CPW to be a broadband frequency device in the range 1-20 GHz with the required 50 Ω impedance. The SRR is fabricated on the underside of the CPW directly underneath one of the gaps of the CPW in order to maximise rf-coupling [15]. The CPW itself was fabricated using a simple mask/photo-etching technique. A 70 μm copper layer on both sides of a 0.7 mm thick dielectric sheet was used as the substrate (FR4, ε_r = 4.5). The SRR, fabricated on the reverse of the CPW with dimensions specified in Figure 8.1(c) is similar to the design by Shelby *et al* [17]. The dimensions of the SRR have been modified to produce frequencies close to the ferrimagnetic resonance (FMR) [18] of the YIG in the available magnetic field range 0-0.5 T.

The YIG film was grown on a single-crystal yttrium aluminium garnet (YAG) (100 oriented) substrate by pulsed laser deposition using a KrF excimer laser operating at 248 nm [19-21]. YIG was used as the magnetic component in this experiment because (*i*) it possesses a strong, narrow FMR resonance, (*ii*) it is characterised by negative permeability on resonance [22] and (*iii*) there are no complications from eddy current losses. The YIG film was placed directly on top of the

SRR ('flip-chip' method) [23] allowing strong coupling to the CPW and therefore good microwave excitation. The VNA allows for collection of the S-matrix parameters including the transmission coefficient S_{21}. The latter describes the transmission properties of the CPW now loaded with the SRR and the YIG film.

6.4. Results

The results presented here are for a single SRR as this avoids the complex effects reported by Kang *et al*. [9] arising from cells at the boundaries of the array. The S_{21} transmission was measured in a frequency *vs*. field map (ν-B_a), in the range 1-20 GHz and 0-0.5 T as in Figure 8.2. In Figure 8.2 the colour at a given point in the map represents the magnitude of S_{21}. In addition it is noted that the S_{21} map plots shown were normalized by subtracting the S_{21} transmission obtained in a small (approximately zero) magnetic field (B_a =0.001 T) from every subsequent frequency sweep. It gives a final value of $|S^N_{21}|$, leaving only field dependent features in the resulting plot. Such maps clearly show (*i*) the individual SRR and YIG resonances and (*ii*) strong anti-crossing behaviour when the two resonances coincide. SRRs of various sizes were used. The size of the SRR scales inversely with the frequency thereof (Eq. 6.1). We focus only on one particular size for this investigation into tenability of metamaterials.

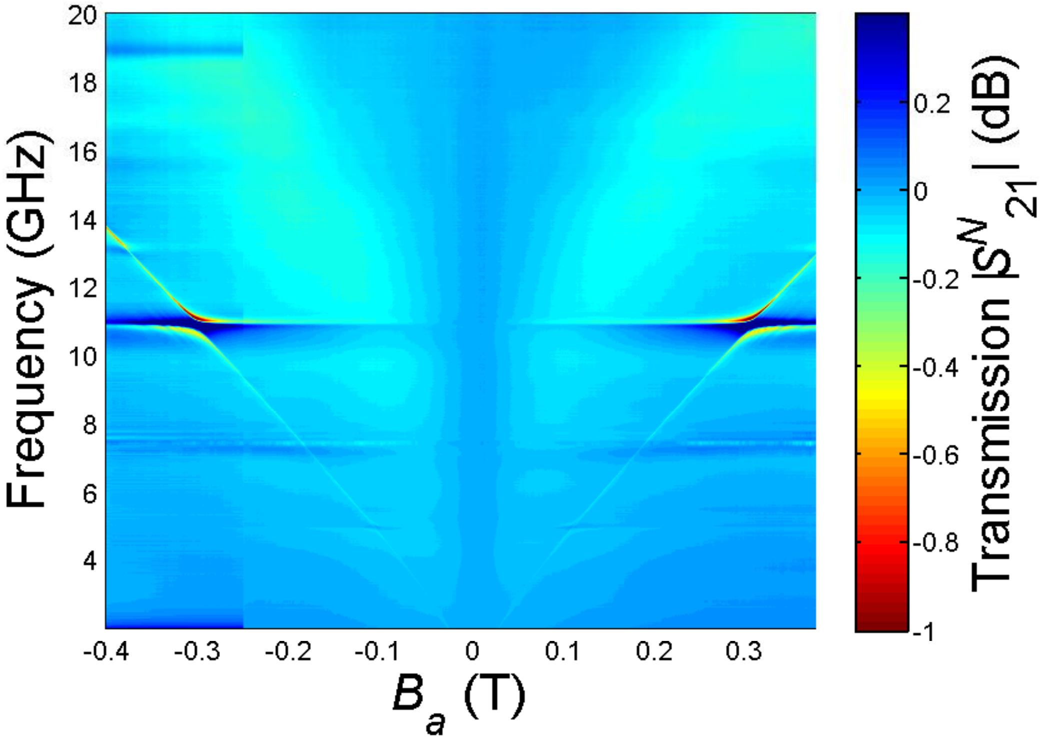

Figure 6.4: Normalized $\left|S^N_{21}\right|$ (ν-B_a) map of a YIG film coupled to a SRR. The transmission colour-bar on the right represents transmission (positive values/blue) and absorption (negative values/red).

The normalized $\left|S_{21}^{N}\right|$ map of the CPW/SRR/YIG composite system in Figure 6.4 demonstrates a single SRR coupled to a YIG film excited via the CPW. The ν-B_a map is symmetrical about $B_a = 0$ as the YIG is isotropic. The absorption that appears as a diagonal line from $B_a = 0$ T, $\nu = 2$ GHz is the expected YIG FMR. This is the acoustic mode whose frequency *vs.* field behaviour follows the usual Kittel resonance equation for a thin film magnetised in-plane [2]. Observe that the SRR resonance appears as a horizontal line at 10.9 GHz. At that point where the YIG and SRR resonances are expected to cross strong anti-crossing behaviour occurs. As the YIG is isotropic we have only shown the positive field section of the S_{21} map in Figure 6.5.

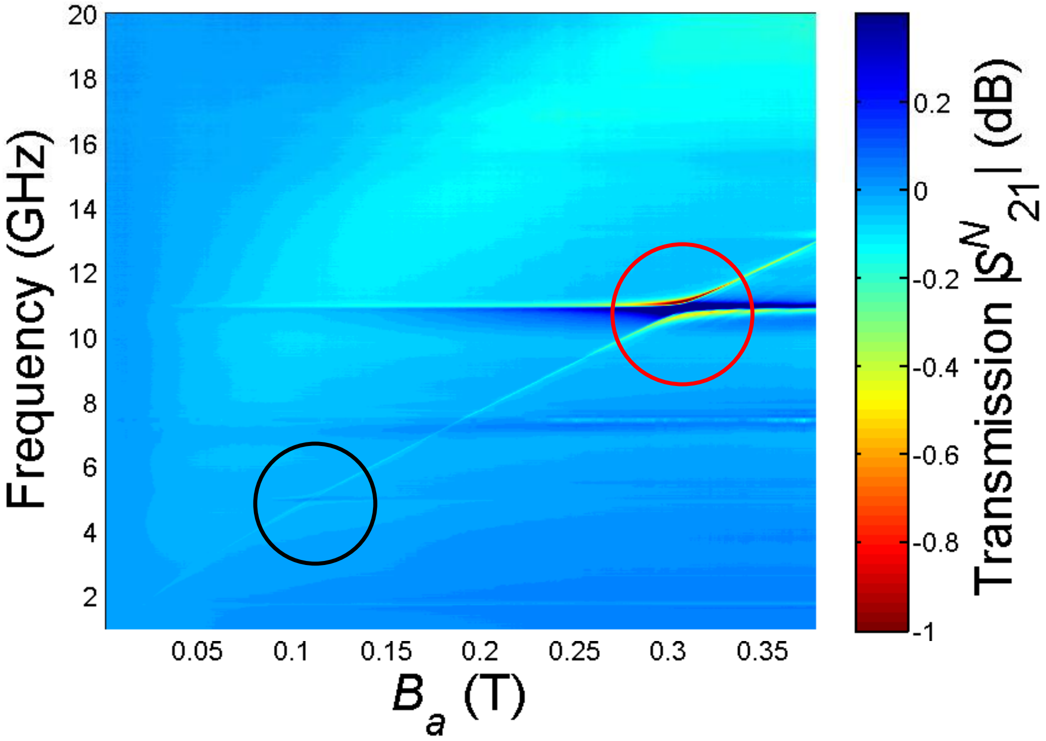

Figure 6.5: (ν-B_a) map of hybridised interaction showing all anti-crossings present. Red (black) circle represent the electric (magnetic) resonance mode of the SRR respectively.

Figure 6.5 shows that for the system described above there are two different types of hybridised resonances. The two anti-crossings in question are highlighted by the circles in Figure 6.5. Anti-crossings are found at frequencies of 5 GHz (black) and 10.9 GHz (red). The two anti-crossings arise from the different current excitations (magnetic and electric) of the SRR which will be covered in more detail in the next section. The main focus of this thesis will be upon the strongest 10.9 GHz anti-crossing. Figure 6.6 shows a reduced frequency (8-13 GHz) and magnetic field range (0.22-0.38 T) ν-B_a map of the second hybridised resonance shown in Figure 6.5 (red circle). It will be noted that there is a reduction in the microwave losses on resonance at an applied field of $B_a = 0.3$ T. This is illustrated both in Figure 6.6 and Figure 6.7 at the centre of the anti-crossing. Above and below the anti-crossing (black and blue curves respectively in Figure 6.7) there are absorption lines (negative) associated with the field-dependent YIG FMR while exactly at the centre of the anti-crossing there is a large modulation of the transmission amounting to 1.6 dB (peak). This is indicative of an effective negative index of refraction as detailed by He *et al.* [24] using the experimental S-parameter retrieval technique [25, 26]. It is evident that satellites on the high field side of the transmission peak are observed. These features are due to the excitation of BVMSWs as discussed in [3-4, 13, 27] and in greater detail in the next section.

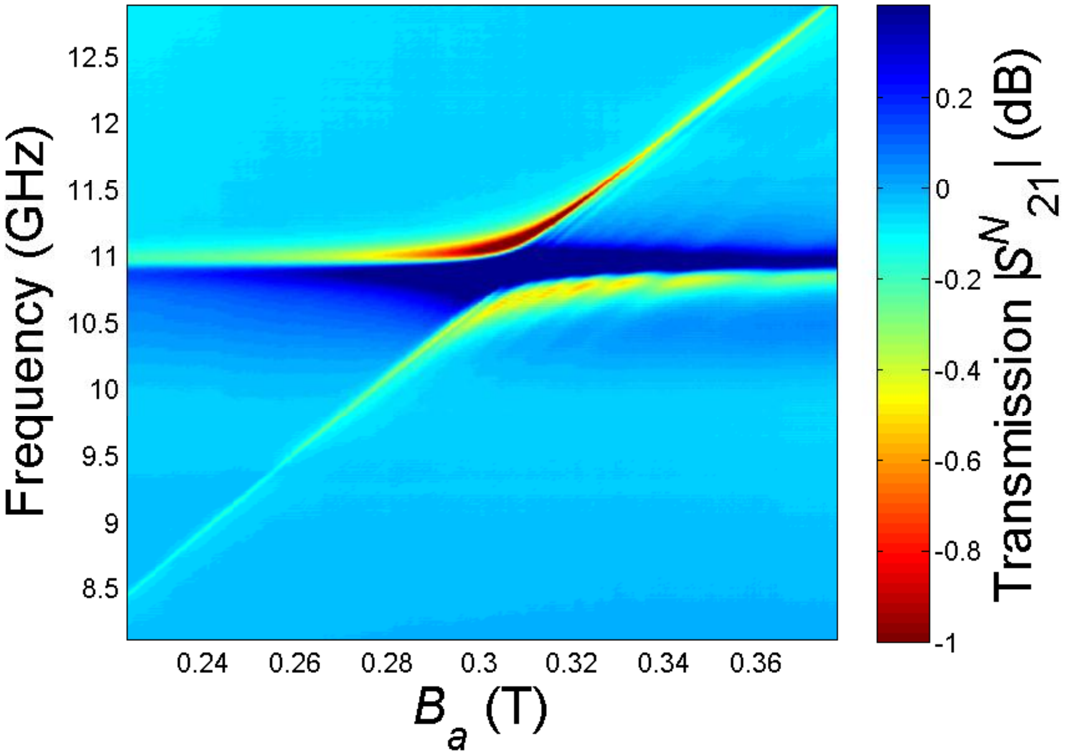

Figure 6.6: (ν-B_a) map of the YIG-SRR anti-crossing mode.

The anti-crossings depicted in Figure 6.5 are similar to those described by Gollub *et al.*, who gave a theoretical interpretation of the interaction of YIG rods with SRRs. Our study shows good agreement with their findings for the YIG/SRR anti-crossing. The low frequency trough in Figure 6.7 (trace $B_a = 0.28$ T) is that of the FMR resonance whereas the high frequency peak is associated with the symmetric electric-dipole resonance of the SRR (see Figure 6.7)).

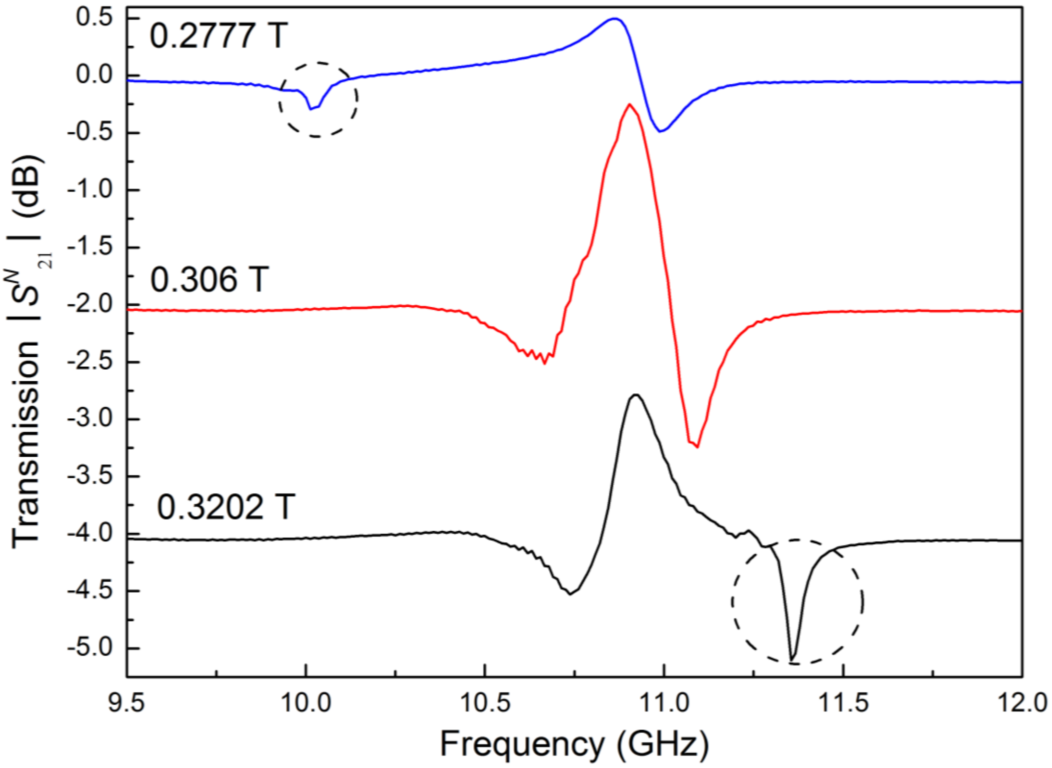

Figure 6.7: Normalised transmission S^N_{21} *vs.* frequency (v) at three fixed fields from Figure 6.6 (*i*) B_a = 0.28, (*ii*) 0.30 T and (*iii*) 0.32 T, blue, red and black respectively. Each trace has been offset by 2 dB for clarity. Dashed circles represent the FMR which moves through the SRR resonance as the field is increased.

For the electric-dipole resonance of the SRR at 10.9 GHz the currents travel essentially on the surface of the SRR. The skin depth of the EM field at a given frequency is given by Eq. 6.2 below [28]:

$$\delta = \sqrt{\frac{2\rho}{2\pi v \mu_0 \mu_r}} \qquad (6.2)$$

Here ρ is the bulk resistivity, μ_r is the relative permeability and v the frequency. For copper the skin depth is approximately 1 µm, considerably smaller than the thickness of the SRR. For the electric-dipole resonance the currents oscillate around the ring in a symmetrical fashion about the symmetry axis of the SRR. By contrast for the magnetic resonance at ≈ 5 GHz (black circle in Figure 6.5) the currents precess around the two rings in unison creating an effective magnetic dipole passing through the plane of the SRR. We have confirmed this experimentally by shorting the gaps in the ring with a short strip of conducting wire which eliminates the magnetic but not electric mode [29].

As the field is increased, the YIG resonance passes through the SRR resonance leading to hybridisation as shown in Figure 6.7 (B_a = 0.306 T). There is a 1.6 dB modulation in the transmission. At this field value the YIG resonance is fully hybridised with the natural resonance of the SRR. For higher or lower fields it is possible to identify the FMR separately as shown in Figure 6.7 (see circles). It is also evident on comparing the curves of B_a = 0.2777 T, and 0.3202 T in Figure 6.7 that the SRR trace is inverted in shape and shifted by 0.25 GHz to a lower frequency (B_a = 0.3202) with respect to the first trace of B_a = 0.2777. This is in agreement with the observations of Kang *et al.* and Gollub *et al.* [9, 10]. As well as a change in the absorption of the microwaves across the anti-crossing a change in the phase also occurs, a 19.76 ° phase reversal [30] was also observed. This occurred with a similar behaviour to the ν-B_a map reversal in Figure 6.6, this is shown in Figure 6.8.

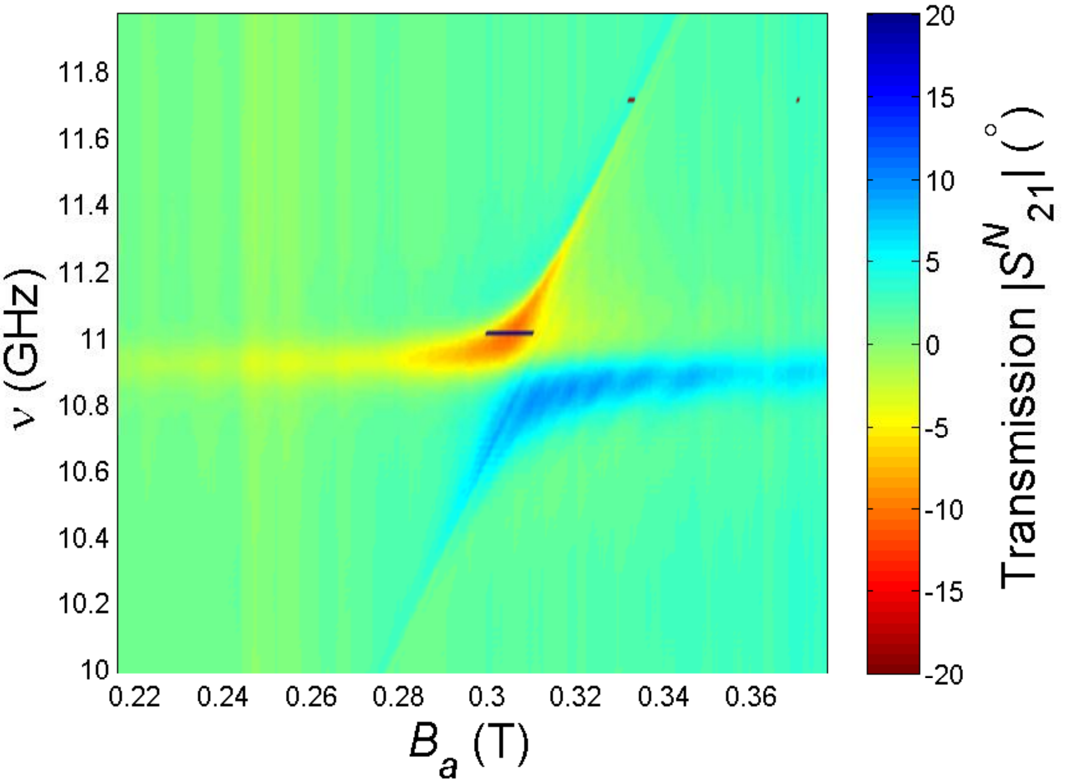

Figure 6.8: ν-B_a map of microwave phase measured in transmission. The black features are due to the use of non-phase stable equipment.

Figure 6.8 displays the microwave phase of the anti-crossing at the electric dipole mode in transmission (S_{21}). The colour at any given point in this plot represents the phase of the microwaves. It shows the phase reversal which occurs across the anti-crossing when taking a fixed applied field and increasing the frequency. The black features present in Figure 6.8 arise from the equipment not being phase stable

Different orientations of the SRR with respect to the direction of the magnetic field were also investigated. The results of these investigations are summarised in Figure 6.9. The black arrows in Figure 6.9 represent the E-field polarisation of the CPW with respect to the geometry of the SRR.

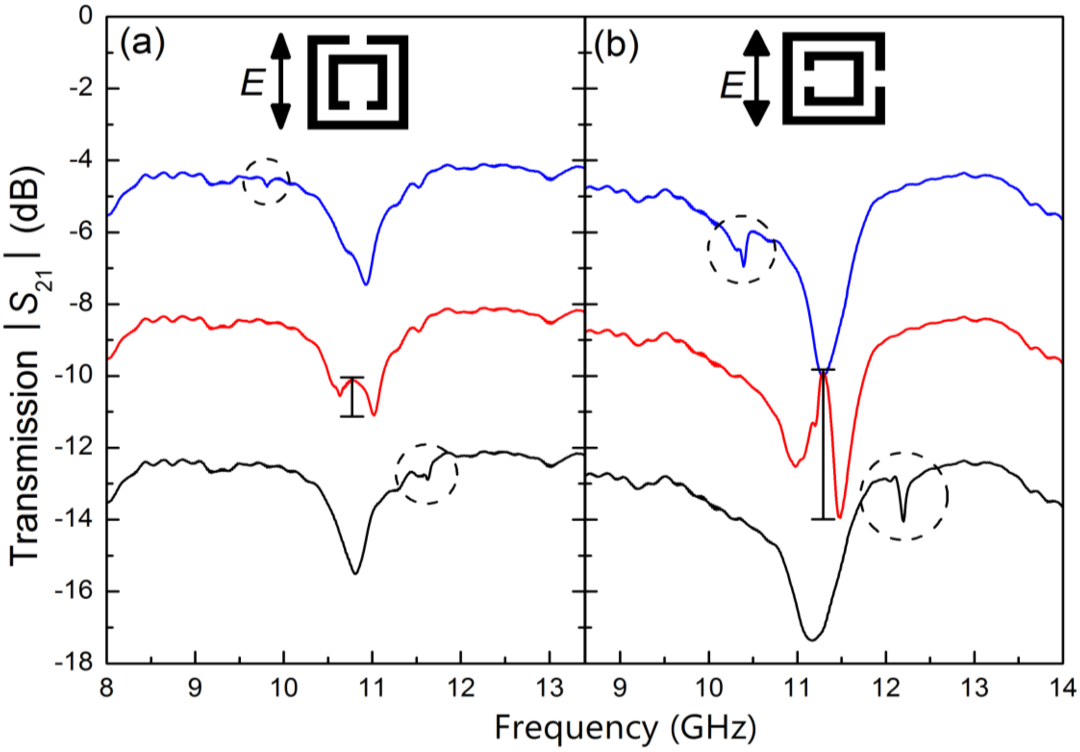

Figure 6.9: Unnormalised data (S_{21}) for two orientations of the SRR. Black arrow represents the electric field polarisation supplied by the CPW. The resonance S_{21} curves blue, red and black were obtained for applied fields of 0.27 T, 0.30 T and 0.33 T respectively. The dashed circles indicate the YIG resonance with vertical black lines representing the modulation in microwave transmission. Each frequency trace has been offset vertically by 4 dB.

An examination of Figure 6.9 indicates that when the gap of the split ring is perpendicular to the propagation of the microwaves, Figure 6.9(b), that the hybridisation of the electric dipole SRR resonance with the YIG is stronger. This is evident by the transmission at the centre of the anti-crossing which has increased by 1.6 to 4 dB. A shift of 0.25 GHz by the SRR electric dipole resonance is also evident as the YIG FMR passes through the electric dipole resonance. Clearly the orientation of the SRR with respect to the magnetic field is important, if desirable increases in microwave transmission S_{21} are to be achieved. Note also the concomitant increases in absorption on both sides of the anticrossing are shown in Figure 6.9. The resonance lineshape shows a similar behaviour to that of the Fano-resonance [31].

Results were also obtained using a linear array of 4 SRRs and multiple YIG films to replicate a metamaterial structure. It was performed as proof of principle that this coupling of a metamolecule to an active magnetic material is scalable to an array. In these experiments, multiple YIG films were used as it was not possible to grow a film large enough that would be uniform across the 4 SRRs. The results are summaried in Figure 6.10 which show that crosstalk and/or differences in the individual electric-dipole resonances do occur. In place of a single SRR resonance there would appear to be at least three electric-dipole resonances in the region of 7-8 GHz.

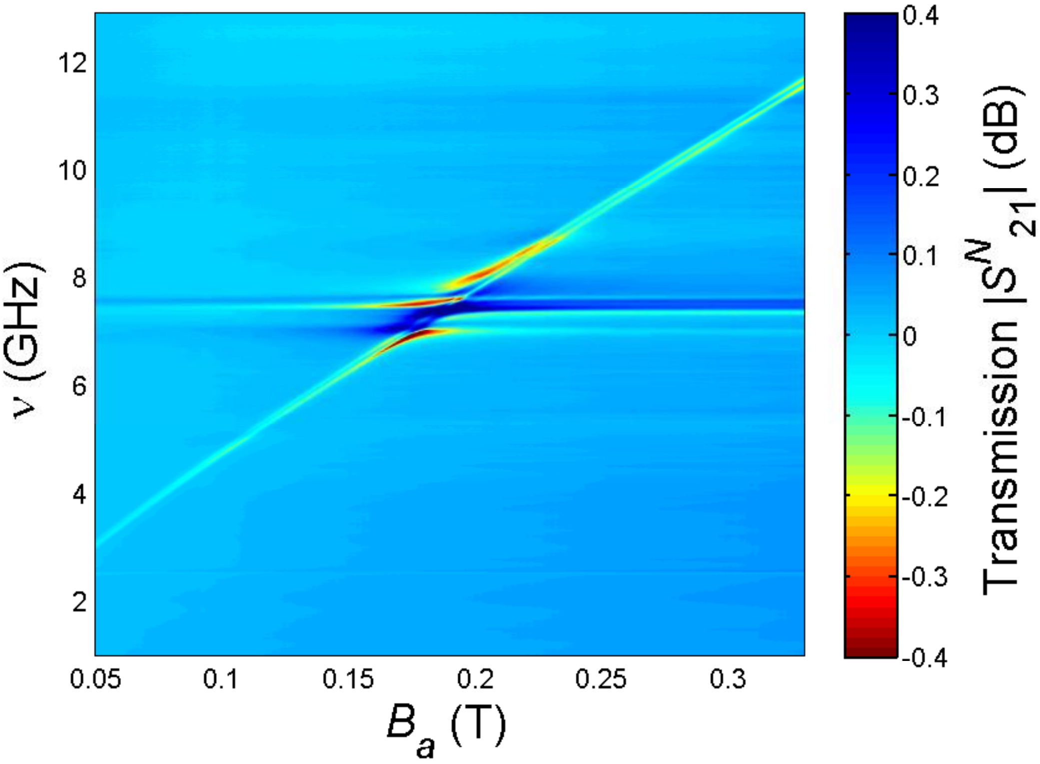

Figure 6.10: (ν-B_a) map of multiple YIG films coupled to four SRRs.

In addition there is a frequency shift down to ~7 GHz arising from the crosstalk/mutual inductance between the 4 SRRs. Nevertheless the results are similar to those obtained for a single metamolecule (cf. Figure 6.6 and Figure 6.10).

6.5 COMSOL modelling

Modelling of the anti-crossing mode using COMSOL has been used to examine the anti-crossing behaviour. In addition a simple two-state model has also been used. Both models replicate the observed anti-crossings. The COMSOL results can be seen in Figure 6.11. The resolution is poor due to the need to cover a wide magnetic field and frequency range necessitating long computing times.

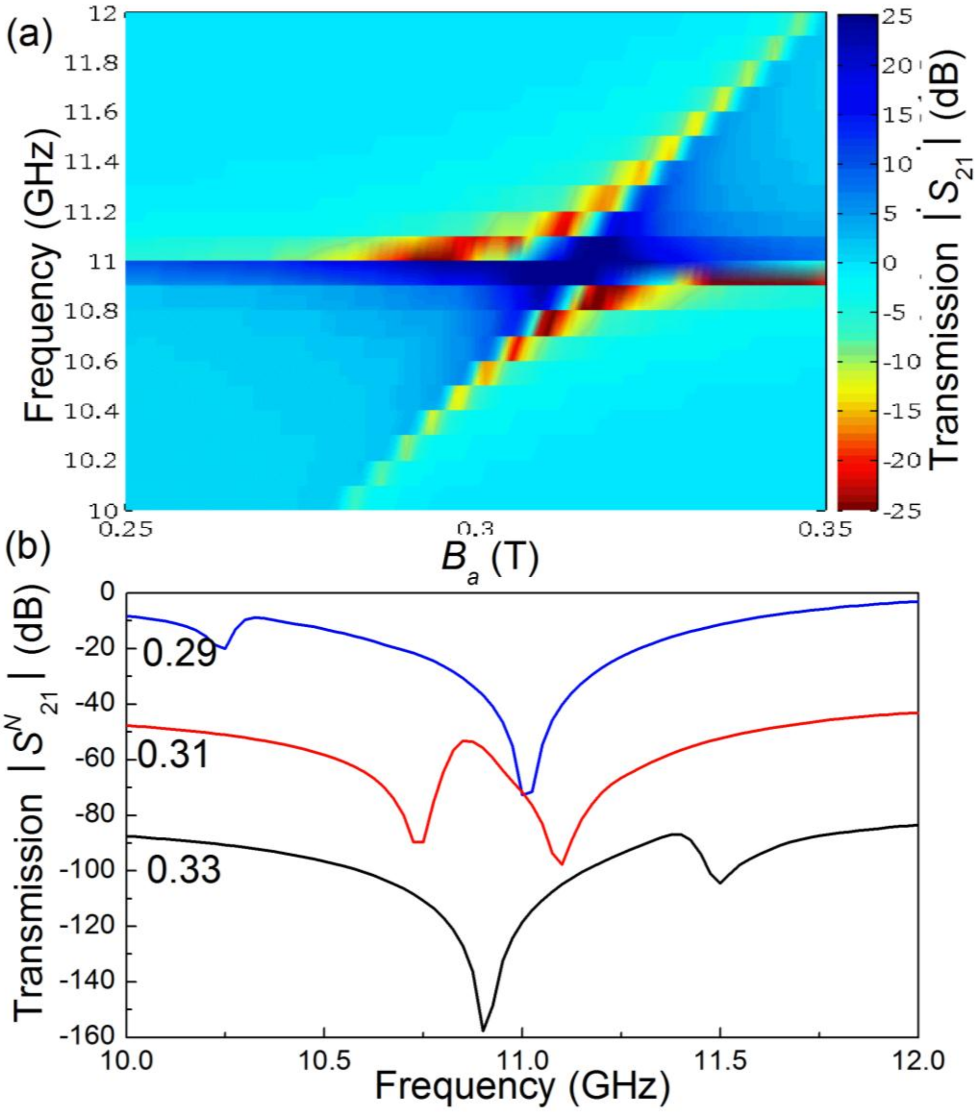

Figure 6.11: COMSOL simulation of a SRR coupled to a YIG film. The microwaves are supplied by a plane wave normal to the SRR and the YIG. (a) ν-B_a map of the anticrossing and (b) line-scans at three different applied fields respectively.

The COMSOL simulations show good agreement with the anti-crossing shape and position. More subtle details such as the observation of BVMSWs are excluded. Further insight into the problem can be gained by adopting the two-state model employed in Ref. [11, 12] for a SRR in close contact with a YIG film. Following the latter, we assert that the anti-crossing between the resonant frequency of the SRR and the YIG resonance can be described by a 2×2 matrix:

$$M = \begin{bmatrix} \nu_{SRR} & \delta \\ \delta & \nu_{YIG} \end{bmatrix} \qquad (6.3)$$

Here, ν_{SRR} (ν_{YIG}) is the resonant frequency of the SRR (YIG film) respectively, while δ represents the mutual interaction between the SRR and the YIG film as a result of the inductance between the two components. The YIG resonant frequency for a thin film magnetised in plane is given by the Kittel equation:

$$\nu_{YIG} = \gamma\sqrt{B_a(B_a + \mu_0 M_0)} \qquad (6.4)$$

Where, γ and M_0 are the gyromagnetic ratio and saturation magnetisation of YIG respectively, so for a finite interaction δ, anti-crossing and mode mixing will occur. This is particularly evident when the diagonal elements of the matrix $\overline{M}$ are degenerate. Mode mixing of the SRR and YIG resonances then amounts to 50%. In general, the roots of $\overline{M}$ are given by:

$$\lambda_{\pm} = \tfrac{1}{2}(\nu_{SRR} + \nu_{YIG}) \pm \tfrac{1}{2}\sqrt{(\nu_{SRR} - \nu_{YIG})^2 + 4\delta^2} \qquad (6.5)$$

At the anti-crossing $\lambda_{\pm} = \nu_{SRR} \pm \delta$. Thus the splitting between the two branches is 2δ, which allows a simple measurement of the strength of the interaction and hence coupling between the YIG and the SRR. From experimental data in Figure 6.6 we find $\delta \approx 0.15$ GHz. This represents the separation of the two branches of the anti-crossing at a fixed applied field in terms of frequency (the bandwidth). On using this value with (*i*) $\nu_{SRR} = 10.9$ GHz, (*ii*) $M_0 = 139.26 \times 10^3$ Am^{-1} [1], and (*iii*) $\gamma = 2.949\times10^{10}$ (HzT^{-1}) [2]. The combined response of the SRR and YIG film (solid lines) is shown in Figure 6.12. Upon comparing experimental results from Figure 6.6, it is evident the two-state model describes the observations well.

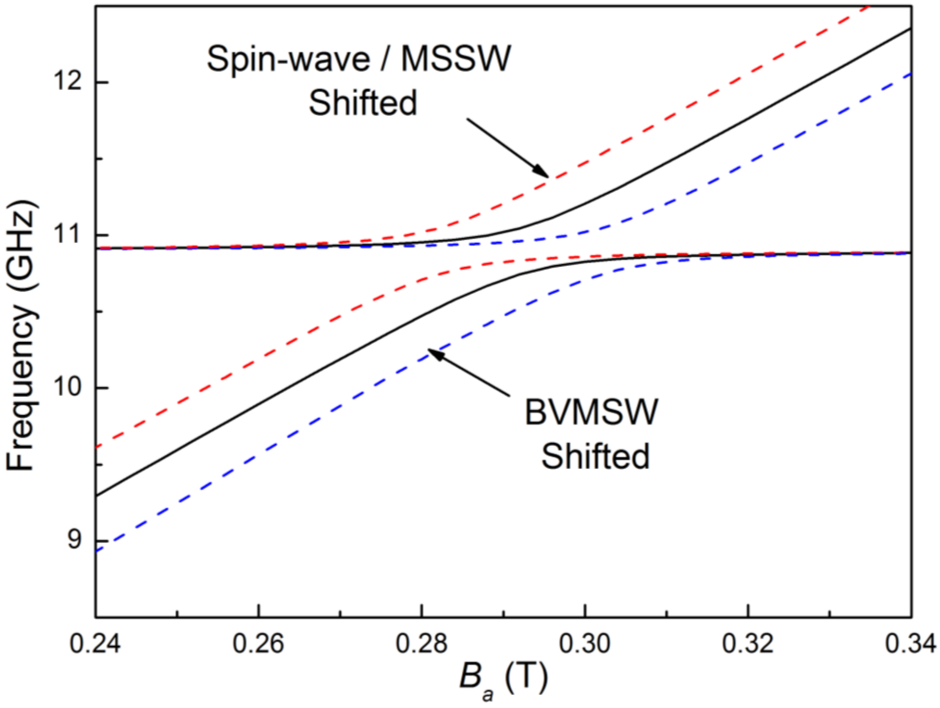

Figure 6.12: Anti-crossing of the YIG and SRR modes. Obtained using a two-level model. MSSW and BVMSW excitations are represented by the red and blue lines respectively.

The two-state model is easily modified to take into account the generation of spin-waves and/or non-uniform Walker magnetostatic modes. For a spin-wave or MSSW the YIG resonance is shifted according to Ref [13]:

$$\nu_{YIG} = \gamma\sqrt{(B_a + Dk_s^2)(B_a + \mu_0 M_0 + Dk_s^2)} \qquad (6.6)$$

Energy of the spin-wave is given by E(k_s) = Dk_s^2, where D is the spin-wave stiffness factor and k_s the wavenumber. By comparison of Eq. (6.4) and (6.6) it is evident that the generation of spin-waves with differing wave-vectors k_s will give rise to hosts of parallel lines left of the uniform Walker mode. By contrast generation of non-uniform volume magnetostatic modes will give rise to lines on the right of the uniform Walker mode, these are known as BVMSWs (see Ref. [13], p157 and 165). Unlike spin-waves and MSSWs, BVMSWs are characterised by a negative group velocity $v_g = \partial\omega/\partial k_s < 0$: hence the description 'backwards moving'. In practice, the generation of spin-waves, MSSWs or non-uniform Walker modes will be dictated by the geometry and strength of the rf field associated with the SRR. For the thin YIG sample in question it is evident that there are a very large number of allowed k-values given the very large aspect ratio (thickness to width) of the thin film ~1:3 × 10^3 (see Ref. [3-4, 27]). To examine this point in more detail therefore experiments were performed using bulk YIG. The results for a 5×5×0.5 mm^3 thick piece (aspect ratio of 1:10) can be seen in Figure 6.13.

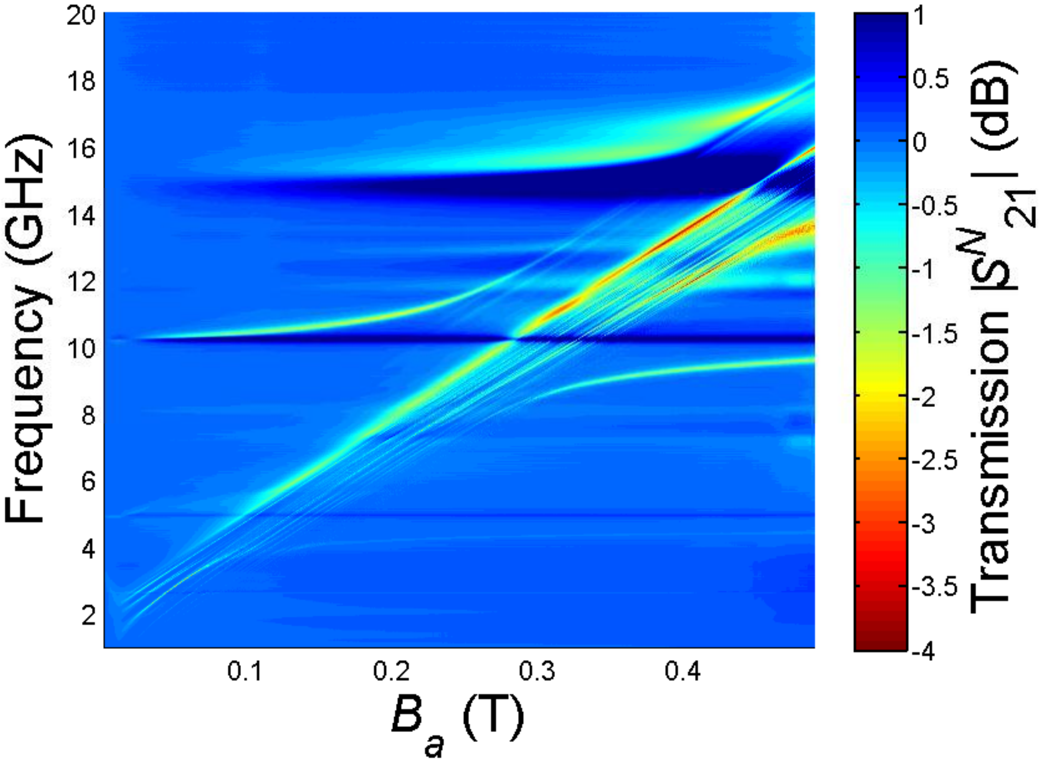

Figure 6.13: S_{21} (ν-B_a) map of bulk YIG crystal 5×5×0.5 mm^3 coupled to a SRR. Notice that the absorptions and anti-crossing features are much stronger given the amount of YIG in the hybrid system.

Two features are immediately apparent, (*i*) the YIG FMR resonance is now dominant over that of the SRR appearing directly in the anti-crossing region and (*ii*) the discrete nature of the BVMSWs is now very apparent on the right-hand side of the FMR. These are the magnetostatic waves first described by Dillon [27]. Some lines are also apparent on the left-hand side of the FMR. We attribute these lines to spin-waves or MSSWs with long wavelengths λ~1 μm. Clearly the non-linear interaction between the SRR and bulk YIG provides a fertile breeding ground for the excitation of spin-waves, surface magnons and BVMSWs. In practice it should be possible to generate specific excitations with well-defined k_s values, using SRRs with tailored shapes, such as those shown in Figure 1 of Ref. [12]. More work is required to determine the optimum thickness, filling factor of the YIG film with respect to the dimensions of the SRR. The precise form of the rf excitation fields produced by the SRR is important. At the so-called magnetic-mode at ~5 GHz anti-crossing exists but at a much weaker level. The interactions described above are much stronger when the SRR is excited in the symmetric-electric mode ~10.9 GHz. This requires further investigation.

6.6 Conclusion

In summary, it has been demonstrated that CPW-based composite SRR metamaterials incorporating a magnetic component (YIG) can be tuned by applying a magnetic field [32]. The coupling between the SRR and the YIG gives rise to hybridisation of the two resonances yielding a frequency response similar to that of a Fano-resonance [31]. In particular the anti-crossing regime allows tuning over a frequency range ~0.3 GHz much wider than that of the SRR metamaterial taken in isolation. There is good agreement between the experiment with electromagnetic simulations obtained using COMSOL and the two-state model [11, 12]. It has also been demonstrated that the anti-crossing region provides a fertile ground for the creation of elementary excitations. Spin-waves, magnetostatic surface waves and backwards volume magneto-static waves have been observed. It has been shown that the orientation of the SRR with respect to the magnetisation of the YIG and CPW is important. In particular, transmission at the centre of the anti-crossing, could be increased by 1.6 to 4.0 dB, simply by rotating the SRR through 90°. These experiments demonstrate that tunability is dependent not only on the strength of the magnetic field but also on the orientation of the SRR with respect to the CPW. Subsequent work with optimised structures has shown that much larger modulation is achievable (70 dB).

References

1. H. How, P. Shi, C. Vittoria, L. C. Kempel, and K. D. Trott, *J. Appl. Phys.* **87,** 4966. (2000).
2. C. Kittel, "*Introduction To Solid State Physics, Eighth Edition,"* (Wiley and Sons, Inc. 2005).
3. L. R. Walker, *J. Appl. Phys.* **29,** 318. (1958).
4. R. W. Damon, and J. R. Eshback, *J. Phys. Chem. Solids.* **19,** 308. (1961).
5. R. A. Shelby, D. R. Smith, and S. Schultz, *Science.* **292,** 77–79. (2001).
6. D. Schurig, J. J. Mock, B. J. Justice, S. A. Cummer, J. B. Pendry, A. F. Starr, and D. R. Smith, *Science.* **314,** 977–980. (2006).
7. J. B. Pendry, A. J. Holden, D. J. Robbins, and W. J. Stewart, *IEEE Trans. Microw. Theory Tech.* **47,** 2075–2084. (1999).
8. M. A. Abdalla and Z. Hu, *IEEE International Symposium on Antennas and Propagation.* (APSURSI) 1054–1057.(2011).
9. L. Kang, Q. Zhao, H. Zhao, and J. Zhou, *Opt. Express.* **16,** 8825–8834. (2008).
10. J. N. Gollub, J. Y. Chin, T. J. Cui, and D. R. Smith, *Opt. Express.* **17,** 2122–2131. (2009).
11. S. Haroche and J. M. Raimond, *Exploring the quantum: Atoms, cavities and Photons.* (Oxford University Press, 2006).
12. H. Huebl, C. Zollitsch, J. Lotze, F. Hocke, M. Greifenstein, A. Marx, R. Gross, and S. T. B. Goennenwein, arXiv:1207.6039v1 [quant-ph] (25 Jul 2012).
13. A. G. Gurevich and G. A. Melkov, "*Magnetization Oscillations and Waves,"* (CRC Press, 1996).
14. F. Martín, F. Falcone, J. Bonache, R. Marqués, and M. Sorolla, *IEEE Microw.Wireless Compon. Lett.* **13,** 511–513. (2003).
15. F. Falcone, F. Martín, J. Bonache, R. Marqués, and M. Sorolla, *Microw. Opt. Technol. Lett.* **40,** 3–6 (2004).
16. C. Saha, J. Y. Siddiqui, and Y. M. M. Antar, *XXXth URSI General Assembly and Scientific Symposium.* 1–4. (2011).
17. R. A. Shelby, D. R. Smith, S. C. Nemat-Nasser, and S. Schultz, *Appl. Phys. Lett.* **78,** 489–491. (2001).
18. D. D. Stancil, A. Prabhakar, "*Spin Waves: Theory and Applications,"* (Springer, 2009)
19. R. W. Eason, "*Pulsed Laser Deposition of Thin Films-Applications-Led Growth of Functional Materials,"* (Wiley Interscience, 2007).
20. C. L. Sones, M. Feinaeugle, A. Sposito, B. Gholipour, and R. W. Eason, *Opt. Express* **20,** 15171–15179. (2012).

21. A. Sposito, T. C. May-Smith, G. B. G. Stenning, P. A. J. de Groot, R. W. Eason, *Opt. Mater. Express.* **3,** 624. (2013).

22. H. Zhao, J. Zhou, L. Kang, and Q. Zhao, *Opt. Express.* **17,** 13373–13380. (2009).

23. J. M. L. Beaujour, A. D. Kent, D. W. Abraham, and J. Z. Sun, *J. Appl. Phys.* **103,** 07B519. (2008).

24. P. He, J. Gao, C. T. Marinis, P. V. Parimi, C. Vittoria, and V. G. Harris, *Appl. Phys. Lett.* **93,** 193505. (2008).

25. D. R. Smith, D. C. Vier, T. Koschny, and C. M. Soukoulis, *Phys. Rev. E Stat. Nonlin. Soft Matter Phys.* **71,** 036617. (2005).

26. S-Parameters...Circuit analysis and design. *HP Application note 95.* (1968).

27. J. F. Dillon Jr., *J. Appl. Phys.* **31,** 1605–1614. (1960).

28. D. J. Griffiths, "*Introduction to Electrodynamics, Third edition,*" (Pearson, 1998).

29. T. Koschny, M. Kafesaki, E. N. Economou, and C. M. Soukoulis, *Phys. Rev. Lett.* **93,** 107402. (2004).

30. M. Lu, J. Y. Chin, R. Liu, and T. J. Cui, *IEEE International Conference on Microwave and Millimeter Wave Technology.* 978–980. (2008).

31. B. Luk'yanchuk, N. I. Zheludev, S. A. Maier, N. J. Halas, P. Nordlander, H. Giessen, and C. T. Chong, *Nat. Mater.* **9,** 707–715. (2010).

32. G. B. G. Stenning, G. J. Bowden, L. C. Maple, S. A. Gregory, A. Sposito, R. W. Eason, N. I. Zheludev, and P. A. J. de Groot, *Opt. Express.* **21,** 1456. (2013).

7. Summary and outlook

Investigation and research in this thesis has focused on model magnetic data storage media and microwave devices. In particular, hard and soft magnetic 'exchange spring' systems [1] provide a high stability against magnetic reversal due to thermal effects, but in parallel provide a reduced coercivity [2]. The latter allows data to be written to the media with ease thereby alleviating the superparamagnetic problem.

The magnetisation dynamics of strongly exchange-coupled multilayer systems with different magnetic hardness were also investigated as a system with increased resonant frequencies, ultimately leading to increased read and write speeds in hard disk drives (HDD), and other microwave devices. Microwave devices are the last topic of study in this thesis, where a new branch of physics named 'metamaterials' [3-5] is covered and new magnetic field dependent devices are presented.

This research provides new insights and understanding into exchange spring media and the discovery of new spring states while developing the XMCD technique at high fields for hard-soft composite multilayers. The research also progressed to cover magnetisation dynamics in exchange-coupled multilayers and microwave devices by establishing an FMR spectroscopy rig and developing XFMR techniques at the Diamond Light Source. The systems investigated were expitaxially grown films which due to well-defined anisotropies and sharp interfaces, between the layers in the exchange spring multilayers, are ideally suited for investigating the fundamental behaviour.

In investigating these effects we used in-house experimental techniques and also made use of synchrotron facilities to further probe the model systems using x-rays. The following section summarises the results and addresses the questions which were set out at the beginning of this thesis

There were three main questions which we aimed to address by the completion of this thesis:

(*i*) What are the various exchange spring states associated with the rare earth multilayers and what are their switching and reversal mechanisms?
(*ii*) How has the magnetisation dynamics changed for an exchange-coupled bilayer system?
(*iii*) Can metamaterials be coupled to magnetic material to obtain tunability?

7.1 Result summary

Exchange springs

Ferromagnetic exchange springs have been proposed as a solution to limitations imposed by thermal effects and writeability of magnetic HDD. Such multilayers circumvent the so-called superparamagnetic limit, due to high thermal stability and low coercivity. This is achieved by hard and soft magnetic layers exchange-coupled together. This produces a non-coherent reversal of the magnetic moments. The thicker soft layer enables the non-coherent reversal by setting up an exchange spring thereby reducing the switching field. To better understand the reversal and switching mechanisms, antiferromagnetic exchange spring systems were studied in this thesis. These systems consisted of alternating hard and soft exchange-coupled magnetic multilayers, such as $ErFe_2/YFe_2$ [6], $DyFe_2/YFe_2$ [7] and NiFe/CoFe.

The superlattices were grown by molecular beam epitaxy (MBE) by our collaborators at Oxford University and, because of the well-defined anisotropy and interlayer exchange and as such are useful model systems. New magnetic exchange spring states were revealed using a number of experimental techniques *e.g.* magnetometry, micromagnetic modelling and most valuable of all, x-ray magnetic circular dichroism (XMCD) [8] performed on the new high-field magnet system (14 T) at the Diamond Light Source. Our experiments were the first to employ this beamline and formed a testbed of its capabilities. XMCD allows the individual layers of the multilayer sample to be probed individually, thereby revealing the underlying mechanisms governing the switching of the exchange spring. During these experiments hysteresis loops at the Er, Dy and Fe edges were collected.

It was found that for the $ErFe_2/YFe_2$ system using bulk magnetometry that any switching of the Er moments is masked by changes in the magnetic exchange spring [9]. In XMCD hysteresis loops at the Er edge indicate these effects were much more pronounced and revealed a crossover from a single switch ($T< 200$ K) (transverse exchange spring) to a double switch ($T> 200$ K). The double, switching labelled as a ‘spin-flop’ transition [6] is due to the Er^{3+} anisotropy which allows the Er magnetic moments to change direction from an out-of-plane direction $\langle 111 \rangle$ to an in-plane $\langle 111 \rangle$, by slipping over a small saddle point in the Er anisotropy surface.

The second exchange spring system investigated was $DyFe_2/YFe_2$ where in contrast, the easy and hard axes of magnetisation lie, in the plane, along a [001] and $[\bar{1}10]$-axis respectively. Experiments on this system showed that the reversal mechanism is the result of a switch from an [001] reversed antiferromagnetic state to an in-plane $[00\bar{1}]$ magnetic exchange spring takes place via an [100] out-of-plane transverse exchange spring state. It occurs by passing through two irreversible transitions. The intermediate state shows up in the bulk magnetometry [10] again as a weak irreversible transition at high field. The new intermediate state is given the name of a ‘transverse exchange spring’ [11]. The exchange springs are due to the cubic magnetic anisotropy of the Dy^{3+} ions.

Magnetisation dynamics

The second theme of research described in this thesis focused on the magnetisation dynamics of a transition metal bilayer, again grown by MBE. The dynamics of this system has potential relevance for the speed of read/write characteristics of complex multilayer data storage media. A ferromagnetic resonance (FMR) spectroscopy rig was built and developed at Southampton University to investigate the resonant frequencies of multilayer samples. The prime intention was to observe how a strong anisotropic material such as CoFe magnetically influences a soft NiFe layer with weak anisotropy when the two layers are strongly coupled by exchange interactions. Our preliminary FMR results showed two main resonant modes, a high and low frequency mode. To unravel these modes further x-ray detected FMR (XFMR) [12, 13] was used incorporating the XMCD technique. We developed this technique at the Diamond Light Source with members of the magnetic spectroscopy group. It allows the amplitude and relative precessional phase of the two resonant modes to be examined with respect to the Co and Ni elements and hence of the individual layers. It was also shown that a weak third resonant mode present in VNA-FMR was in fact due to the Fe in the seed layer. This demonstrates the power of XFMR, as only this technique could have been used to unravel this problem. Investigations showed that for the lowest frequency mode all the spins from both the Ni and the Co precess in phase (≈0°) with the amplitude at a maximum in the NiFe layer, but with the precessional amplitude decaying as the mode penetrates into the CoFe layer. It can be described as a low frequency ‘acoustic-natured mode’. By contrast the high frequency mode was found to possess an almost 180° phase difference between the spins in the two layers of Ni and Co now with the amplitude having a maximum in the CoFe layer. We have labelled this as an ‘optic-natured mode’ [14]. Calculations using the Kittel equation [15] for FMR and simulations using the Nmag simulation package [16] reveal that the NiFe and CoFe layers act, to first approximation almost independently of one another but with a ‘transferred’ anisotropy from the CoFe across the interface into the NiFe. This transfer is mediated by the strong exchange coupling across the bilayer interface and induces a residual four-fold anisotropy in the NiFe layer.

Metamaterials (microwave devices)

The final investigation was that of metamaterials [3-5]. The work performed in this thesis has opened up new metamaterial research directions. In particular, we investigated whether these new microwave devices can be controlled by an applied magnetic field to achieve tunability of the metamaterial resonant frequency and absorption depth. The topic of metamaterials is a recently developed branch of physics. Metamaterials consist of patterned material structures, for instance the archetypical split ring resonators (SRR) [5], to induce unusual electromagnetic properties not attainable in optical or microwave materials found in nature. In our investigations reported here a metamolecule (single element of a metamaterial) was fabricated onto a coplanar waveguide (CPW) and then coupled to a soft magnetic thin film which was tuned to FMR by an applied magnetic field. A magnetic film of yttrium iron garnet (YIG) [17] was coupled to an SRR metamolecule structure and through the application of a magnetic field the SRR resonance frequency was changed. These novel metamaterial hybrid structures investigated showed that magnetic tunability of the metamolecule can be obtained. The hybridised resonance has a line shape similar to that of the Fano-resonance [18]. At the point of hybridisation a tuning of 0.3 GHz of the metamaterial is observed; a much greater response than when the SRR is taken in isolation and not coupled to the magnetic material. It is at this hybridisation (anti-crossing) that modulation of the metamolecule is achieved (1.6 dB). Consequently it was shown that this can be optimised by changing the geometry of the SRR with respect to the CPW (now 4 dB) and hence the excitation fields at various points of the SRR. Agreement was found between these experiments and electromagnetic simulations using COMSOL, as well as a simple two state model. At the hybridised resonance the creation of spin-waves was also observed which have the characteristics of magnetostatic surface waves and backwards volume magnetostatic waves [19]. Our research on magnetically tunable metamaterials has inspired further research on coupling NiFe patterned films to a metamolecule. This work was performed by Simon Gregory using the equipment developed in this project. The system was found to have a 40 dB modulation depth at resonance.

7.2 Future work

The opportunity and capacity for further investigation on the various systems described go beyond the initial results covered in this thesis.

Principally the *exchange spring multilayers* still offer further areas for research as only in recent years XMCD has been introduced as a technique to unravel the reversal and switching processes governing the behaviour of these multilayers. A magnetic system consisting of a $DyFe_2$/YFe_2 multilayer with a monatomic layer of $ErFe_2$ placed in the thick softer YFe_2 is planned. This system will have competing effects from the out-of-plane easy axis from the Er anisotropy and the in-plane easy axis from the Dy. XMCD will offer a unique opportunity to study these effects of these competing anisotropies by probing both the Dy and Er edges. The influence of introducing a weak anisotropic monatomic layer in the thick YFe_2 layer will also affect the exchange spring and how it is set up.

Also the second theme of this thesis has a huge potential for further work. *Investigating the magnetisation dynamics of bilayers*. In this thesis XFMR studies of a bilayer of NiFe/CoFe were presented and the dynamics of this bilayer were analysed. The CoFe has a four-fold anisotropy associated with it, which can be used to change the resonant frequency of the system by applying fields along the easy and hard axis of magnetisation respectively. Therefore further work is required to expand our understanding of the dynamics in these systems. Specifically by (*i*) changing the composition of the CoFe thereby changing the anisotropy strength, (*ii*) changing the direction of the applied field during the XFMR measurements favouring the easy or hard axis of magnetisation and (*iii*) changing the thickness of the constituent layers.

The final area of research is the new topic of *magnetic metamaterials*. Here there is a broad and diverse field which can be investigated. The results presented in this thesis show that an insulating magnetic film of YIG can be coupled to a metamaterial to create a hybridised resonance. It can be extended to couple transition metal magnetic films to metamaterials therefore opening up the opportunity for further microwave devices. As magnetic materials can be prepared in different metastable states this opens the way to ‘configurable metamaterials’ a device functionality much sought after in the metamaterials community.

Further experiments are planned at the Diamond Light Source for August 2013 to develop a new technique, using XFMR on a magnetic material initially NiFe coupled to an SRR. The aim of these experiments is to map the excitation amplitude and phase across the magnetic film with respect to points of the SRR where the SRR rf fields are expected to be a maximum.

References

1. R. Wood, *J. Magn. Magn. Mater.* **321,** 555. (2009).
2. A. R. Buckingham, *Ph. D. Thesis*, University of Southampton, UK (2010).
3. R. A. Shelby, D. R. Smith, and S. Schultz, *Science.* **292,** 77–79. (2001).
4. D. Schurig, J. J. Mock, B. J. Justice, S. A. Cummer, J. B. Pendry, A. F. Starr, and D. R. Smith, *Science.* **314,** 977–980. (2006).
5. J. B. Pendry, A. J. Holden, D. J. Robbins, and W. J. Stewart, *IEEE Trans. Microw. Theory Tech.* **47,** 2075–2084. (1999).
6. G. B. G. Stenning, A. R. Buckingham, G. J. Bowden, R. C. C. Ward, G. van der Laan, L. R. Shelford, F. Maccherozzi, S. S. Dhesi, and P. A. J. de Groot, *Phys Rev. B.* **84,** 104428. (2011).
7. G. B. G. Stenning, G. J. Bowden, S. A. Gregory, J. –M. L. Beaujour, A. N. Dobrynin, L. R. Shelford, P. Bencok, P. Steadman, T. Hesjedal, G. van der Laan, P. A. J. de Groot, *Appl. Phys. Lett.* **101,** 072412. (2012).
8. G. van der Laan, and B. T. Thole, *Phys. Rev. B.* **43,** 13401. (1991).
9. K. N. Martin, K. Wang, G. J. Bowden, A. A. Zhukov, J. P. Zimmermann, H. Fangohr, R. C. C. Ward, and P. A. J. de Groot, *Appl. Phys. Lett.* **89,** 132511. (2006).
10. J. –M. L. Beaujour, *Ph. D. Thesis*, University of Southampton, UK (2003).
11. G. B. G. Stenning, G. J. Bowden, S. A. Gregory, A. N. Dobrynin, L. R. Shelford, P. Bencok, P. Steadman, T. Hesjedal, G. van der Laan, P. A. J. de Groot, *Phys. Rev. B.* **86,** 174420. (2012).
12. M. K. Marcham, P. S. Keatley, A. Neudert, R. J. Hicken, S. A. Cavill, L. R. Shelford, G. van der Laan, N. D. Telling, J. R. Childress, J. A. Katine, P. Shafer, and E. Arenholz, *J. Appl Phys.* **109,** 07D353. (2011).
13. D. A. Arena, E. Vescovo, C. -C. Kao, Y. Guan, and W. E. Bailey, *Phys. Rev. B.* **74,** 064409. (2006).
14. G. B. G. Stenning, L. R. Shelford, S. A. Gregory, F. Hoffmann, M. Haertinger, T. Hesjedal, R. C. C. Ward, G. Woltersdorf, S. A. Cavill, G. J. Bowden, G. Ashton, L. C. Maple, C. H. Back, H. Fangohr, G. van der Laan, and P. A. J. de Groot, In preparation. (2013).
15. C. Kittel, *Phys. Rev.* **73,** 155161. (1948).
16. http://nmag.soton.ac.uk/
17. A. Sposito, T. C. May-Smith, G. B. G. Stenning, P. A. J. de Groot, R. W. Eason, *Opt. Mater. Express.* **3,** 624. (2013).
18. B. Luk'yanchuk, N. I. Zheludev, S. A. Maier, N. J. Halas, P. Nordlander, H. Giessen, and C. T. Chong, *Nat. Mater.* **9,** 707–715. (2010).

19. G. B. G. Stenning, G. J. Bowden, L. C. Maple, S. A. Gregory, A. Sposito, R. W. Eason, N. I. Zheludev, and P. A. J. de Groot, *Opt. Express.* **21,** 1456. (2013).

Appendix A

Diamond beamtime proposal written and submitted by Dr Stuart Cavill on our behalf.

X-ray detected FMR of magnetically tunable metamaterials

Introduction

Metamaterials are patterned structures with electromagnetic properties that are unattainable in nature. Being initially intended to achieve negative refraction, allowing effects such as ‘super lensing’ and ‘cloaking’ [1]. The concept of metamaterials has quickly covered a much broader range of applications including those in microwaves, optics and acoustics. To a large extent, this emerging field has been stimulated by the theoretical work of John Pendry's group [2], which made two distinct predictions: (*i*) anomalous magnetic permeability at optical frequencies—which is a prerequisite for negative-index metamaterials and (*ii*) enhanced and novel nonlinear-optical properties. Motivated by the promise for ground-breaking science and new effects not seen in natural systems, a rich research field has developed in recent years. This research has almost-exclusively concentrated on relatively simple materials based on ohmic metals and low-loss dielectrics and to date metamaterials are used only as passive devices; the full potential of active metamaterials has yet to be exploited. Split-ring resonators (SRRs) have become the key building blocks for composite metamaterials, particularly in materials having negative refractive index [3]. Recent theoretical studies have demonstrated how to tune dynamically the electromagnetic properties of metamaterials [4] and the fabrication of nonlinear SRRs has been demonstrated by placing a varactor diode [5] within the gap of the resonator. The diode allows the metamaterial to be tuned by an applied dc voltage or by a high-power signal [6]. These advances allow for systematic studies of nonlinear tuneable metamaterials which may change their properties and transmission characteristics by varying the amplitude of the input electromagnetic field.

Recently we have demonstrated a further route to tunability by coupling a SRR based metamaterial to soft magnetic films [7]. The tunability of the magnetic resonances in the microwave, mm-wave regime, offers a powerful means to realize controllable and loss-compensating devices. Broadband FMR experiments using vector network analyser ferromagnetic resonance (VNA-FMR) reveal a number of distinct anti-crossing features which can be ascribed to a coupled oscillator of the magnetic thin film with the “meta-atom” (split-ring resonator), hence showing the tunable potential of this composite metamaterial (Figure 1). The hybridisation can be clearly observed as an increase in the microwave transmission where the horizontal line (resonance of the meta-atom) intersects with the diagonal absorption line of the magnetic film.

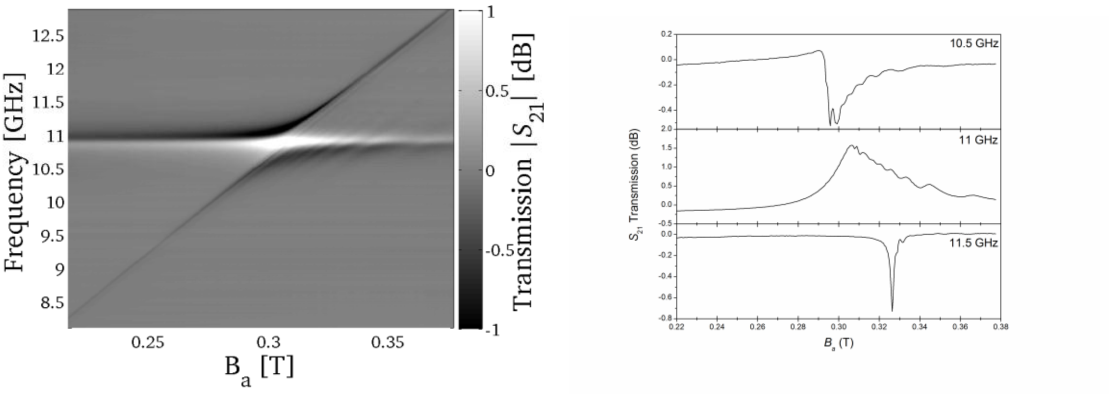

Figure 1: (a) VNA-FMR, frequency versus magnetic field map of the hybrid magnetic metamaterial. (b) Cuts from Figure 1a showing the normalised transmission *versus* applied field at three fixed frequencies.

Aim

We now wish to develop our understanding of these magnetically tuneable metamaterials by using phase resolved x-ray detected ferromagnetic resonance (XFMR) to spatially map the coupling of the resonance across the metamaterial structure. Using XFMR we intend to produce a two-dimensional (2D) map of the magnitude and phase of the magnetic precession across the hybrid magnetic metamaterial at both the magnetic and electric resonances allowing information to be gained on the dynamics in the near field (close to the gap of the resonator); the RF wavelength at the frequencies of interest is of the order of a 10's mm.

In particular, our recent FMR study of the hybrid magnetic metamaterial reveal that the anti-crossing resonance is an electric mode due to oscillating currents in the split-ring resonator (SRR). This arises from the polarisation of the microwave excitation. Other magnetic and electric mode resonances have been observed with similar properties in the anti-crossing regime shown above. The natural resonance of the SRR can be altered by varying the ring size and orientation relative to the excitation field thereby allowing the anti-crossing to be modified.

Experimental Method

The magnetic material yttrium iron garnet (YIG), is grown by pulsed-laser deposition with the gold SRR etched directly onto the magnetic film yielding the greatest coupling between the SRR and the magnetic film. YIG, a ferrimagnetic insulator gives a large magnetic moment suitable for hybridisation and has extremely low damping allowing for large signals in XFMR. The sample will be placed "flip-chip" onto a coplanar waveguide (CPW) to excite the structure (Figure 2) with microwave frequencies between 0.5-12 GHz. As the RF signal applied to the CPW is phase locked to the master RF signal of the synchrotron and therefore the x-rays, we will stroboscopically probe the projection of the magnetic moments as they precess about static bias field. This transverse XFMR scheme (bias field applied perpendicular the beam direction) allows for phase-resolved measurements as we have previously demonstrated [8] whilst longitudinal XFMR (bias field applied along the beam direction) will allow access to higher frequencies and a greater range of resonant modes. The measurements will be performed in the portable octopole magnetic system (POMS) – a vector magnet that provides fields up to 0.9 T to be applied in an arbitrary direction. The necessary equipment for XFMR is available from the Magnetic Spectroscopy Lab at Diamond and has been used before on beamline I06-1.

The x-ray absorption in the magnetic film will be determined by detecting the fluorescence yield from the YIG [8]. We plan XFMR and XMCD experiments at the $L_{2,3}$ absorption edges for Fe. The experiments will be performed at room temperature and require applied fields up to 0.5 T in different directions with respects of the metamaterial symmetry axis which is possible in POMS. Spatially mapping the XFMR response will be performed by rastering the sample in the x-y plane and recording the XFMR as a function of delay between the RF excitation and the x-rays. Such 'phase' scans at each point will allow both the magnitude and phase of the magnetic response to be mapped. For the two magnetic metamaterial samples of either magnetic or electric resonant modes we request 6 days (18 shifts) on beamline I06-1.

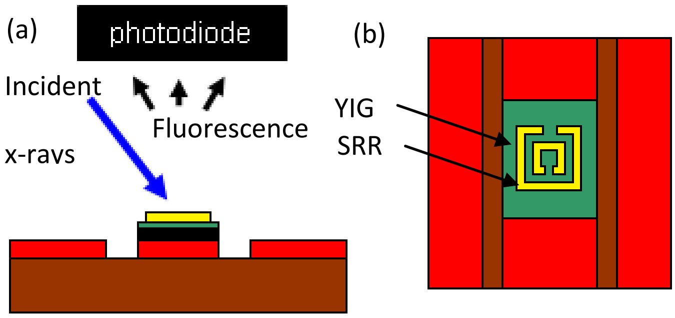

Figure 2: Experimental setup. (a) Side view and (b) top view of coplanar waveguide (CPW) loaded with YIG on YAG film, patterned with gold split ring resonator (SRR) on top (dimension 3.93 mm).

Expected Results and Justification

Common techniques to study magnetisation dynamics are time-resolved magneto-optical Kerr effect (TR-MOKE), Brillouin light scattering (BLS), and microwave ferromagnetic resonance (FMR). FMR measures the spatially averaged response of metallic magnetic films and is therefore not suitable for measuring local effects across the SRR. Spatially resolved BLS and MOKE experiments are problematic due to the SSR coupled to the YIG film which gives rise to scattering and reflection effects. The recently developed technique of XFMR [8] circumvents all these issues and uniquely enables us to measure the phase of the magnetic oscillation at different positions and applied field. This will provide direct insights into the magnetisation damping. In addition, I06-1 is ideally suited to this study as the beam size (200 x 20 micron) is small compared to the wavelength of the RF excitation and dimensions of the SRR. The results will be compared to micromagnetic modelling.

By combining XFMR data with results of our spatially averaged DC magnetometry and FMR measurements we plan to build up a full description of the tunability of magnetic metamaterials and the magnetisation dynamics of the coupled magnetic film across the metamaterial. The results will be an important step forward to understand the magnetic control of metamaterials.

[1] V. Veselago *et al.* J. Comput. Theor. Nanosci. **3**, 1 (2006); D. Schurig *et al*. Science **314**, 977 (2006)

[2] J. B. Pendry *et al*. IEEE Trans. Microw. Theory Tech. **47**, 2075 (1999)

[3] D. R. Smith *et al*. Phys. Rev. Lett. **84**, 4184 (2000)

[4] M. Gorkunov and M. Lapine. Phys. Rev. B **70**, 235109 (2004)

[5] I. V. Shadriov *et al*. Opt. Express **14**, 9344 (2006)

[6] D. A. Powell *et al*. Appl. Phys. Lett. **91**, 144107 (2007)

[7] G. B. G. Stenning *et al*. submitted to Opt. Express **21**, 1456 (2013)

[8] M. K. Marcham *et al*. J. Appl. Phys. **109**, 07D353 (2011)